POLITECNICO DI TORINO

Master's Degree in Aerospace Engineering

Low-Thrust Earth-Moon Transfer Trajectories to Stable Distant Retrograde Orbits using Indirect Optimization Method

Supervisor:
Prof. Manuela Battipede

Author:
Daniele Pice

Co-Supervisor:
Dr. Luigi Mascolo

Academic Year 2023/24

To my beloved grandfather Pino, for always believing in me.

Abstract

This research focuses on identifying low-thrust optimal trajectories for inserting satellites into a Distant Retrograde Orbit (DRO) around the Moon with minimum propellant usage, contributing to cost-effective strategies and enabling heavier payloads for future cislunar missions. This study is motivated by the growing interest in establishing a scientific presence in cislunar space, with initiatives aiming to position orbital stations on such orbits, or to utilize lunar resources and create a launchpad for missions to Mars and beyond. NASA's Artemis program is heading in this direction. Among potential locations, Periodic Orbits around Lagrangian Points, including DROs and Near-Rectilinear Halo Orbits (NRHOs), present promising options. DROs, in particular, offer significant advantages due to their stability, reducing maintenance costs and prolonging mission lifespans.

To optimize DRO insertion trajectories, a Two-Point Boundary Value Problem approach is employed. This method enhances solution convergence amid the chaotic gravitational dynamics between Earth and the Moon and includes an iterative shooting procedure with a bang-bang thrust control law derived from indirect optimal control theory. Pontryagin's Maximum Principle is applied to ensure the optimality of control solutions.

DRO computations are performed within the Circular Restricted Three-Body Problem (CR3BP) framework using a single-shooting method based on the State Transition Matrix analysis. This model accounts for the gravitational influences of the Moon, which significantly impacts both the injection trajectory and the stability of the DRO.

Results indicate that two-burn finite-thrust trajectories present the most efficient means for direct DRO insertion from Earth, effectively exploiting the Earth-Moon gravitational interaction without the need of performing a lunar gravity assist or

multiple swing-bys. The optimal trajectory is proven to be the one that best fits the shape of the orbit, inserting the satellite directly into the final stable DRO.

Contents

List of Figures

List of Tables

Acronyms

2BP	Two-Body Problem
3BP	Three-Body Problem
4BP	Four-Body Problem
ARM	Asteroid Redirect Mission
BC	Boundary Condition
BVP	Boundary Value Problem
CoV	Calculus of Variations
CR3BP	Circular Restricted Three-Body Problem
DM	Direct Method
DRI	Distant Retrograde Orbit Insertion
DRO	Distant Retrograde Orbit
DSG	Deep Space Gateway
EM	Earth-Moon
EME2000	Earth Mean Equator and Equinox of Epoch J2000
EoM	Equation of Motion
EP	Electrical Propulsion
ICRF	International Celestial Reference Frame

IM	Indirect Method
JPL	Jet Propulsion Laboratory
L1	Lagrangian Point L1
L2	Lagrangian Point L2
L3	Lagrangian Point L3
L4	Lagrangian Point L4
L5	Lagrangian Point L5
LEO	Low Earth Orbit
LHS	Left-Hand Side
LO	Lyapunov Orbit
LOP-G	Lunar Orbital Platform-Gateway
LP	Lagrangian Point
MEO	Medium Earth Orbit
MPBVP	Multi-Point Boundary Value Problem
NAIF	Navigation and Ancillary Information Facility
NBP	n-Body Problem
NL	Non Linear
NLP	Non Linear Programming Problem
NRHO	Near Rectilinear Halo Orbit
NSL	Newton's Second Law
OCP	Optimal Control Problem
OCT	Optimal Control Theory
PMP	Pontryagin's Maximum Principle

PO	Periodic Orbit
QPO	Quasi-Periodic Orbit
RF	Reference Frame
RHS	Right-Hand Side
RS	Reference System
SC	Spacecraft
SF	Switching Function
SLS	Space Launch System
STM	State Transition Matrix
TLI	Trans-Lunar Injection
TPBVP	Two-Point Boundary Value Problem
wrt	with respect to
ZEN	Zenith East North
ZVS	Zero-Velocity Surface

Chapter 1

Introduction

1.1 Preface

Since ancient times, humanity has gazed upon the Moon with fervent fascination, intrigued by its mysteries and unexplored possibilities. As early as the III millennium BC in Mesopotamia, the Moon was venerated, personified as the Sumerian god Sin, also known as Nanna. The Pantheon of ancient Greeks included the lunar goddesses Selene, sister to Helios (the Sun) and Eos (the Aurora), and Artemis, the goddess of crescent moon, while the Romans worshipped the corresponding Luna and Diana. Beyond its religious significance, lunar observations profoundly influenced astrology, esotericism, and obviously astronomy. The Roman calendar itself was based on lunar months, at least until the advent of Julian calendar in 46 BC. The Moon has perpetually inspired countless myths and legends. During the Middle Ages, popular belief held that men transformed into fierce wolves under the light of the full Moon, giving rise to the iconic imagery of werewolves. This mystical allure with the Moon extended into art and literature in subsequent centuries. In Dante's masterpiece, *La Divina Commedia* (early 14th century), he describes the ascent through the Moon's spheres towards Paradise. In Ludovico Ariosto's chivalric epic *Orlando Furioso* (1516), the knight Astolfo rides a hippogriff to the Moon to regain the lost sanity of the protagonist Orlando. The fascination for lunar voyages also permeated modern science-fiction literature, from Jules Verne's *From the Earth to the Moon* (1865) to H.G. Wells' *The First Men in the Moon* (1901), and Edgar Rice Burroughs' *The Moon Maid* (1926). In the fantasy genre, J.R.R. Tolkien's cosmology of his fictional

universe Arda includes the lunar goddess Isil (or Ithil), a counterpart to our real Moon. The theme of lunar voyages quickly captured the attention of the newborn cinema, from George Méliès' *A Trip to the Moon* (1902), depicting a spaceship of bullet-like shape fired to the Moon by a cannon, to Fritz Lang's *Woman in the Moon* (1929) and Irvin Pichel's *Destination Moon* (1950), written by Robert A. Heinlein. During the second half of the 20th century, NASA's Mercury (1958-1963), Gemini (1964-1966), and Apollo (1969-1972) space programs marked the beginning of a unprecedented era in space exploration. These missions, which culminated with humanity's first steps on the Moon, captivated global imagination and continued to inspire people. Even before the Apollo 11 mission, Robert Altman and William Conrad's *Countdown* (1967) narrated the story of the first Moon landing rushed by NASA to preempt Sovietic Union. The following year, was released the science-fiction masterpiece par excellence *2001: A Space Odyssey* by Stanley Kubrick. Inspired by Arthur C. Clarke's story *The Sentinel* (1951), it features the discovery of a giant extraterrestrial monolith in Tycho crater, which prompts the protagonists to embark on a deep space mission. More recently, even in the iconic *Star Trek* saga (1998), the Moon is envisioned as a large space station of millions of inhabitans, while in Duncan Jones' film *Moon* (2009), it becomes a massive mining base for isotope extraction. Also noteworthy are Ron Howard's *Apollo 13* (1995), about the miraculous rescue of the crew following the mission own failure, and Damien Chazelle's *First Man* (2018), depicting Neil Armstrong's preparations for the historic Moon landing.

Fig. 1.1 An iconic frame from the first science-fiction film set in space, *A trip to the Moon* by George Méliès (*Le voyage dans la Lune*, 1902).

Today, after centuries of dreaming and sixty years of actual exploration, all the major space agencies and private companies in the world are once again planning to send humans to the Moon, this time with the aim of establishing a stable presence in the cislunar space. Indeed, this region has gained significant interest over the past decade, serving as a base-ground scenario and testing zone for both several lunar missions and deeper space exploration endeavors. In this regard, the unfolding NASA's Artemis Program aims at setting foot on the Moon for the first time since Apollo 17 in 1972, specifically to create a sustainable human base in the lunar South Pole region [1]. Additionally, the presence of unique gravitational balance points in the Earth-Moon (EM) system, namely the Lagrangian Points L1 and L2, offers numerous opportunities for establishing long-term infrastructure relatively close to the Moon. Indeed, an object positioned at L1 or L2 maintains a fixed position with respect to the rotating primaries, making these points strategic locations for stationing satellites, space telescopes, and even orbiting space stations. These installations may enable continuous monitoring of Earth, Moon, and deep space phenomena, produce a more practical handling of lunar resources, and facilitate spacecrafts assembly and supply for more distant explorations, as for the Deep Space Transport. The future Lunar Orbital Platform-Gateway (LOP-G), previously known as Deep Space Gateway (DSG), represents a collaborative initiative between NASA, ESA, CSA, and JAXA to address these objectives [2, 3]. This long-term platform will be deployed in a stable orbit around L2, positioned at an average distance of 61,500 km from the Moon. In particular, it will be placed in a Southern L2 Near Rectilinear Halo Orbit (NRHO) with a 9:2 Lunar Synodic Resonance and a perilune average radius of 70,000 km, allowing to minimize station keeping and eliminate eclipses almost completely. Therefore, the Lunar Gateway embodies the next frontier of space exploration, serving as a valuable waypoint and operational base for more ambitious missions towards Mars and beyond. Over the years, other several space missions on orbits around EM L1 and L2 have been proposed, but, till now, only the Artemis missions were actually implemented.

However, beyond the study of Lagrangian Points (LPs), the interest of scientific community focuses on the emergence of periodic or quasi-periodic orbits in the cislunar scenario, especially those around L2 [4, 5]. In particular, researchers worldwide have been investigating multiple orbit families, from the more classical Lyapunov, Halo, and Lissajous orbits, to the more recent NRHOs and DROs. All of these invariant structures would play a key role in designing lunar staging orbits, and

facilitating low-energy trajectories both for Earth-to-L2 or Earth-to-Moon transfers [6–8]. At this purpose, strategies like Indirect transfer [9], Weak Stability Boundary [10, 11], or Lunar flyby [12] have been explored. All these approaches capitalize on the unique dynamics of LPs and their associated quasi-stable orbits to enable more efficient and cost-effective trajectories for future space missions.

The present thesis starts from such heritage, proposing to determine valuable trajectories for accessing the cislunar space and inserting satellites into a Moon-centered Distant Retrograde Orbit (DRO). Specifically, this involves modeling a DRO insertion within a multi-body gravitational scenario, by identifying the optimal strategy, among the possible ones, that minimizes the fuel consumption. To achieve this, an iterative shooting procedure based on indirect optimization methods is implemented, leveraging the fundamentals of Optimal Control Theory (OCT). An overview of the current state of research on DROs and optimization methods in space trajectory applications is given below.

1.2 State of the art

DROs are a specific class of Periodic Orbits (POs) in the Earth-Moon three-body system, which combine a retrograde motion, opposite to the Moon's orbiting direction, and large amplitudes. In more general terms, these orbits can be centered in the secondary attractor of any Circular Restricted Three-Body Problem (CR3BP), of which they represent a closed solution. This model considers the dynamics of two main bodies, rotating on circular orbits around a common barycenter, and a smaller third mass of negligible gravitation, and has been extensively adopted for the classical Sun-Earth and Earth-Moon systems.

As early as 1968, Broucke provided initial evidence of the existence of DROs within the CR3BP [13]. Further investigations into DROs are attributed to Hénon [14–18], focusing on the specific Hill's Case model derived from the broader CR3BP framework. In such scenario, Hénon treated different orbits families numerically, investigating their generation and stability properties. Listed in Hénon family f, DROs are indeed characterized by a very high stability due to the interactions with L1 and L2. A comprehensive classification of POs is provided in [15].

As regards the Earth-Moon system, Whitley and Martinez have been compared various types of POs as potential staging orbits in cislunar space [6]. Among the examined options, only NRHOs and DROs have proven to be feasible, due to their high accessibility and minimal eclipse periods. DROs, in particular, exhibit a multi-years stability so that no corrective maneuvers are required. Their general stability has been formally studied in [19, 20]. These unique properties have led DROs to be rediscovered in recent years, paving the way for more in-depth analyses and promising mission concepts. In 2011, NASA proposed the Asteroid Redirect Mission (ARM), intended to visiting a large near-Earth asteroid for collecting samples, by exploiting DROs' stability [21]. Unfortunately, the mission was canceled in 2017. Notably, DROs was even considered as a cost-effective alternative to NRHOs for stationing the Lunar Gateway.

Among all the proposed missions involving DROs, NASA's Artemis I stands out as the only one that has been developed and completed [22]. Launched in 2022, this uncrewed mission served as a testing flight of the Orion spacecraft and Space Launch System rocket (SLS) in preparation for subsequent Artemis missions. After separation from the upper stage, the capsule performed a Trans-Lunar Injection (TLI) on a Moon-centered DRO, flew-by around the Moon, and then returned to Earth [23]. The Orion spent a total of three weeks in space, 6 days of which on orbit, approaching approximately to a distance of 130 km from the lunar surface during fly-bys. Further details on mission design and a complete optimization analysis of the Artemis I trajectory are given in [24, 25].

In literature, several works have investigated how to exploit DROs as low-energy transfer orbits in the EM CR3BP [26–28]. Indeed, it is possible to study their dynamical evolution and leverage the manifolds for maneuvering at much lower costs compared to traditional operations in the Keplerian model [29, 30]. Different mission scenarios for a transfer to DROs are explored in [31]; these solutions for DRO insertion range from exploiting the adjacent Lyapunov orbits at L1 and L2 to performing a powered lunar fly-by (exactly like Artemis I) or even undertaking a more complex direct transfer. Recent contributions have directly analyzed a transfer from an initial parking DRO to Low Lunar Orbits [32]. A diverse scenario is proposed in [33], where a LEO-to-DRO transfer is coupled with a rendezvous maneuver on lunar orbits for future space outposts or supply stations. Conte, moreover, examines DROs as support trajectories for refueling during deeper space missions [34, 35].

However, the majority of these studies encompasses various differential correction and numerical optimization methods to identify feasible trajectories that ensure minimal cost while addressing mission requirements. For this reason, the following section provides a brief introduction to space trajectory optimization, the principles of which are widely used in this thesis.

1.3 Optimization methods in space trajectories

The origins of Optimal Control Theory (OCT) date back to the 18th century, anchored in Euler and Lagrange's studies on Calculus of Variations (CoV), of which the OCT represents an extension [36–38]. However, it was not until the mid-20th century that OCT gained prominence, finding significant applications in the then newborn aerospace industry [39–42]. In particular, the need to overcome the limit imposed by the maximum transportable propellant, along with the existing mission constraints, created fertile ground for optimization in space trajectories. By reducing propellant requirements for a fixed spacecraft mass, more payload can be carried onboard, which is the primary scope of any mission concept.

Historically, two different types of optimization methods have been implemented to solve boundary value problems: direct and indirect methods [43]. Direct methods perform a transcription of the original problem in to a new finite-dimensional one; all continuous functions are discretized into a refined mesh, requiring a large number of variables to describe the problem. Direct methods generally exhibit an higher robustness compared to indirect methods, often reaching the final solution even without a complete understanding of the scenario. However, this may result in a suboptimal solution, not an optimal one, which requires further refinement techniques to tackle scarce accuracy.

Indirect methods, instead, are generally faster due to a smaller set of describing variables. Starting from initial guesses, they can achieve accurate optimal solutions, by offering theoretical insights which guide the procedure. For this reason, the indirect approach is preferred in this thesis, offering a better comprehension of the problem. However, necessary conditions for optimality have to be retrieved for the specific case study. Indirect methods introduce additional variables, or costates, related to the original ones, thus producing an augmented boundary value problem. Given their sensitivity to initial conditions, these methods has to be improved through

tailored control strategies, capable to aid convergence. A detailed analysis and comparison between these two numerical approaches is provided in Chapter 3.

1.4 Main objectives

This thesis fits perfectly with the described framework, focusing on the optimization of direct transfer trajectories to a lunar DRO within the CR3BP model. The analysis relies on the indirect formulation to compose a two-point boundary value problem. Specifically, a single-shooting algorithm based on Newton's method is implemented, assuming a *bang-bang* thrust control strategy. The Pontryagin's Maximum Principle (PMP) is adopted to ensure the optimality of solutions.

As anticipated, the examined scenario involves an Earth-to-Moon transfer trajectory, followed by a Distant Retrograde Orbit Insertion (DRI) maneuver. The aim is to identify the optimal trajectory at minimum propellant request that fulfills all boundary conditions. First off, such DRO has to be generated; the abovementioned shooting procedure allows to compute a completely closed orbit in the CR3BP, then targeted as final condition for the actual optimization process.

Therefore, this thesis operates on two different fronts; on one hand, it confirms the enduring human attractiveness to the Moon, specifically the renewed scientific interest in cislunar space operations. On the other hand, it provides a powerful tool, based on the indirect optimization, that can be broadly applied -with minor adjustments- to various types of optimal control problems. Such necessity arises from Mascolo's extensive research [44], of which this work is a derivative.

The main objectives of this thesis are:

- Unify and improve the results of previous research within the framework of lunar transfers and cislunar operations on DROs.
- Develop an automated tool to generate periodic orbits in the CR3BP model, providing a starting solution for the optimization problem of the case study.
- Implement a single-shooting algorithm that leverages the benefit of indirect methods to identify an optimal, cost-effective trajectory while satisfying mission requirements and constraints.

- Investigate the characteristics of stable periodic orbits in the vicinity of the Moon, providing useful considerations for future mission concepts.

1.5 Thesis overview

The overall structure of the thesis is outlined as follows.

Chapter 2 discusses the dynamical model adopted for the whole analysis. A preliminary overview of the two-body problem is provided to clearly understand the scenario under investigation. The three-body problem, specifically the CR3BP, is introduced, including its main assumptions and respective equations of motion, with a focus on the existence of equilibrium points. Finally, the n-body problem is briefly mentioned for completeness.

Chapter 3 explores the generation of periodic orbits in the three-body model via differential correction. In particular, a single-shooting method is presented, serving as a baseline for the main optimization procedure. Some considerations about how such orbits would be transitioned in a higher-fidelity model are also provided.

Chapter 4 delves into the Optimal Control Theory, offering a detailed comparison between direct and indirect methods. The original scenario is transformed in a Two-Point Boundary Value Problem (TPBVP) and an effective thrust control strategy is adopted. Numerical techniques and manipulations to improve the indirect optimization procedure are extensively discussed in their main aspects.

Chapter 5 introduces the scenario under investigation, where a DRO insertion in the Earth-Moon system is completely performed. The analysis aims at identify the optimal trajectory for the case study, applying the OCT principles previously discussed. The problem's Boundary Conditions (BCs) are specified, and opportune strategies complying with the Pontryagin's Maximum Principle are implemented to ensure optimality.

Chapter 6, in conclusion, summarizes the final results of this thesis, followed by some suggestions on potential improvements and future research directions.

Chapter 2

Dynamic models

Chapter 2 offers a comprehensive description of the adopted dynamical model.

First off, the Chapter introduces the main assumptions underlying the two-body problem formulation. This includes preliminary considerations on classical orbital parameters and the reference systems used to describe the Spacecraft (SC) motion. In subsequent sections, a detailed overview of the three-body problem is provided, with a specific focus on the CR3BP model, extensively employed in this thesis. The CR3BP Equations of Motion (EoMs), along with the definition of gravitational equilibrium points and Zero Velocity Surfaces (ZVSs) are also discussed. At the end, the n-Body Problem (NBP) is briefly reported, mentioning the most commonly used perturbations to add complexity to the scenario. However, only those elements necessary for laying the groundwork of later analysis are explored. Further details on the fundamentals of orbital mechanics can be found in the eminent works cited in references [45–49].

The following notation, unless otherwise specified, will be employed throughout this thesis; vectors will be presented as column vectors in bold lowercase fonts, except for known quantities (e.g., velocity $\boldsymbol{V}$ and thrust $\boldsymbol{T}$), while matrices will be in bold uppercase letters ($\boldsymbol{A}$); unit vectors, again in bold lowercase fonts, are denoted by a hat ($\hat{\boldsymbol{x}}$); first or multiple-orders time derivatives will be respectively marked with one or multiple dots, for both scalar and vector quantities ($\dot{x}$, $\ddot{x}$, $\dot{\boldsymbol{x}}$, $\ddot{\boldsymbol{x}}$); a tilde superscript ($\tilde{\boldsymbol{x}}$) as well as Greek letters or Calligraphic fonts will be used to distinguish nondimensional quantities from dimensional ones.

2.1 Two-Body Problem

The Two-Body Problem (2BP) is the first approximate representation used in orbital mechanics to describe the motion of massive bodies under their mutual gravitational attraction. Also known as *Kepler problem*, this model simplifies the complexities of multi-body interactions by reducing the system to only two bodies, allowing for an exact analytical solution.

More precisely, the 2BP main assumptions are:

- The two bodies are considered as point particles.
- Masses are constant, with $m \ll M$.
- No additional forces, except for gravity, are considered.

Given that one body (i.e. the SC) is much smaller than the other, its mass is assumed to be negligible which gives the epithet *restricted* to the model. This means that such a small body does not exert any influence on the primary, but is only affected by its gravitation.

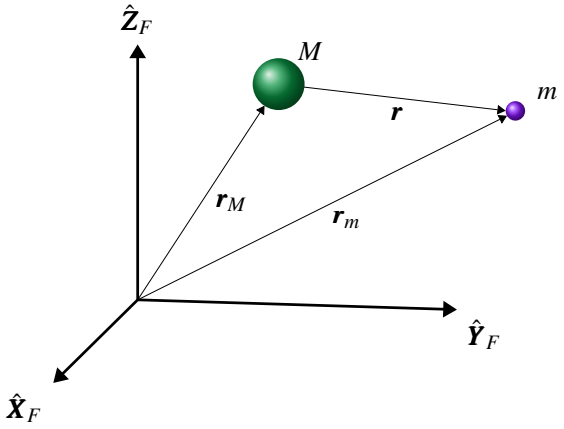

Fig. 2.1 Representation of the 2BP in a generic inertial RF $\{\hat{\boldsymbol{X}}_F, \hat{\boldsymbol{Y}}_F, \hat{\boldsymbol{Z}}_F\}$.

From Newton's law of universal gravitation, considering two bodies at a relative distance of $\boldsymbol{r} = \boldsymbol{r}_M - \boldsymbol{r}_m$ in a generic reference frame $\{\hat{\boldsymbol{X}}_F, \hat{\boldsymbol{Y}}_F, \hat{\boldsymbol{Z}}_F\}$, the following expression holds:

$$\ddot{\boldsymbol{r}} \approx -\frac{GM}{r^2}\frac{\boldsymbol{r}}{r} = -\frac{\mu}{r^2}\frac{\boldsymbol{r}}{r}. \tag{2.1}$$

Therefore, the set of 2BP Equations of Motion (EoMs) is easily obtained:

$$\ddot{\boldsymbol{r}} + \frac{\mu}{r^2}\frac{\boldsymbol{r}}{r} = \boldsymbol{0}, \tag{2.2}$$

where $G \approx 6.67 \times 10^{-20}$ km^3/kg/s^2 is the universal gravitational constant, while $\mu = GM$ is the planetary gravitational parameter. Values of μ for different main bodies are provided in table 2.1.

Table 2.1 Planetary gravitational parameters for different primaries in the Solar system.

Bodies	μ $[km^3/s^2]$
Sun	1.3271×10^{11}
Earth	3.9860×10^5
Moon	4.9028×10^3

After some mathematical manipulations, two constants of motion can be derived for the purposes of this discussion. The first quantity is the specific mechanical energy $\mathscr{E}$, clearly defined in the so-called *vis-viva* equation:

$$\mathscr{E} = \frac{V^2}{2} - \frac{\mu}{r}, \tag{2.3}$$

where the first and second terms are respectively the specific kinetic and potential contributions. Such energy remains constant for any orbit in the 2BP domain and is strictly related to the shape of orbit itself:

$$\mathscr{E} = -\frac{\mu}{2a}. \tag{2.4}$$

Depending on values assumed by $\mathscr{E}$, the trajectory in question can be a closed orbit (for ellipses, $\mathscr{E} < 0$) or an open one (for parabolas, $\mathscr{E} = 0$ while, for hyperbolae, $\mathscr{E} > 0$).

The second conservation law regards the aforementioned specific angular momentum:

$$\boldsymbol{h} = \boldsymbol{r} \times \boldsymbol{V}. \tag{2.5}$$

These considerations lead to several key concepts in astrodynamics, such as Kepler's laws and closed-form equations for orbit determination, laying the ground-

work for understanding more complex analyses. Further details can be found in [45, 47, 48].

2.1.1 EME2000 reference systems

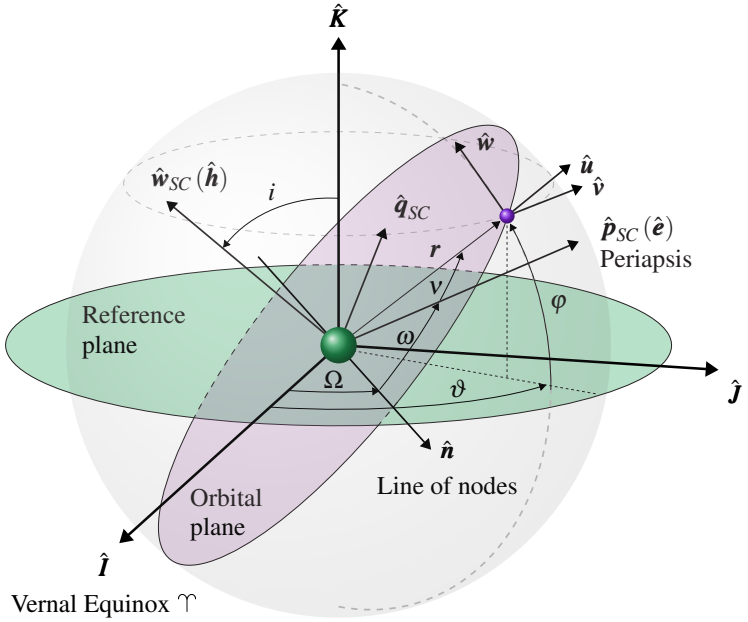

Fig. 2.2 EME2000 $\{\hat{\boldsymbol{I}},\hat{\boldsymbol{J}},\hat{\boldsymbol{K}}\}$, perifocal $\{\hat{\boldsymbol{p}}_{SC},\hat{\boldsymbol{q}}_{SC},\hat{\boldsymbol{w}}_{SC}\}$, and ZEN $\{\hat{\boldsymbol{u}},\hat{\boldsymbol{v}},\hat{\boldsymbol{w}}\}$ RFs.

A generic Reference System (RS) is uniquely defined by a right-hand triad of mutually orthogonal axes centered in its origin and lying on its fundamental plane, thus composing the specific Reference Frame (RF). Two different types of RFs exist: inertial and non-inertial, primarily distinguished by their state of motion. Indeed, in the first ones an object remains at rest or moves at a constant velocity, in absence of any external force. Conversely, non-inertial RFs are characterized by their own acceleration or rotation, which gives rise to apparent forces, such as Coriolis centrifugal accelerations. The selection of an appropriate RS depends on the particular analysis being conducted; the motion of a satellite with respect to Earth, is more conveniently implemented by employing an inertial reference frame.

For the 2BP, an equatorial geocentric quasi-inertial RS is generally adopted, specifically the Earth Mean Equator and Equinox of Epoch J2000 (EME2000). As depicted in Figure 2.2, such RF, also directly called J2000, presents its origin at

the Earth's center and the equatorial plane as its fundamental one. Its unit vectors, indicating the three axes directions, are: $\hat{\boldsymbol{I}}$ aligned toward the direction of Vernal Equinox, $\hat{\boldsymbol{K}}$ normal to the reference plane, and $\hat{\boldsymbol{J}}$ completing the right-handed triad.

To easily describe the satellite motion, the EME2000 can be accompanied by other two reference systems:

- The non-inertial perifocal RF, $\{\hat{\boldsymbol{p}}_{SC}, \hat{\boldsymbol{q}}_{SC}, \hat{\boldsymbol{w}}_{SC}\}$, whose two main axes $\hat{\boldsymbol{p}}_{SC}$ and $\hat{\boldsymbol{w}}_{SC}$ are respectively aligned with the eccentricity $\hat{\boldsymbol{e}}$ and the specific angular momentum $\hat{\boldsymbol{h}}$ vectors directions, while $\hat{\boldsymbol{q}}_{SC}$ ends the triad.
- The topocentric, non-inertial Zenith-East-North (ZEN) RF, $\{\hat{\boldsymbol{u}}, \hat{\boldsymbol{v}}, \hat{\boldsymbol{w}}\}$, whose axes coincide with the radial, tangential, and normal directions of the satellite's velocity components $\{\hat{\boldsymbol{u}}, \hat{\boldsymbol{v}}, \hat{\boldsymbol{w}}\}$.

The coordinates of a vector can be expressed in any of these reference systems; in that sense, it is necessary to perform a conversion between different RFs using proper elementary rotation matrices, which are composed of a set of Direction Cosine Matrices (DCMs). Since the purpose of this Section is only to provide a general overview of the 2BP, the implementation of such matrices is not discussed.

2.1.2 Conic equation

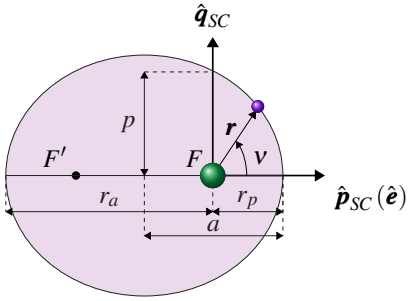

Fig. 2.3 Perifocal reference plane.

Assuming a closed orbit not subject to any external perturbation, a spacecraft would follow a conic path indefinitely, in accordance with the Kepler's First Law. Such a conic can be precisely described by using a set of classical Keplerian parameters $\{a, e, i, \Omega, \omega, \nu\}$, which uniquely define its configuration and orientation in space.

Specifically, the semi-major axis a, namely the half distance between the apsides, determines the orbit's dimensions, while its shape depends on the eccentricity e, quantifying the deviation from a circle; these two elements are often linked via another Keplerian parameter, the semilatus rectum $p = a(1-e^2)$. The true anomaly ν specifies the SC's angular position with respect to periapsis, the closest point to the main body. The mean anomaly M can also be used for this purpose. However, these three elements are sufficient to define the SC's position on a specific orbit in the perifocal RF. They are related to each other by the well-known *conic equation*:

$$r = \frac{a(1-e^2)}{1+e\cos\nu}. \tag{2.6}$$

In order to complete the representation in three-dimensional space (with respect to the EME2000), the remaining three Keplerian parameters are required. Indeed, the inclination i quantifies how much the orbital plane may be inclined with respect to the reference equatorial plane. The intersection between these two planes is the line of nodes $\hat{\boldsymbol{n}}$, along which the passage of from the southern to the northern hemisphere and viceversa respectively occurs at two reference points, namely the ascending and descending nodes. The right ascension of the ascending node (RAAN) Ω specifies the orientation of this line, measured from the $\hat{\boldsymbol{I}}$ axis, heading towards the ascending node. The last parameter is the argument of periapsis ω, which indicates the position of pariapsis relative to the line of nodes, provided that Ω is defined (i.e. for non-circular and non-equatorial orbits). Figure 2.3 clearly shows the fundamental plane of the aforementioned perifocal RF, where the satellite's orbit lies and all these parameters are explicitly defined.

2.1.3 2BP Equations of Motion

The evolution of SC's state in the 2BP over time can be described by the following set of governing ODEs:

$$\frac{d\boldsymbol{r}}{dt} = \boldsymbol{V} \tag{2.7a}$$

$$\frac{d\boldsymbol{V}}{dt} = \boldsymbol{g}_0 + \frac{\boldsymbol{T}}{m} + \frac{\boldsymbol{L}}{m} + \frac{\boldsymbol{D}}{m} + \mathbf{a}_p \tag{2.7b}$$

$$\frac{dm}{dt} = -\frac{\boldsymbol{T}}{c}. \tag{2.7c}$$

where the EME2000 RF is considered. The first two lines, (2.7a) and (2.7b), specify the variations in terms of SC's position $\boldsymbol{r}$ and velocity $\boldsymbol{V}$ under different influences and perturbations. In particular, besides the thrust vector $\boldsymbol{T}$, other accelerations are taken into account, such as the aerodynamic forces -namely the lift $\boldsymbol{L}$ and the drag $\boldsymbol{D}$- and possible external perturbations $\mathbf{a}_p$. The last equation, (2.7c), refers to the propulsive system, representing the decrease in mass due to fuel consumption. The term $\boldsymbol{g}_0$ is the gravitational acceleration, as per equation (2.1):

$$\boldsymbol{g}_0 = -\frac{\mu}{r^2}\frac{\boldsymbol{r}}{r}. \tag{2.8}$$

If only such force is present without any external acceleration, all these quantities can be integrated analytically in the 2BP domain.

2.2 Three-Body Problem

This section delves into the Three-Body Problem (3BP) formulation, a model that more accurately reflects the real-scenario conditions.

Differently from the 2BP, which provides an elegant analytical solution for the dynamic system, the addition of a third body in the 3BP introduces a level of complexity that precludes closed-form solutions for the EoMs. As a result, the predictable conic paths typical of a two-body interaction give way to more elaborate trajectories, shaped by the mutual gravitational influences of the three bodies involved. In particular, the model of the Circular Restricted Three-Body Problem (CR3BP) is presented here, which, under specific assumptions, is sufficient to preliminarily elucidate these complex interactions and set the stage for understanding a multi-body gravitational scenario.

Considering a generic binary system, the 3BP implies the presence of two main bodies, with masses m_1 and m_2 respectively for the bigger and smaller one, revolving around their barycenter and a third body representing the spacecraft. As a fundamental hypothesis of the CR3BP, the third mass is smaller than the primaries, so its gravitational contribution is assumed negligible [49, 45].

2.2.1 Synodic reference frame

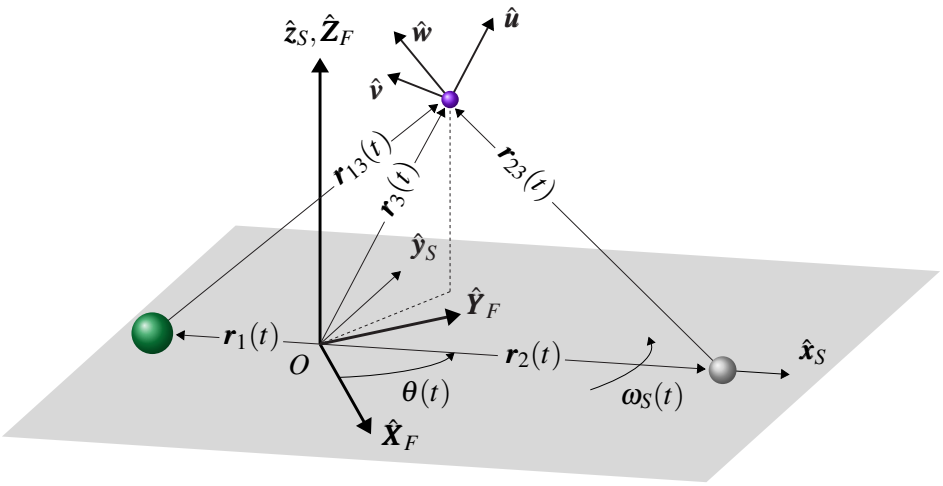

Fig. 2.4 Synodic RF $\{\hat{x}_S, \hat{y}_S, \hat{z}_S\}$ in a generic binary system (not in scale).

A schematic representation of the three-body scenario is provided in Figure 2.4. When the two primary bodies are observed from an inertial RS $\{\hat{X}_F, \hat{Y}_F, \hat{Z}_F\}$, their mutual angular speed $\omega_S(t)$ arises. The non-inertial rotating reference system $\{\hat{x}_S, \hat{y}_S, \hat{z}_S\}$, known as the *synodic* RF, is centered in the barycenter and follows the main bodies' motion; the direction of $\hat{x}_S$ axis coincides with the line joining the two bodies, the $\hat{z}_S$ axis is normal to their orbital plane, and the $\hat{y}_S$ axis completes the triad. Such a whole framework exactly resembles the Earth-Moon system, where a small generic object (i.e. the SC) freely moves in the 3D space under the mutual influence of both the Earth and Moon. Similarly, the dynamics of the 3BP can also be applied to the Sun-Earth-Moon system, where our satellite takes the role of third body.

A generic distance between any two bodies is denoted with the vector:

$$\boldsymbol{r}_{ij}(t) = \boldsymbol{r}_i(t) - \boldsymbol{r}_j(t), \tag{2.9}$$

where the element $\boldsymbol{r}_i(t) = \boldsymbol{r}_{Oi}(t)$ indicates the i-th body's position with respect to the origin O. Therefore, the vector $\boldsymbol{r}_{12}(t)$ represents the distance between the two primaries, to which the rotation rate $\omega_S(t)$ is strictly related. The dimensional mean

motion for the binary system then can be expressed as:

$$n(t) = \sqrt{\frac{\mu_1 + \mu_2}{r_{12}^3(t)}} = \sqrt{\frac{\mu^*}{r_{12}^3(t)}}, \tag{2.10}$$

where μ^* is the sum of the specific gravitational parameters of the primaries μ_1 and μ_2. Hence, the angle θ between an inertial RS and the synodic RF can be easily computed by multiplying the mean motion to the elapsed time t, measured in seconds:

$$\theta(t) = n(t) \cdot t, \tag{2.11}$$

In general, since the distance $\boldsymbol{r}_{12}(t)$ varies over time, the mean motion and the angle θ exhibit a roto-pulsating behaviour as the ephemerides and the eccentricity of Keplerian orbits are considered in the analysis. However, the transition to CR3BP is completed by assuming that the main bodies describe two perfect *circular* Keplerian orbits around their barycenter. With this further simplification, the primaries' position vectors $r_i(t) = r_i$ become time-independent in magnitude and, therefore, the mean motion remains constant, resulting in a prograde θ that varies linearly over time with a constant angular velocity ω_S.

To enhance numerical precision, the quantities of the CR3BP are typically nondimensionalized with respect to the following characteristic values:

$$\begin{cases} \ell^* = r_1 + r_2 & \text{(2.12a)} \\ m^* = m_1 + m_2 & \text{(2.12b)} \\ \mathscr{T}^* \triangleq \sqrt{\dfrac{(\ell^*)^3}{Gm^*}}. & \text{(2.12c)} \end{cases}$$

Specifically, the characteristic length ℓ^* is the fixed mean distance between the two main bodies, while the characteristic mass m^* is the sum of their masses; the characteristic time $\mathscr{T}^*$ is implicitly derived by imposing that the nondimensional universal gravitational constant equals the unity in the Kepler's Third Law formulation.

Therefore, the nondimensional quantities for distances, masses, and times are obtained:

$$\begin{cases} \rho_{12} = \dfrac{r_{12}}{\ell^*} = 1 & \text{(2.13a)} \\ \mu \triangleq \dfrac{m_2}{m^*} & \text{(2.13b)} \\ \tau = \dfrac{\mathscr{T}}{\mathscr{T}^*} = 2\pi & \text{(2.13c)} \end{cases}$$

With some mathematical steps, the nondimensional mass ratios can be easily retrieved:

$$\mu \triangleq \frac{\mu_2}{\mu^*}, \tag{2.14a}$$

$$\frac{\mu_1}{\mu^*} = 1 - \mu. \tag{2.14b}$$

Similarly, the barycenter position with respect to the first primary is:

$$\rho_{CG} = \frac{\sum \rho_i \mu_i}{\sum \mu_i} = \mu, \tag{2.15}$$

and, so:

$$\rho_1 = \frac{r_1}{\ell^*} = -\mu \tag{2.16a}$$

$$\rho_2 = \frac{r_2}{\ell^*} = 1 - \mu. \tag{2.16b}$$

2.2.2 CR3BP Equations of Motion

The compact dimensional form of the CR3BP EoMs is derived from Newton's Second Law (NSL):

$$\ddot{\boldsymbol{r}} = -\frac{\mu_1}{r_{13}^2}\frac{\boldsymbol{r}_{13}}{r_{13}} - \frac{\mu_2}{r_{23}^2}\frac{\boldsymbol{r}_{23}}{r_{23}}, \tag{2.17}$$

where the SC position vectors with respect to the main bodies can be generalized as:

$$\boldsymbol{r}_{i3} = \boldsymbol{r}_3 - \boldsymbol{r}_i \quad i = 1, 2. \tag{2.18}$$

Henceforth, given that the primaries are not influenced by the SC, its subscript 3 is omitted for brevity and SC's coordinates simply coincide with $\{x, y, z\}$ values.

In the synodic RF, the EoMs projected into the three directions take the form:

$$\ddot{x} = -\frac{\mu_1}{r_{13}^3}(x - x_1) - \frac{\mu_2}{r_{23}^3}(x - x_2) \tag{2.19a}$$

$$\ddot{y} = -\frac{\mu_1}{r_{13}^3}y - \frac{\mu_2}{r_{23}^3}y \tag{2.19b}$$

$$\ddot{z} = -\frac{\mu_1}{r_{13}^3}z - \frac{\mu_2}{r_{23}^3}z. \tag{2.19c}$$

where the relative position vectors are:

$$r_{i3} = \sqrt{(x - x_i)^2 + y^2 + z^2}, \quad i = 1, 2. \tag{2.20}$$

In order to project the EoMs in the inertial RF, the transport theorem must be employed. Indeed, for a generic variable f:

$$\frac{df^F}{dt} = \frac{df^R}{dt} + \boldsymbol{\omega}_S^{R/F} \times f^R, \tag{2.21}$$

where the superscripts F and R respectively refer to fixed and synodic RFs, and R/F suggests that such quantity is measured in the rotating RF with respect to the inertial one. Therefore, the inertial velocity is:

$$\dot{\boldsymbol{r}}^F = \frac{d\boldsymbol{r}^F}{dt} = \frac{d\boldsymbol{r}^R}{dt} + \boldsymbol{\omega}_S^{R/F} \times \boldsymbol{r}^R, \tag{2.22}$$

while the acceleration can be computed as:

$$\begin{aligned}
\ddot{\boldsymbol{r}}^F &= \frac{d\dot{\boldsymbol{r}}^F}{dt} = \frac{d^R\dot{\boldsymbol{r}}^F}{dt} + \boldsymbol{\omega}_S^{R/F} \times \dot{\boldsymbol{r}}^F \\
&= \frac{d^R}{dt}\left(\dot{\boldsymbol{r}}^R + \boldsymbol{\omega}_S^{R/F} \times \boldsymbol{r}^R\right) + \boldsymbol{\omega}_S^{R/F} \times \left(\dot{\boldsymbol{r}}^R + \boldsymbol{\omega}_S^{R/F} \times \boldsymbol{r}^R\right) \\
&= \ddot{\boldsymbol{r}}^R + \dot{\boldsymbol{\omega}}_S^{R/F} \times \boldsymbol{r}^R + \boldsymbol{\omega}_S^{R/F} \times \dot{\boldsymbol{r}}^R + \boldsymbol{\omega}_S^{R/F} \times \dot{\boldsymbol{r}}^R + \boldsymbol{\omega}_S^{R/F} \times \left(\boldsymbol{\omega}_S^{R/F} \times \boldsymbol{r}^R\right) \\
&= \ddot{\boldsymbol{r}} + \dot{\boldsymbol{\omega}}_S \times \boldsymbol{r} + 2\boldsymbol{\omega}_S \times \dot{\boldsymbol{r}} + (\boldsymbol{\omega}_S \times \boldsymbol{r}).
\end{aligned} \tag{2.23}$$

In the last line, the superscripts are dropped for brevity, since all terms are referred to the rotating RF. The first term in the Right-Hand Side (RHS) is the rotating

acceleration, whereas the other three terms represent respectively the tangential, centripetal, and Coriolis accelerations. Under the CR3BP assumptions, given that the considered orbits are circular, no variation of both ω_S and position vector norm arise, thus the tangential and centripetal accelerations are both null. The sole Coriolis acceleration remains for any rotating frame. Moreover, one has:

$$\boldsymbol{\omega}_S = \omega_S \hat{\mathbf{z}}_S, \tag{2.24}$$

where, from the Kepler's Third Law:

$$\omega_S = \sqrt{\frac{\mu_1 + \mu_2}{r_{12}^3}}. \tag{2.25}$$

However, by explicitly expressing the quantities in equation (2.23) for the most generic case in the 3BP, the velocity shows the following components:

$$\begin{aligned}
\dot{\boldsymbol{r}}^F &= (\dot{x}\hat{\mathbf{x}}_S + \dot{y}\hat{\mathbf{y}}_S + \dot{z}\hat{\mathbf{z}}_S) + \begin{vmatrix} \hat{\mathbf{x}}_S & \hat{\mathbf{y}}_S & \hat{\mathbf{z}}_S \\ 0 & 0 & \omega_S \\ x & y & z \end{vmatrix} \\
&= (\dot{x}\hat{\mathbf{x}}_S + \dot{y}\hat{\mathbf{y}}_S + \dot{z}\hat{\mathbf{z}}_S) + [(-y\omega_S)\hat{\mathbf{x}}_S - (-x\omega_S)\hat{\mathbf{y}}_S + (0)\hat{\mathbf{z}}_S] \\
&= (\dot{x} - y\omega_S)\hat{\mathbf{x}}_S + (\dot{y} + x\omega_S)\hat{\mathbf{y}}_S + (\dot{z})\hat{\mathbf{z}}_S,
\end{aligned} \tag{2.26}$$

whereas for the acceleration:

$$\begin{aligned}
\ddot{\boldsymbol{r}}^F &= \ddot{\boldsymbol{r}} + \dot{\boldsymbol{\omega}}_S \times \boldsymbol{r} + 2\boldsymbol{\omega}_S \times \dot{\boldsymbol{r}} + \boldsymbol{\omega}_S \times (\boldsymbol{\omega}_S \times \boldsymbol{r}) \\
&= \ddot{\boldsymbol{r}} + \begin{vmatrix} \hat{\mathbf{x}}_S & \hat{\mathbf{y}}_S & \hat{\mathbf{z}}_S \\ 0 & 0 & \dot{\omega}_S \\ x & y & z \end{vmatrix} + 2 \begin{vmatrix} \hat{\mathbf{x}}_S & \hat{\mathbf{y}}_S & \hat{\mathbf{z}}_S \\ 0 & 0 & \omega_S \\ \dot{x} & \dot{y} & \dot{z} \end{vmatrix} + \begin{vmatrix} \hat{\mathbf{x}}_S & \hat{\mathbf{y}}_S & \hat{\mathbf{z}}_S \\ 0 & 0 & \omega_S \\ x & y & z \end{vmatrix} \\
&= (\ddot{x} - 2\dot{y}\omega_S + y\dot{\omega}_S)\hat{\mathbf{x}}_S + (\ddot{y} + 2\dot{x}\omega_S + x\dot{\omega}_S)\hat{\mathbf{y}}_S + (\ddot{z})\hat{\mathbf{z}}_S + \begin{vmatrix} \hat{\mathbf{x}}_S & \hat{\mathbf{y}}_S & \hat{\mathbf{z}}_S \\ 0 & 0 & \omega_S \\ -y\omega_S & x\omega_S & 0 \end{vmatrix} \\
&= (\ddot{x} - 2\dot{y}\omega_S - y\dot{\omega}_S - x\omega_S^2)\hat{\mathbf{x}}_S + (\ddot{y} + 2\dot{x}\omega_S + x\dot{\omega}_S - y\omega_S^2)\hat{\mathbf{y}}_S + (\ddot{z})\hat{\mathbf{z}}_S.
\end{aligned} \tag{2.27}$$

Equalling equations (2.19) and (2.27) component by component yields:

$$\ddot{x} - 2\dot{y}\omega_S - y\dot{\omega}_S - x\omega_S^2 = -\frac{\mu_1}{r_{13}^3}(x - x_1) - \frac{\mu_2}{r_{23}^3}(x - x_2) \tag{2.28a}$$

$$\ddot{y} + 2\dot{x}\omega_S + x\dot{\omega}_S - y\omega_S^2 = -\frac{\mu_1}{r_{13}^3}y - \frac{\mu_2}{r_{23}^3}y \tag{2.28b}$$

$$\ddot{z} = -\frac{\mu_1}{r_{13}^3}z - \frac{\mu_2}{r_{23}^3}z. \tag{2.28c}$$

Both for a historical convention and numerical accuracy, the SC's coordinates and position vector in the CR3BP are nondimensionalized as follows:

$$\begin{cases} \xi = \dfrac{x}{\ell^*} & \text{(2.29a)} \\ \eta = \dfrac{y}{\ell^*} & \text{(2.29b)} \\ \zeta = \dfrac{z}{\ell^*} & \text{(2.29c)} \\ \rho = \dfrac{r}{\ell^*} & \text{(2.29d)} \end{cases}$$

Given that there are no roto-pulsating behaviours, one has a nondimensional angular velocity $w_S = \omega_S/\omega_S^* = 1$ and thus $\dot{w}_S = 0$. Therefore, the full set of nondimensional ODEs in the CR3BP dynamic model is:

$$\ddot{\xi} - 2\dot{\eta} - \xi = -\frac{1-\mu}{{\rho_{13}}^3}(\xi + \mu) - \frac{\mu}{{\rho_{23}}^3}[\xi - (1-\mu)] \tag{2.30a}$$

$$\ddot{\eta} + 2\dot{\xi} - \eta = -\frac{1-\mu}{{\rho_{13}}^3}\eta - \frac{\mu}{{\rho_{23}}^3}\eta \tag{2.30b}$$

$$\ddot{\zeta} = -\frac{1-\mu}{{\rho_{13}}^3}\zeta - \frac{\mu}{{\rho_{23}}^3}\zeta. \tag{2.30c}$$

As anticipated, such complex dynamics lead to unpredictable trajectories influenced by the third body's gravitation. Indeed, unlike the closed conics seen in Section 2.1.2 for the 2BP, CR3BP orbits cannot be defined by Keplerian elements, as they generally exhibit irregular shapes and unstable behaviors.

2.2.3 Jacobi integral

The Jacobi integral is the sole, consistent pseudo-integral of motion that is conserved in the dynamics of the CR3BP. Within the rotating synodic RF, it allows to investigate which regions are accessible to the third body and identify areas where escapes or collisions are not possible under the CR3BP assumptions. As a central element in orbital mechanics, the Jacobi integral is invaluable for planning space mission trajectories and analyzing orbital stability. It is derived by first defining the potential function U in the inertial RF:

$$U^F = \sum_{i=1}^{2} \frac{\mu_i}{r_{i3}}, \tag{2.31}$$

where i indicates a generic gravitational body while 3 refers to the SC. By projecting this in the rotating RF, the centrifugal potential is also considered:

$$U^R = \frac{\mu_1}{r_{13}} + \frac{\mu_2}{r_{23}} + \frac{1}{2}\omega_S(x^2+y^2), \tag{2.32}$$

or, in nondimensional form, the pseudopotential arises:

$$\mathscr{U}^R = \frac{1-\mu}{\rho_{13}} + \frac{\mu}{\rho_{23}} + \frac{1}{2}(\xi^2+\eta^2). \tag{2.33}$$

Deriving such quantity with respect to the nondimensional coordinates:

$$\frac{\partial \mathscr{U}}{\partial \xi} = \xi - \frac{1-\mu}{\rho_{13}^3}(\xi+\mu) - \frac{\mu}{\rho_{23}^3}[\xi-(1-\mu)] \tag{2.34a}$$

$$\frac{\partial \mathscr{U}}{\partial \eta} = \eta - \frac{1-\mu}{\rho_{13}^3}\eta - \frac{\mu}{\rho_{23}^3}\eta \tag{2.34b}$$

$$\frac{\partial \mathscr{U}}{\partial \zeta} = -\frac{1-\mu}{\rho_{13}^3}\zeta - \frac{\mu}{\rho_{23}^3}\zeta. \tag{2.34c}$$

By combining equations (2.30) and (2.34) one obtains:

$$\ddot{\xi} - 2\dot{\eta} = \frac{\partial \mathscr{U}}{\partial \xi} \tag{2.35a}$$

$$\ddot{\eta} + 2\dot{\xi} = \frac{\partial \mathscr{U}}{\partial \eta} \tag{2.35b}$$

$$\ddot{\zeta} = \frac{\partial \mathscr{U}}{\partial \zeta}. \tag{2.35c}$$

Moreover, multiplying each of the dimensional equations in (2.28) by $2\dot{x}$, $2\dot{y}$, $2\dot{z}$, and then summing them results in:

$$2\ddot{x}\dot{x}+2\ddot{y}\dot{y}+2\ddot{z}\dot{z}+2\omega_S^2(\dot{x}x+\dot{y}y)=2\dot{x}\frac{\partial U}{\partial x}+2\dot{y}\frac{\partial U}{\partial y}+2\dot{z}\frac{\partial U}{\partial z}=2\frac{dU}{dt}, \tag{2.36}$$

by integrating which, the Jacobian integral equation arises:

$$\dot{x}^2+\dot{y}^2+\dot{z}^2=V^2=2U-J_C. \tag{2.37}$$

The term on the Left-Hand Side (LHS) represents the velocity squared V^2 in the synodic RF. In the RHS, the pseudopotential U includes the integrated term $\omega_S(x^2+y^2)$, whereas J_C is commonly known as the *Jacobi Constant*. Such a constant of motion can be seen as an inverse mechanical energy-like quantity, sum of the kinetic and potential energy contributions. Hence, an higher J_C implies less energy for the SC in the rotating frame. In the nondimensional synodic form one has:

$$\dot{\xi}^2+\dot{\eta}^2+\dot{\zeta}^2=\mathcal{V}^2=2\mathscr{U}-\mathscr{J}_C. \tag{2.38}$$

2.2.4 Lagrangian Points

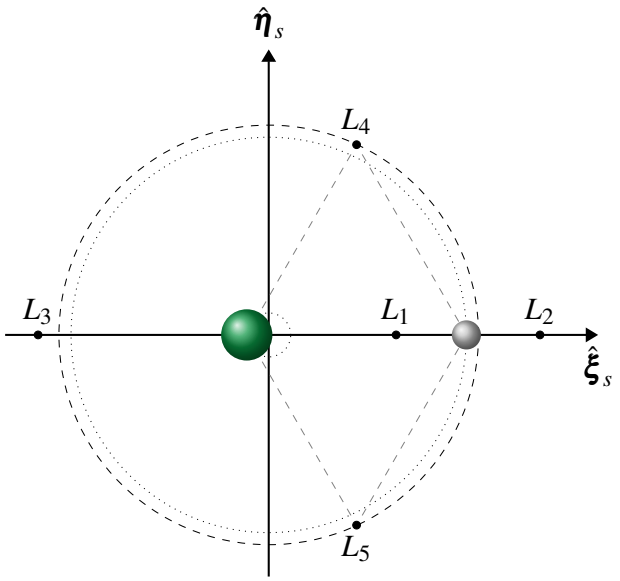

Fig. 2.5 Lagrangian Points in a generic synodic RF.

Within the framework of the CR3BP analytical solutions indeed exist. Although today the complete set of ODEs (2.35) still requires a numerical approach, in 1772 Lagrange revealed the presence of equilibrium points, then named Lagrangian Points (LPs) in tribute to his work [50]. Therefore, retracing Lagrange's steps provides useful theoretical insights into the 3BP dynamics.

First of all, the gradient vector of the pseudopotential is set equal to zero:

$$\nabla \mathscr{U} = 0, \tag{2.39}$$

which means imposing zero velocities and accelerations in the synodic RF.

By expliciting (2.39) in the scalar form, a specific set of coordinates $\{\xi_i, \eta_i, \zeta_i\}$, with $i = 1, ..., 5$, can be retrieved per each of the five LPs:

$$\frac{\partial \mathscr{U}}{\partial \xi} = 0 = \xi - \frac{1-\mu}{\rho_{13}^3}(\xi + \mu) - \frac{\mu}{\rho_{23}^3}[\xi - (1-\mu)] \tag{2.40a}$$

$$\frac{\partial \mathscr{U}}{\partial \eta} = 0 = \eta - \frac{1-\mu}{\rho_{13}^3}\eta - \frac{\mu}{\rho_{23}^3}\eta \tag{2.40b}$$

$$\frac{\partial \mathscr{U}}{\partial \zeta} = 0 = -\frac{1-\mu}{\rho_{13}^3}\zeta - \frac{\mu}{\rho_{23}^3}\zeta. \tag{2.40c}$$

The last equation (2.40c) is immediately satisfied by imposing $\zeta = 0$, implying that all of these equilibrium solutions lie in the $\hat{\boldsymbol{\xi}}_S - \hat{\boldsymbol{\eta}}_S$ plane. Then, the two remaining equations (2.40a) and (2.40b) are solved via substitution. Setting also $\eta = 0$ yields a quintic equation, function of the sole ξ, which has to be solved numerically. The first three equilibrium solutions are known as *collinear* libration points, as they exist along the $\hat{\boldsymbol{\xi}}_S$ axis. They are considered unstable points since a small perturbation from the equilibrium state causes an object placed there drift further away from the LP itself. The other two roots can be found by imposing the primaries distances with respect to the SC, ρ_{13} and ρ_{23}, equal to unity, thus obtaining the *triangular* libration points at the vertices. They are assumed stable as long as the primary-to-secondary mass ratio is greater than 24.96; when an object placed at L4 or L5 accelerates away, the Coriolis force intervenes to correct its trajectory.

Figure 2.5 shows, in a generic binary system, the position of LPs, where the main bodies' gravitational forces perfectly balance. This framework also applies to the Earth-Moon system, on which this thesis focuses. The collinear point L1 lies on the

$\hat{\boldsymbol{\xi}}_S$ axis between the two primaries and is called *cislunar* point; L2 is the *translunar* point, located beyond the Moon, while the *trans-Earth* point L3 is situated on the other side symmetrically with respect to the Moon; L4 and L5 are equidistant from the primaries at the vertices of the two equilateral triangles. When observed from an inertial RF, the entire system revolves around the barycenter, which resides inside the Earth, about 4800 km from its center of mass [47].

Some approximations for the quintic equation can be deduced via the perturbation theory [51]. The complete form for the numerical computation of LPs is:

$$\xi^5 \mp (3-\mu)\xi^4 + (3-2\mu)\xi^3 - \mu\xi^2 \pm 2\mu\xi - \mu = 0. \tag{2.41}$$

Assuming that the smaller between the two main bodies is orders of magnitude smaller than the bigger body, as for the EM system, the first two LPs are equidistant to the smaller primary; they are situated close to the Hill's sphere radius, approximately at the distance:

$$x_{L_i} \approx \mp r_{12}\sqrt{\frac{\mu_2}{3\mu_1}} \quad i = 1,2. \tag{2.42}$$

2.2.5 Zero-velocity surfaces

The previous formulation on the Jacobi integral leads to the concept of Zero-Velocity Surfaces (ZVSs), Hill's solutions for the CR3BP [52]. On these surfaces, given that the relative velocity is null in the synodic frame, the third body has zero kinetic energy ($\mathcal{V} = 0$). It implies that the total energy is entirely potential, thus limiting the SC allowed regions, where it has sufficient energy to reach them without additional propulsion. Therefore, for a given $\mathscr{J}_C$ value, the ZVSs act as a constraint on motion, providing the SC's boundaries equation:

$$\mathscr{J}_C = 2\mathscr{U} = 2\left(\frac{1-\mu}{\rho_1 3} + \frac{\mu}{\rho_2 3}\right)\left(\xi^2 + \eta^2\right). \tag{2.43}$$

By inverting signs in equation (2.38), the representation of these surfaces come closer to the expected understanding of potential energy, as illustrated in Figure 2.6.

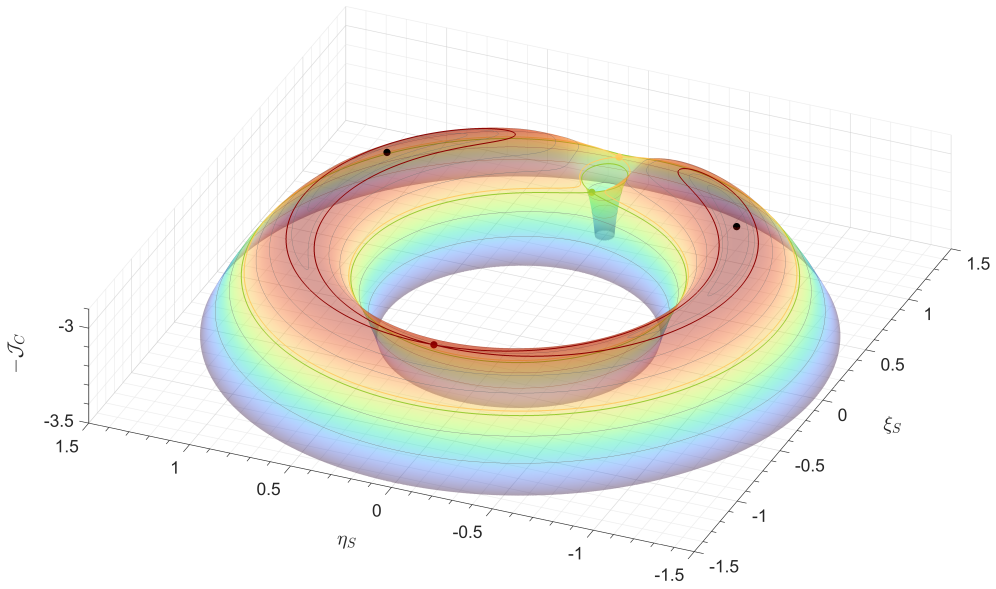

Fig. 2.6 Three-dimensional Earth-Moon ZVSs at LPs energy.

When a spacecraft in proximity to a main body travels at an initial velocity close to the orbital one, its apogee-like condition, namely the maximum apogee it could reach if all the orbit's energy is converted in altitude, will be confined in the gravitational field taking shape around the primaries. In the three-dimensional Earth-Moon system such area, delimited by the mentioned ZVSs is almost toroidal.

As the initial total energy increases, the Jacobi Constant $\mathscr{J}_C$ assumes lower positive values, so that the SC expands its accessible regions. The first surfaces intersecting point is reached at L1, as in Figure 2.6, followed closely behind by the L2 point. Theoretically, a SC able to cross the translunar boundary has enough energy to escape from the EM binary system. By further increasing its energy, the SC can access the L3 energy level, thereby widening the corridor until escape in that direction becomes possible. If a SC can arrive at L4 or L5, no regions of motion within the entire system are forbidden. These LPs are named accordingly to the order in which they become accessible, which in turn corresponds to the decreasing order of their Jacobi Constant values.

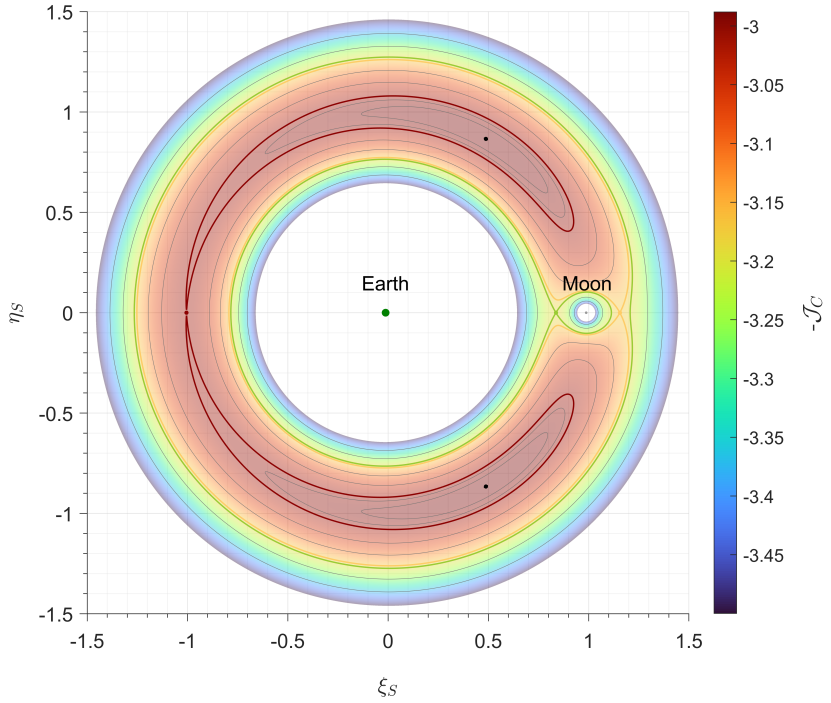

Fig. 2.7 Earth-Moon ZVSs at LPs energy on the $\hat{\boldsymbol{\xi}}_S - \hat{\boldsymbol{\eta}}_S$ plane.

The same concepts are shown in Figure 2.7, projecting the EM system on the $\hat{\boldsymbol{\xi}}_S - \hat{\boldsymbol{\eta}}_S$ plane. The green curve delimits areas characterized by $\mathcal{J}_C < \mathcal{J}_{C,L1}$; inside the yellow curve $\mathcal{J}_{C,L2} < \mathcal{J}_C < \mathcal{J}_{C,L1}$, while up to the red one $\mathcal{J}_{C,L3} < \mathcal{J}_C < \mathcal{J}_{C,L2}$; finally, regions circumscribed by the L3 curve have $\mathcal{J}_{C,L4} = \mathcal{J}_{C,L5} < \mathcal{J}_C < \mathcal{J}_{C,L3}$. This relation between accessibility and $\mathcal{J}_C$ values can be easily observed in Table 2.2, where the LPs coordinates and the corresponding Jacobi Constants are provided.

Table 2.2 EM Lagrangian Points positions and Jacobi Constants in the synodic RF.

	LPs	ξ	η	ζ	$\mathcal{J}_C$
●	L1	0.83740242	0.00000000	0.00000000	3.188326
●	L2	1.15618808	0.00000000	0.00000000	3.172147
●	L3	-1.00506193	0.00000000	0.00000000	3.012145
●	L4	0.48785136	0.86602540	0.00000000	2.987999
●	L5	0.48785136	-0.86602540	0.00000000	2.987999

2.3 N-Body Problem

For the purposes proposed in this thesis, the use of the CR3BP model is sufficient. However, for a better understanding of the fidelity level of the adopted scenario, the NBP is briefly discussed in this Section.

The NBP model considers a multiple-body gravitation, where each body dynamically influences and is influenced by the others. Furthermore, planetary ephemerides are employed, quantifying the evolution of positions and velocities over time under all the existing perturbations and phenomena. Therefore, a realistic scenario, closer to the real solar system, is composed.

The simplest model implies the presence of four bodies (n=4), namely the Sun, Earth, Moon, and the SC itself. Differently from the 3BP, an inertial RS is preferred here for its effectiveness in formulating EoMs; all the trajectories are computed in the EME2000 RS, as depicted in Figure 2.8. Actually, JPL ephemerides[1] are generally set within the International Celestial Reference Frame (ICRF) and comprise libration and nutation effects, which characterize the EME2000 as quasi-inertial. Nonetheless, the rotational offset between the ICRF and the EME2000 is negligible, allowing the EME2000 to be definetively considered inertial.

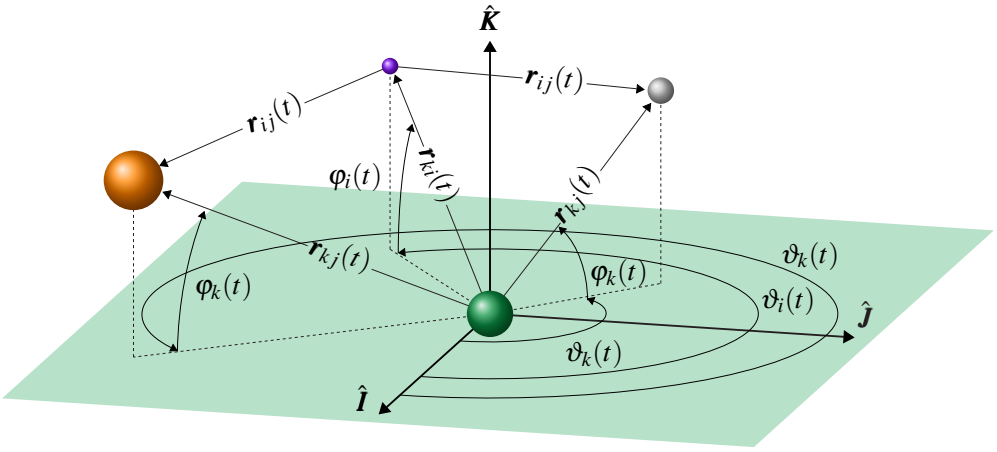

Fig. 2.8 EME2000 RF in the 4BP.

[1]They are regularly computed by the JPL's Navigation and Ancillary Information Facility (NAIF), which provides tools and data for planning mission trajectories and performing scientific analyses.

From the NSL, a SC in this RF experiences an acceleration of:

$$\ddot{\boldsymbol{r}}_i = -\sum_{\substack{j=1 \\ j\neq i}}^{n} \frac{\mu_j}{r_{ji}^3} \boldsymbol{r}_{ji}, \tag{2.44}$$

where the Earth is denoted as the k-th body, with additional body labeled as the j-th entity, excluding the spacecraft which is marked as i.

Reformulating the equation with respect to the central body (i.e. the Earth) provides the following second-order ODE:

$$\ddot{\boldsymbol{r}}_{ki} = -\frac{(\mu_i + \mu_k)}{r_{ki}^3} \boldsymbol{r}_{ki} + \sum_{\substack{j=1 \\ j\neq i,k}}^{n} \mu_j \left(\frac{\boldsymbol{r}_{ij}}{r_{ij}^3} - \frac{\boldsymbol{r}_{kj}}{r_{kj}^3} \right). \tag{2.45}$$

Beyond the influence of the Moon and Sun's gravitation, other two pertubative effects are conventionally included:

- The Earth's asphericity, as this non-uniform distribution of mass creates variations in the Earth's gravitational field.
- The solar radiation pressure, exterted by photons emitted by the Sun when they hit a surface at the speed of light.

By summing these contributions, the overall perturbation that affects the system dynamics can be written in form of perturbing acceleration:

$$\mathbf{a}_p = \mathbf{a}_{SM} + \mathbf{a}_{asph} + \mathbf{a}_{SRP}. \tag{2.46}$$

Some considerations on how this model would influence the concept of the implemented orbits will be provided in Section 3.5.

Chapter 3

Periodic Orbits generation in the CR3BP

This Chapter delves into the numerical processes that allow the construction and validation of POs in the Circular Restricted Three-Body Problem (CR3BP). Although it may seem more convenient to analyze orbits in a n-body model, calculating them within a lower-fidelity CR3BP provides a valuable starting point for the optimization problem, which represents the real core of this thesis.

Underlying the procedure is the concept of differential correction; once an initial estimate of the periodic solution is made, it is iterated and corrected until a solution satisfying the desired conditions is reached. Through the use of a sensitivity matrix, named State Transition Matrix (STM), a linear mapping between the initial and final conditions is performed to better guide the solution updating. Specifically, a single-shooting procedure based on such correction scheme is implemented, thus yielding exact periodic motions for specific orbits in the CR3BP domain.

Starting from analytical approximations, two main families of POs are computed: Lyapunov Orbits (LOs), lying on the same plane of the two primary bodies, and Distant Retrograde Orbits (DROs), which are again planar, but deviate from the first ones by increasing dimensions. Further considerations about the role of ephemerides and the transition to Quasi-Periodic Orbits (QPOs) in the higher-fidelity NBP are finally provided.

3.1 Orbits analytical approximation

The current section introduces the construction of orbits -and more in general of trajectories- within the CR3BP domain, serving as a foundation and precursor for the optimization procedure. Specifically, the generation process starts from the orbits analytical approximation, leading to the numerical computation of POs via Differential Correction (DC) and single-shooting methods.

Since the CR3BP is a time-invariant model, its set of epoch-independent, autonomous EoMs can be linearized in order to investigate the SC behavior nearby LPs. By applying a Taylor series expansion to the RHS of equation (2.35), and denoting the second partial derivatives of $\mathscr{U}$ as:

$$\frac{\partial^2 \mathscr{U}}{\partial \xi \partial \eta} \triangleq \mathscr{U}_{\xi\eta}, \tag{3.1}$$

one obtains the following *variational equations*:

$$\ddot{\xi} - 2\dot{\eta} = \mathscr{U}_{\xi\xi}\big|_{LP}\xi + \mathscr{U}_{\xi\eta}\big|_{LP}\eta + \mathscr{U}_{\xi\zeta}\big|_{LP}\zeta \tag{3.2a}$$

$$\ddot{\eta} + 2\dot{\xi} = \mathscr{U}_{\eta\xi}\big|_{LP}\xi + \mathscr{U}_{\eta\eta}\big|_{LP}\eta + \mathscr{U}_{\eta\zeta}\big|_{LP}\zeta \tag{3.2b}$$

$$\ddot{\zeta} = \mathscr{U}_{\zeta\xi}\big|_{LP}\xi + \mathscr{U}_{\zeta\eta}\big|_{LP}\eta + \mathscr{U}_{\zeta\zeta}\big|_{LP}\zeta, \tag{3.2c}$$

with the subscript *LP* referring to the partial derivatives computed at the equilibrium points. This notation is omitted here for clarity. Since all the equilibrium points lie on the $\hat{\boldsymbol{\xi}}_S - \hat{\boldsymbol{\eta}}_S$ plane, the mixed partial derivatives containing ζ are null by definition, namely $\mathscr{U}_{\xi\zeta} = \mathscr{U}_{\eta\zeta} = 0$. As a result, the out-of-plane motion ζ, induced by the acceleration $\ddot{\zeta}$, exhibits a linear behavior, whose effects on the in-plane motion in the ξ and η directions are negligible. Indeed, the last line in system (3.2), $\ddot{\zeta} = \mathscr{U}_{\zeta\zeta}\zeta$, is decoupled from the other two, and proves to be an harmonic in the $\hat{\boldsymbol{\zeta}}_S$ direction:

$$\zeta = A_\zeta \cos(\omega_\zeta \tau) + B_\zeta \sin(\omega_\zeta \tau), \tag{3.3}$$

where A_ζ and B_ζ are constants depending on the initial conditions. The out-of-plane frequency can be computed as:

$$\omega_\zeta^2 = -\mathscr{U}_{\zeta\zeta}. \tag{3.4}$$

The first two equations (3.2a) and (3.2b) form a coupled system of two second-order ODEs that can be reformulated into a set of four first-order ODEs:

$$\begin{Bmatrix} \dot{\xi} \\ \dot{\eta} \\ \ddot{\xi} \\ \ddot{\eta} \end{Bmatrix} = \begin{bmatrix} 0 & 0 & 1 & 0 \\ 0 & 0 & 0 & 1 \\ \mathscr{U}_{\xi\xi} & \mathscr{U}_{\xi\eta} & 0 & 2 \\ \mathscr{U}_{\eta\xi} & \mathscr{U}_{\eta\eta} & -2 & 0 \end{bmatrix} \begin{Bmatrix} \xi \\ \eta \\ \dot{\xi} \\ \dot{\eta} \end{Bmatrix}, \tag{3.5}$$

or, in compact form:

$$\dot{\tilde{\boldsymbol{X}}} = \tilde{\boldsymbol{A}}\tilde{\boldsymbol{X}}, \tag{3.6}$$

where $\tilde{\boldsymbol{A}}$ is the nondimensional Jacobian matrix and $\tilde{\boldsymbol{X}}$ represents here the (planar reduced) nondimensional state of the SC. Looking at the determinant, a quartic equation arises:

$$\lambda^4 + \left(4 - \mathscr{U}_{\xi\xi} - \mathscr{U}_{\eta\eta}\right)\lambda^2 + \left(\mathscr{U}_{\xi\xi}\mathscr{U}_{\eta\eta} - \mathscr{U}_{\xi\eta}^2\right) = 0, \tag{3.7}$$

thus yielding four different roots. By implementing the procedure presented in Szebehely [49], it is proven that at the three collinear points, for $0 < \mu < 1/2$, the following holds:

$$\mathscr{U}_{\xi\xi} > 0, \quad \mathscr{U}_{\eta\eta} < 0, \quad \mathscr{U}_{\xi\eta} = 0. \tag{3.8}$$

Hence, the equation (3.7) can be rewritten to find the two roots $\Lambda_{1/2}$ as:

$$\Lambda^2 + 2\beta_1\lambda - \lambda\beta_2^2 = 0, \tag{3.9}$$

where:

$$\left.\begin{aligned} \Lambda &= \lambda^2 \\ \beta_1 &= 2 - \frac{\mathscr{U}_{\xi\xi} + \mathscr{U}_{\eta\eta}}{2} \\ \beta_2 &= \sqrt{-\mathscr{U}_{\xi\xi}\mathscr{U}_{\eta\eta}} \end{aligned}\right\} \quad \Rightarrow \quad \Lambda_{1/2} = -\beta_1 \pm \sqrt{\beta_1^2 + \beta_2^2}. \tag{3.10}$$

The four eigenvalues are:

$$\lambda_{1/2} = \pm\sqrt{\Lambda_1}, \tag{3.11a}$$

$$\lambda_{3/4} = \pm\sqrt{\Lambda_2}. \tag{3.11b}$$

The first two eigenvalues in equation (3.11a) are real ones, whereas the other two in equation (3.11b) are pure imaginary. The third eigenvalue, namely the first imaginary solution, provides the in-plane frequency of the linearized PO:

$$\omega_3 = -i\lambda_3. \tag{3.12}$$

The solutions for ξ and η as a function of the nondimensional time τ are coupled and exhibit both aperiodic exponential growths and decays, which may affect the stability of trajectory around the collinear points. The first-order approximation sought for the following analysis is a purely aperiodic structure. After further mathematical manipulations and by nullifying any aperiodic exponential instability, a simplified set of EoMs is obtained [53]:

$$\begin{cases} \xi(\tau) = A_\xi \cos(\omega_3 \tau + \phi) & \text{(3.13a)} \\ \eta(\tau) = -c_2 A_\xi \sin(\omega_3 \tau + \phi) & \text{(3.13b)} \\ \zeta(\tau) = A_\zeta \cos(\omega_\zeta \tau + \psi) & \text{(3.13c)} \\ \dot{\xi}(\tau) = -A_\xi \omega_3 \sin(\omega_3 \tau + \phi) & \text{(3.13d)} \\ \dot{\eta}(\tau) = -c_2 A_\xi \omega_3 \cos(\omega_3 \tau + \phi) & \text{(3.13e)} \\ \dot{\zeta}(\tau) = -A_\zeta \omega_\zeta \sin(\omega_\zeta \tau + \psi) & \text{(3.13f)} \end{cases}$$

where A_ξ and A_ζ are respectively the initial amplitudes in the $\hat{\boldsymbol{\xi}}_S$ and $\hat{\boldsymbol{\zeta}}_S$ directions. Specifically, the quantity A_ξ resembles the semimajor axis of a generic orbit, whereas the semiminor axis A_η can be computed as:

$$A_\eta = c_2 A_\xi. \tag{3.14}$$

The trajectories resulting from the system (3.13) can be used as initial analytical solutions for the differential correction procedure. Indeed, where an analytical propagation yields an indefinitely stable elliptical orbit, using the initial state vector $\tilde{\boldsymbol{X}}^a(\tau_0) = \left\{\xi_0, \eta_0, \zeta_0, \dot{\xi}_0, \dot{\eta}_0, \dot{\zeta}_0\right\}^T$ as a starting condition for the NL integration of the CR3BP EoMs, a divergent, non-linear behavior emerges. The probability of remaining stable for longer in the integrated orbit increases as the dimensions of the initial analytical one are smaller. To effectively predict the evolution and stability of

POs in the CR3BP, the momentum integral is introduced:

$$\mathcal{M}_I = \int_{\tau_0}^{\tau_f} \left[\xi(\tau)\dot{\xi}(\tau) + \eta(\tau)\dot{\eta}(\tau) + \zeta(\tau)\dot{\zeta}(\tau) \right] d\tau. \tag{3.15}$$

Such a line integral is computed over the SC integrated state from τ_0 to τ_f and allows to predict with a sufficient margin when nonlinearities are inducing an undesired escape. Specifically, the momentum integral is typically observed to exhibit a negative trend over time; when $\mathcal{M}_I > 0$ at a specific point, it serves as a warning sign of potential escape: the integrated orbit deviates significantly and the solution diverges from the desired closed trajectory.

3.2 Differential Correction

In this thesis, the study of POs' stability is not strictly necessary, as long as the baseline departure trajectory remains for a reasonable time in its initial configuration. In particular, a simple single-shooting method is employed to fulfill the requirement of preserving the orbit stability for at least a single complete period. Additionally, this method improves the initial guesses resulting from the analytical approach, as seen in section 3.1. Two types of periodic orbits are considered: planar Lyapunov Orbits (LOs) and Distant Retrograde Orbits (DRO)s.

In order to find a specified path from an initial state $\tilde{\boldsymbol{X}}(\tau_0)$ to a desired final state $\tilde{\boldsymbol{X}}(\tau_f)$, or from $\boldsymbol{X}(t_0)$ to $\boldsymbol{X}(t_f)$ in dimensional quantities, a classic Two-Point Boundary Value Problem (TPBVP) is implemented. The procedure implies that a reasonable initial guess is selected for the initial state and integrated for a specified duration, changing the initial quantities iteratively, until an integrated final state converges to the desired condition. The key concept is to understand *how* the initial state should be corrected to produce the final one, namely to analyze how $\tilde{\boldsymbol{X}}(\tau_0)$ and $\tilde{\boldsymbol{X}}(\tau_f)$ are related along the trajectory. This method proves to be extremely robust and provides theoretical insights about the evolution of states over time and the correction of the baseline trajectory under specific boundary conditions.

The *variation* between the desired $\boldsymbol{X}^*(\tau_f)$ and the actual final state $\boldsymbol{X}(\tau_f)$ can be expressed as:

$$\delta\tilde{\boldsymbol{X}}(\tau_f) = \tilde{\boldsymbol{X}}\left(\tilde{\boldsymbol{X}}(\tau_0), \tau_f\right) - \tilde{\boldsymbol{X}}^*\left(\tilde{\boldsymbol{X}}^*(\tau_0), \tau_f\right), \tag{3.16}$$

where the DC procedure aims at nullifying such discrepancy. For this purpose, a specific correction in the initial state, say $\delta\tilde{\boldsymbol{X}}(\tau_0)$ produces the following desired initial state:

$$\tilde{\boldsymbol{X}}^*(\tau_0) = \tilde{\boldsymbol{X}}(\tau_0) + \delta\tilde{\boldsymbol{X}}(\tau_0). \tag{3.17}$$

By expanding and linearizing the equation (3.16), one has:

$$\begin{aligned}
\delta\tilde{\boldsymbol{X}}(\tau_f) &= \tilde{\boldsymbol{X}}\left(\tilde{\boldsymbol{X}}(\tau_0), \tau_f\right) - \tilde{\boldsymbol{X}}^*\left(\tilde{\boldsymbol{X}}^*(\tau_0), \tau_f\right) \\
&= \tilde{\boldsymbol{X}}\left(\tilde{\boldsymbol{X}}(\tau_0) + \delta\tilde{\boldsymbol{X}}(\tau_0)\right) - \tilde{\boldsymbol{X}}^*\left(\tilde{\boldsymbol{X}}^*(\tau_0), \tau_f\right) \\
&= \frac{\partial\tilde{\boldsymbol{X}}(\tau_f)}{\partial\tilde{\boldsymbol{X}}(\tau_0)}\delta\tilde{\boldsymbol{X}}(\tau_0), \\
\delta\tilde{\boldsymbol{X}}(\tau_f) &= \tilde{\boldsymbol{\Phi}}(\tau_f, \tau_0)\delta\tilde{\boldsymbol{X}}(\tau_0).
\end{aligned} \tag{3.18}$$

where the first term in the RHS of equation (3.18) is the State Transition Matrix (STM), $\tilde{\boldsymbol{\Phi}}(\tau_f, \tau_0)$, in its nondimensional form in the CR3BP domain. As per equation (3.6), the STM, often denoted as sensitivity matrix, allows to quantify how much variations in the final state are *sensible* to changes in the initial state. Such *linear mapping* can be indeed performed through the partial derivatives of all state quantities computed at a specified final time τ_f with respect to all the same quantities at the initial time τ_0. Therefore:

$$\tilde{\boldsymbol{\Phi}}(\tau, \tau_0) = \begin{bmatrix}
\frac{\partial\xi}{\partial\xi_0} & \frac{\partial\xi}{\partial\eta_0} & \frac{\partial\xi}{\partial\zeta_0} & \frac{\partial\xi}{\partial\dot{\xi}_0} & \frac{\partial\xi}{\partial\dot{\eta}_0} & \frac{\partial\xi}{\partial\dot{\zeta}_0} \\
\frac{\partial\eta}{\partial\xi_0} & \frac{\partial\eta}{\partial\eta_0} & \frac{\partial\eta}{\partial\zeta_0} & \frac{\partial\eta}{\partial\dot{\xi}_0} & \frac{\partial\eta}{\partial\dot{\eta}_0} & \frac{\partial\eta}{\partial\dot{\zeta}_0} \\
\frac{\partial\zeta}{\partial\xi_0} & \frac{\partial\zeta}{\partial\eta_0} & \frac{\partial\zeta}{\partial\zeta_0} & \frac{\partial\zeta}{\partial\dot{\xi}_0} & \frac{\partial\zeta}{\partial\dot{\eta}_0} & \frac{\partial\zeta}{\partial\dot{\zeta}_0} \\
\frac{\partial\dot{\xi}}{\partial\xi_0} & \frac{\partial\dot{\xi}}{\partial\eta_0} & \frac{\partial\dot{\xi}}{\partial\zeta_0} & \frac{\partial\dot{\xi}}{\partial\dot{\xi}_0} & \frac{\partial\dot{\xi}}{\partial\dot{\eta}_0} & \frac{\partial\dot{\xi}}{\partial\dot{\zeta}_0} \\
\frac{\partial\dot{\eta}}{\partial\xi_0} & \frac{\partial\dot{\eta}}{\partial\eta_0} & \frac{\partial\dot{\eta}}{\partial\zeta_0} & \frac{\partial\dot{\eta}}{\partial\dot{\xi}_0} & \frac{\partial\dot{\eta}}{\partial\dot{\eta}_0} & \frac{\partial\dot{\eta}}{\partial\dot{\zeta}_0} \\
\frac{\partial\dot{\zeta}}{\partial\xi_0} & \frac{\partial\dot{\zeta}}{\partial\eta_0} & \frac{\partial\dot{\zeta}}{\partial\zeta_0} & \frac{\partial\dot{\zeta}}{\partial\dot{\xi}_0} & \frac{\partial\dot{\zeta}}{\partial\dot{\eta}_0} & \frac{\partial\dot{\zeta}}{\partial\dot{\zeta}_0}
\end{bmatrix} = \left[\begin{array}{c|c} \tilde{\boldsymbol{\Phi}}_{\rho\rho} & \tilde{\boldsymbol{\Phi}}_{\rho\mathcal{V}} \\ \hline \tilde{\boldsymbol{\Phi}}_{\mathcal{V}\rho} & \tilde{\boldsymbol{\Phi}}_{\mathcal{V}\mathcal{V}} \end{array}\right], \tag{3.19}$$

where the STM is a $\tilde{\boldsymbol{\Phi}} \in \mathbb{R}^{6\times6}$ matrix composed by four square submatrices 3×3 of partial derivatives; the first subscript denotes the numerator, the second one the denominator, with the vectors $\boldsymbol{\rho}$ and $\boldsymbol{\mathcal{V}}$ respectively indicating nondimensional position and velocities. For the sake of brevity, a simpler notation is introduced:

$$\tilde{\boldsymbol{X}}_f \triangleq \tilde{\boldsymbol{X}}\left(\tilde{\boldsymbol{X}}(\tau_0), \tau_f\right), \tag{3.20a}$$

$$\tilde{\boldsymbol{X}}_0 \triangleq \tilde{\boldsymbol{X}}(\tau_0). \tag{3.20b}$$

Given its strong connection with state variations over time, the STM evolves over the trajectory in the same manner as the trajectory itself. So, for a generic time τ:

$$\begin{aligned}
\dot{\tilde{\boldsymbol{\Phi}}}(\tau,\tau_0) &= \frac{\mathrm{d}}{\mathrm{d}\tau}\tilde{\boldsymbol{\Phi}}(\tau,\tau_0) = \frac{\mathrm{d}}{\mathrm{d}\tau}\left(\frac{\partial\tilde{\boldsymbol{X}}}{\partial\tilde{\boldsymbol{X}}_0}\right) \\
&= \frac{\partial}{\partial\tilde{\boldsymbol{X}}_0}\left(\frac{\mathrm{d}\tilde{\boldsymbol{X}}}{\mathrm{d}\tau}\right) \\
&= \frac{\partial\dot{\tilde{\boldsymbol{X}}}}{\partial\tilde{\boldsymbol{X}}}\frac{\partial\tilde{\boldsymbol{X}}}{\partial\tilde{\boldsymbol{X}}_0}, \\
\dot{\tilde{\boldsymbol{\Phi}}}(\tau,\tau_0) &= \tilde{\boldsymbol{A}}(\tau)\tilde{\boldsymbol{\Phi}}(\tau,\tau_0).
\end{aligned} \tag{3.21}$$

Therefore, the evolution of the STM is described by its own set of 36 governing ODEs via the Jacobian matrix $\tilde{\boldsymbol{A}}(\tau)$. Such matrix, also a function of the state of the reference trajectory, plays exactly the same role of the Jacobian one in equation (3.6). Moreover, similarly to the STM, $\tilde{\boldsymbol{A}} \in \mathbb{R}^{6\times6}$ is composed by four square 3×3 submatrices:

$$\tilde{\boldsymbol{A}}(\tau) = \left[\begin{array}{c|c} \boldsymbol{0} & \boldsymbol{I} \\ \hline \boldsymbol{U} & \boldsymbol{\Omega} \end{array}\right], \tag{3.22}$$

or, in explicit form:

$$\tilde{\boldsymbol{A}}(\tau) = \begin{bmatrix} 0 & 0 & 0 & 1 & 0 & 0 \\ 0 & 0 & 0 & 0 & 1 & 0 \\ 0 & 0 & 0 & 0 & 0 & 1 \\ \mathcal{U}_{\xi\xi} & \mathcal{U}_{\xi\eta} & \mathcal{U}_{\xi\zeta} & 0 & 2 & 0 \\ \mathcal{U}_{\eta\xi} & \mathcal{U}_{\eta\eta} & \mathcal{U}_{\eta\zeta} & -2 & 0 & 0 \\ \mathcal{U}_{\zeta\xi} & \mathcal{U}_{\zeta\eta} & \mathcal{U}_{\zeta\zeta} & 0 & 0 & 0 \end{bmatrix}. \tag{3.23}$$

To verify the elements of $\tilde{\boldsymbol{A}}(\tau)$, one can simply double-check the set of equations (3.2). The explicit form of the second partial derivatives of the pseudopotential $\mathscr{U}$ is omitted here for brevity, but is provided in Appendix A.

3.3 Single-shooting procedure

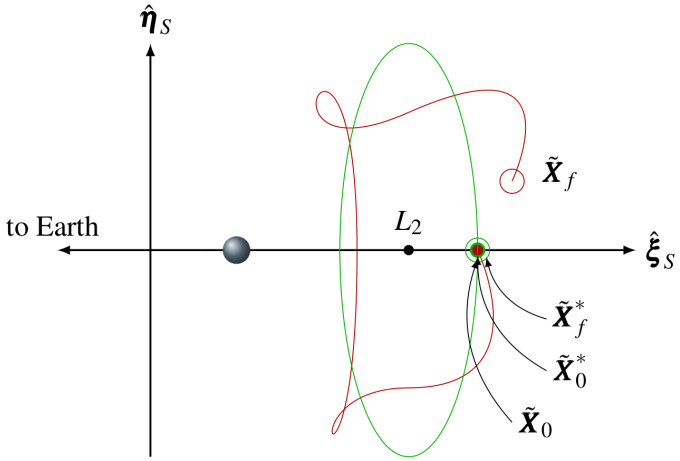

Fig. 3.1 Single-shooting procedure for a generic Lyapunov orbit in the CR3BP domain [44].

As anticipated, the *shooting* method essentially consists in adjusting some initial conditions until a targeted set of specified final conditions is respected, in the form of a TPBVP. This procedure requires possibly computing corrections from undesired terminal deviations, in order to refine the initial state iteratively until convergence.

Figure 3.1 shows, for example, the single-shooting method applied to generic planar Lyapunov orbit in the EM binary system. The green orbit is the targeted final trajectory, precisely the Lyapunov orbit; such solution is defined by an initial state $\tilde{\boldsymbol{X}}_0^*$ which produces, after a complete revolution, the final state $\tilde{\boldsymbol{X}}_f^*$. The red trajectory, instead, is a non-converged tentative solution to obtain the same Lyapunov orbit.

While its departure guess $\tilde{\boldsymbol{X}}_0$ has been imposed to coincide with the desired initial point, the integrated final state $\tilde{\boldsymbol{X}}_f$ does not achieve the targeted one. Indeed, in shooting methods, some initial quantities may be fixed to specified values, and not all the final conditions are constrained to the targeted ones, but some of them may be allowed to acquire any feasible values. In the example, since the initial positions

are fixed, the discrepancy between the desired $\tilde{\boldsymbol{X}}_f^*$ and the actual $\tilde{\boldsymbol{X}}_f$ can be imputed to the initial guesses for the sole velocities. Therefore, only these values should be allowed to vary during correction.

In general, the free-variable vector $\tilde{\boldsymbol{X}}_0 \in \mathbb{R}^{n\times 1}$ has the form:

$$\tilde{\boldsymbol{X}}_0 = \{X_1,\, X_2,\, \ldots,\, X_n\}^T, \tag{3.24}$$

and may contain all state elements, such as positions, velocities and integration times.

The constraint vector, on the other hand, targets the desired final quantities, which, in this analysis, correspond to all those relevant in generating POs in the CR3BP. So, the constraint vector $\boldsymbol{\chi}(\tilde{\boldsymbol{X}}_0) \in \mathbb{R}^{m\times 1}$, deriving from $\tilde{\boldsymbol{X}}_0$, accounts the differences between actual and desired final states, including final positions and velocities:

$$\boldsymbol{\chi}(\tilde{\boldsymbol{X}}_0) = \{\chi_1,\, \chi_2,\, \ldots,\, \chi_m\}^T = \begin{Bmatrix} \xi - \xi^* \\ \eta - \eta^* \\ \zeta - \zeta^* \\ \dot{\xi} - \dot{\xi}^* \\ \dot{\eta} - \dot{\eta}^* \\ \dot{\zeta} - \dot{\zeta}^* \end{Bmatrix}. \tag{3.25}$$

The correction method now can be translate into searching for a specified initial state $\tilde{\boldsymbol{X}}_0^*$ that satisfy all constraints, so that:

$$\boldsymbol{\chi}(\tilde{\boldsymbol{X}}_0^*) = \boldsymbol{0}. \tag{3.26}$$

In order to quantify how a variation in the free-variable vector affects the constraint vector, a first-order Taylor expansion is performed. For a generic new variable state vector $\tilde{\boldsymbol{X}}$, the constraint vector can be defined as:

$$\boldsymbol{\chi}(\tilde{\boldsymbol{X}}) = \tilde{\boldsymbol{\chi}}(\tilde{\boldsymbol{X}}_0) + \frac{\partial \tilde{\boldsymbol{\chi}}(\tilde{\boldsymbol{X}}_0)}{\partial \tilde{\boldsymbol{X}}}(\tilde{\boldsymbol{X}} - \tilde{\boldsymbol{X}}_0). \tag{3.27}$$

Here, the partial derivatives of the constraints with respect to the forward-in-time free-variable quantities form again a Jacobian matrix $\tilde{\boldsymbol{J}}(\tilde{\boldsymbol{\chi}}(\tilde{\boldsymbol{X}}_0),\tilde{\boldsymbol{X}}) \in \mathbb{R}^{m\times n}$:

$$\frac{\partial \boldsymbol{\chi}(\tilde{\boldsymbol{X}}_0)}{\partial \tilde{\boldsymbol{X}}} = \tilde{\boldsymbol{J}}(\boldsymbol{\chi}(\tilde{\boldsymbol{X}}_0),\tilde{\boldsymbol{X}}) = \begin{bmatrix} \frac{\partial \chi_1}{\partial \tilde{X}_1} & \frac{\partial \chi_1}{\partial \tilde{X}_2} & \cdots & \frac{\partial \chi_1}{\partial \tilde{X}_n} \\ \frac{\partial \chi_2}{\partial \tilde{X}_1} & \frac{\partial \chi_2}{\partial \tilde{X}_2} & \cdots & \frac{\partial \chi_2}{\partial \tilde{X}_n} \\ \vdots & \vdots & \ddots & \vdots \\ \frac{\partial \chi_m}{\partial \tilde{X}_1} & \frac{\partial \chi_m}{\partial \tilde{X}_2} & \cdots & \frac{\partial \chi_m}{\partial \tilde{X}_n} \end{bmatrix}. \tag{3.28}$$

Such matrix closely resembles the STM in equation (3.19) and allows to understand how the design vector $\tilde{\boldsymbol{X}}_0$ must be updated at each step. Expanding the constraint vector in an iterative form, the subsequent step $r+1$ can be expressed as a function of the previous r-th step:

$$\boldsymbol{\chi}(\tilde{\boldsymbol{X}}_{r+1}) = \boldsymbol{\chi}(\tilde{\boldsymbol{X}}_r) + \frac{\partial \tilde{\boldsymbol{\chi}}(\tilde{\boldsymbol{X}}_r)}{\partial \tilde{\boldsymbol{X}}_{r+1}}(\tilde{\boldsymbol{X}}_{r+1} - \tilde{\boldsymbol{X}}_r). \tag{3.29}$$

To avoid a burdening notation the following shortenings are introduced:

$$\boldsymbol{\chi}_r \triangleq \boldsymbol{\chi}\left(\tilde{\boldsymbol{X}}_r\right), \tag{3.30a}$$

$$\tilde{\boldsymbol{J}}(\boldsymbol{\chi}_r) \triangleq \tilde{\boldsymbol{J}}\left(\boldsymbol{\chi}(\tilde{\boldsymbol{X}}_r),\tilde{\boldsymbol{X}}_{r+1}\right). \tag{3.30b}$$

If a solution exists, then $\boldsymbol{\chi}_{r+1} = \boldsymbol{0}$ and an iterative solution takes the form:

$$\boldsymbol{\chi}_r + \left[\tilde{\boldsymbol{J}}(\boldsymbol{\chi}_r)\right](\tilde{\boldsymbol{X}}_{r+1} - \tilde{\boldsymbol{X}}_r) = \boldsymbol{0}. \tag{3.31}$$

Therefore, one can compute at each iteration the state of the design vector $\tilde{\boldsymbol{X}}_r$ and the updated value of the constraint vector $\boldsymbol{\chi}_r$, derived directly from integrating all EoMs from $\tilde{\boldsymbol{X}}_r$, as per:

$$\tilde{\boldsymbol{X}}_{r+1} = \tilde{\boldsymbol{X}}_r - \left[\tilde{\boldsymbol{J}}(\boldsymbol{\chi}_r)\right]^{-1}\boldsymbol{\chi}_r. \tag{3.32}$$

If there are more state variables than constraints $n > m$, the minimum norm update equation is used in place of equation (3.32):

$$\tilde{\boldsymbol{X}}_{r+1} = \tilde{\boldsymbol{X}}_r - \left[\tilde{\boldsymbol{J}}(\boldsymbol{\chi}_r)\right]^T \left[\tilde{\boldsymbol{J}}(\boldsymbol{\chi}_r)\tilde{\boldsymbol{J}}(\boldsymbol{\chi}_r)^T\right]^{-1} \boldsymbol{\chi}_r, \tag{3.33}$$

guiding the next solution to be not too far to the initial guess $\tilde{\boldsymbol{X}}_r$, among the infinite possible ones. A relaxation parameter κ_R is introduced to aid the convergence, allowing to perform small corrections at each iteration. Typically, for planar LOs a $\kappa_R \approx 0.5$ is sufficient, whereas more complex trajectories has to be computed with smaller coefficients. Formally, an iterative Richardson's correction method arises:

$$\tilde{\boldsymbol{X}}_{r+1} = \tilde{\boldsymbol{X}}_r - \kappa_R \cdot \left[\tilde{\boldsymbol{J}}(\boldsymbol{\chi}_r)\right]^{-1} \boldsymbol{\chi}_r, \qquad \text{if } n = m, \tag{3.34a}$$

$$\tilde{\boldsymbol{X}}_{r+1} = \tilde{\boldsymbol{X}}_r - \kappa_R \cdot \left[\tilde{\boldsymbol{J}}(\boldsymbol{\chi}_r)\right]^T \left[\tilde{\boldsymbol{J}}(\boldsymbol{\chi}_r)\tilde{\boldsymbol{J}}(\boldsymbol{\chi}_r)^T\right]^{-1} \boldsymbol{\chi}_r, \qquad \text{if } n > m. \tag{3.34b}$$

3.3.1 Variable Time vs Fixed Time Differential Correction

In the DC process, the integration time may be variable, and thus included in the design vector, or imposed, giving respectively rise to two different procedures: the Variable-Time Differential Correction (VTDC) and the Fixed-Time Differential Correction (FTDC). In this analysis, the integration time is set to the period of a single, complete revolution about a specific PO. The general form of the design vector $\tilde{\boldsymbol{X}}_0$, including time, is:

$$\tilde{\boldsymbol{X}}_0 = \left\{\xi,\ \eta,\ \zeta,\ \dot{\xi},\ \dot{\eta},\ \dot{\zeta},\ \tau\right\}^T, \tag{3.35}$$

where τ is specifically the nondimensional period of the PO, namely:

$$\tau = \tau_f - \tau_0. \tag{3.36}$$

If the time is constrained, it is sufficient to exclude it from the free-variable vector and specify the period of the PO directly; indeed, the complete constraint vector coincides with the one in equation (3.25). Since there are seven free variables now, coupled with six constraints, the Jacobian is composed by a further column, corresponding to the partial derivatives of the other state variables with respect to the integration time τ, namely velocities and accelerations. Therefore, the complete

Jacobian matrix $\tilde{\boldsymbol{J}} \in \mathbb{R}^{6\times 7}$ attains the form:

$$\tilde{\boldsymbol{J}}(\boldsymbol{\chi}(\tilde{\boldsymbol{X}}_0),\, \tilde{\boldsymbol{X}}_0) = \begin{bmatrix} \frac{\partial \xi_f}{\partial \xi_0} & \frac{\partial \xi_f}{\partial \eta_0} & \frac{\partial \xi_f}{\partial \zeta_0} & \frac{\partial \xi_f}{\partial \dot{\xi}_0} & \frac{\partial \xi_f}{\partial \dot{\eta}_0} & \frac{\partial \xi_f}{\partial \dot{\zeta}_0} & \frac{\partial \xi_f}{\partial \tau} \\ \frac{\partial \eta_f}{\partial \xi_0} & \frac{\partial \eta_f}{\partial \eta_0} & \frac{\partial \eta_f}{\partial \zeta_0} & \frac{\partial \eta_f}{\partial \dot{\xi}_0} & \frac{\partial \eta_f}{\partial \dot{\eta}_0} & \frac{\partial \eta_f}{\partial \dot{\zeta}_0} & \frac{\partial \eta_f}{\partial \tau} \\ \frac{\partial \zeta_f}{\partial \xi_0} & \frac{\partial \zeta_f}{\partial \eta_0} & \frac{\partial \zeta_f}{\partial \zeta_0} & \frac{\partial \zeta_f}{\partial \dot{\xi}_0} & \frac{\partial \zeta_f}{\partial \dot{\eta}_0} & \frac{\partial \zeta_f}{\partial \dot{\zeta}_0} & \frac{\partial \zeta_f}{\partial \tau} \\ \frac{\partial \dot{\xi}_f}{\partial \xi_0} & \frac{\partial \dot{\xi}_f}{\partial \eta_0} & \frac{\partial \dot{\xi}_f}{\partial \zeta_0} & \frac{\partial \dot{\xi}_f}{\partial \dot{\xi}_0} & \frac{\partial \dot{\xi}_f}{\partial \dot{\eta}_0} & \frac{\partial \dot{\xi}_f}{\partial \dot{\zeta}_0} & \frac{\partial \dot{\xi}_f}{\partial \tau} \\ \frac{\partial \dot{\eta}_f}{\partial \xi_0} & \frac{\partial \dot{\eta}_f}{\partial \eta_0} & \frac{\partial \dot{\eta}_f}{\partial \zeta_0} & \frac{\partial \dot{\eta}_f}{\partial \dot{\xi}_0} & \frac{\partial \dot{\eta}_f}{\partial \dot{\eta}_0} & \frac{\partial \dot{\eta}_f}{\partial \dot{\zeta}_0} & \frac{\partial \dot{\eta}_f}{\partial \tau} \\ \frac{\partial \dot{\zeta}_f}{\partial \xi_0} & \frac{\partial \dot{\zeta}_f}{\partial \eta_0} & \frac{\partial \dot{\zeta}_f}{\partial \zeta_0} & \frac{\partial \dot{\zeta}_f}{\partial \dot{\xi}_0} & \frac{\partial \dot{\zeta}_f}{\partial \dot{\eta}_0} & \frac{\partial \dot{\zeta}_f}{\partial \dot{\zeta}_0} & \frac{\partial \dot{\zeta}_f}{\partial \tau} \end{bmatrix}, \tag{3.37}$$

where the first six rows and columns compose a 6×6 submatrix exactly coinciding with the STM in equation (3.19). Denoting each element of such submatrix with φ_{ij}, the following compact form of Jacobian can be used:

$$\tilde{\boldsymbol{J}}(\boldsymbol{\chi}(\tilde{\boldsymbol{X}}_0),\, \tilde{\boldsymbol{X}}_0) = \begin{bmatrix} \varphi_{11} & \varphi_{12} & \varphi_{13} & \varphi_{14} & \varphi_{15} & \varphi_{16} & \dot{\xi}_f \\ \varphi_{21} & \varphi_{22} & \varphi_{23} & \varphi_{24} & \varphi_{25} & \varphi_{26} & \dot{\eta}_f \\ \varphi_{31} & \varphi_{32} & \varphi_{33} & \varphi_{34} & \varphi_{35} & \varphi_{36} & \dot{\zeta}_f \\ \varphi_{41} & \varphi_{42} & \varphi_{43} & \varphi_{44} & \varphi_{45} & \varphi_{46} & \ddot{\xi}_f \\ \varphi_{51} & \varphi_{52} & \varphi_{53} & \varphi_{54} & \varphi_{55} & \varphi_{56} & \ddot{\eta}_f \\ \varphi_{61} & \varphi_{62} & \varphi_{63} & \varphi_{64} & \varphi_{65} & \varphi_{66} & \ddot{\zeta}_f \end{bmatrix}. \tag{3.38}$$

where the velocities and accelerations in the last column can be determined by evaluating the EoMs at the final state along the integrated trajectory, namely $\tilde{\boldsymbol{X}}_f$.

As mentioned, all of this correction scheme, where the influence of the variable integration time on the final state is quantified along the state evolution itself, is indicated as a VTDC procedure. On the other hand, if the integration time is a constrained quantity, then the Jacobian coincides in its full form with the STM and a FTDC has to be adopted.

3.4 Lyapunov orbits computation in the CR3BP

Underlying the POs computation procedure are two main considerations worth specifying preliminarily. Firstly, as previously noted, the CR3BP is an autonomous, time-invariant dynamical model. This implies there is no preferred direction of integration over time; indeed, integrating a correct initial state $\tilde{\boldsymbol{X}}_0^*$ over a whole period forward in time τ yields the same terminal conditions as integrating backward in time $-\tau$, provided the appropriate velocity components are correctly inverted. Secondly, according to the *mirror theorem* [54], POs in the CR3BP model that intersect a specific plane perpendicularly twice exhibit symmetrical configurations relative to that plane. Consequently, these observations lead to a more straightforward and efficient implementation of the shooting method; since the LO clearly shows symmetric properties with respect to the $\hat{\boldsymbol{\xi}}_S - \hat{\boldsymbol{\zeta}}_S$ plane, it is sufficient to compute only half the orbit. Then, the complete LO can be easily obtained in a single iteration by doubling the integration time.

As regards the computation of planar orbits in the CR3BP, a generic LO, which lies on the $\hat{\boldsymbol{\xi}}_S - \hat{\boldsymbol{\eta}}_S$ plane in the synodic frame, does not present neither position ζ nor velocity $\dot{\zeta}$ components in the out-of-plane direction. Moreover, due to its planar nature, when the LO crosses the $\hat{\boldsymbol{\xi}}_S - \hat{\boldsymbol{\zeta}}_S$ plane, it does not have also velocities along the $\hat{\boldsymbol{\xi}}_S$ direction, thus $\dot{\xi}_0 = \dot{\xi}_{\tau_f/2} = 0$. So, a simple targeting scheme would require to check if, after half orbit, the LO crosses the plane again perpendicularly. The design vector and the constrained vector are constructed accordingly to the provided considerations on the orbit. Therefore:

$$\tilde{\boldsymbol{X}}_0 = \begin{Bmatrix} \xi \\ \dot{\eta} \\ \tau \end{Bmatrix}, \tag{3.39}$$

where the only quantities allowed to vary and be corrected are the starting position on the $\hat{\boldsymbol{\xi}}_S$ axis, the initial velocity along the $-\hat{\boldsymbol{\eta}}_S$ direction (for a ξ_0 lying on the positive side of L2) and, if needed, the integration time. The terminal constraint vector, related to desired initial state $\tilde{\boldsymbol{X}}_0^*$, is thus defined as:

$$\boldsymbol{\chi}\left(\tilde{\boldsymbol{X}}_0^*\right) = \begin{Bmatrix} \eta_f \\ \dot{\xi}_f \end{Bmatrix} = \boldsymbol{0}. \tag{3.40}$$

The Jacobian can be directly computed by extracting the appropriate rows and columns from the complete matrix in equation (3.38). In particular, for the planar Lyapunov case, rows $\{2,4\}$ corresponding to $\{\eta_f, \dot{\xi}_f\}$ are extracted and then reduced only to the columns $\{1,5,7\}$, corresponding to $\{\xi_0, \dot{\eta}_0, \tau\}$:

$$\tilde{\boldsymbol{J}} = \begin{bmatrix} \varphi_{21} & \varphi_{25} & \dot{\eta}_f \\ \varphi_{41} & \varphi_{45} & \ddot{\xi}_f \end{bmatrix}. \tag{3.41}$$

Figure 3.1 shows a complete L2-centered LO family which has been computed via continuation strategy in the Earth-Moon binary system.

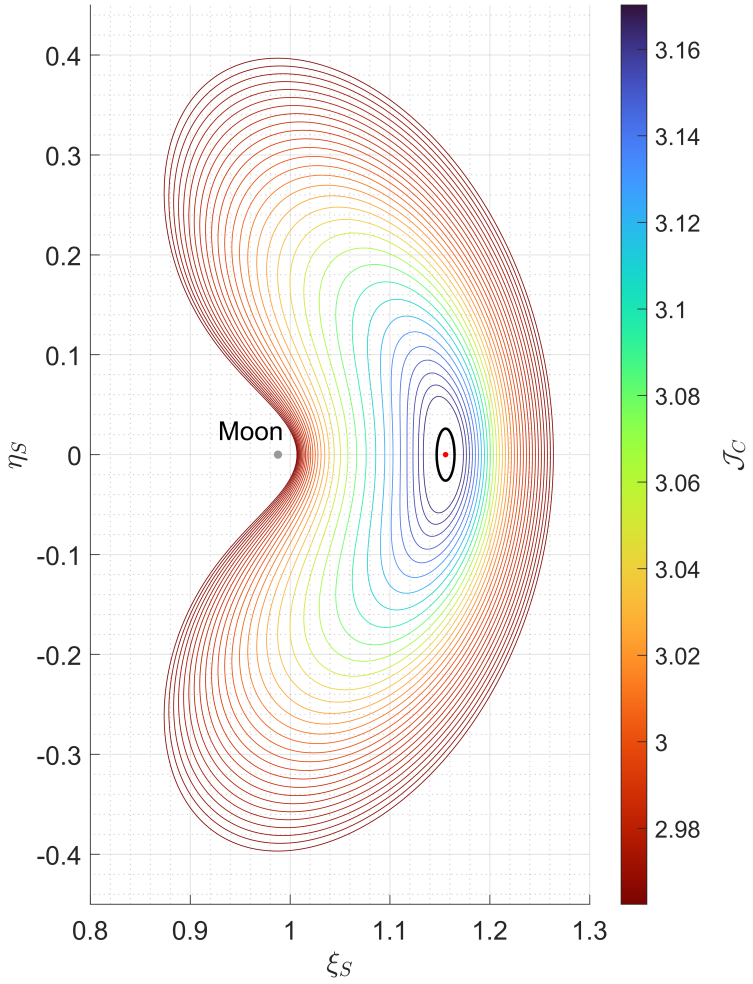

Fig. 3.2 L2 Lyapunov orbits family in the EM binary system.

An analytical LO of size $A_y = 1 \times 10^4$ km -i.e. the elliptical black orbit centered in L2- serves as starting point. To explore variations, the initial position ξ_0 is perturbed by a small finite step $d\xi_0$, which is kept fixed during the DC procedure, thus allowing only the initial velocities $\dot{\eta}_0$ and the integration time τ to be propagated. Due to nonlinearities, convergence robustness improves when the varying ξ_0 point is the one that produces smaller variations while increasing the orbit shape, more precisely the positive coordinate ξ beyond L2.

Please note from the colorbar that, as the LOs depart further from L2, they require greater energy, thus resulting in lower associated $\mathscr{J}_C$ values. Moreover, such larger orbits are distinguished by their characteristic cashew shape, whereas smaller LOs, with higher $\mathscr{J}_C$ values, closely reflect the elliptical geometry of the analytical one.

3.5 DROs computation in the CR3BP

Broucke, in his 1968 work *Periodic Orbits in the Restricted Three-Body Problem with Earth-Moon Masses* first mentioned the existence of DROs by exploring symmetric POs in the planar CR3BP [13]. In the same years, Hénon's studies emerged as a major reference on the subject [14–18], offering a comprehensive investigation of DROs in the Hill's Problem, a simplified case of the CR3BP. In this scenario, the system dynamics are considered primarily around the secondary body, assuming an infinite distance between the two primaries [52]. Nonetheless, the term *Distant Retrograde Orbit* (DRO) was apparently coined by Ocampo and Rosborough only twenty-five years later, in 1993 [28].

Analyzing several POs families in the Earth-Moon system, Hénon identified specific selenocentric POs characterized by a quasi-elliptical shape and very large radii with respect the closest primary (i.e. the Moon). DROs are indeed "distant" as they are situated at significant distances from the Moon, with medium radii extending tens of thousands of kilometers from the lunar surface. Moreover, these orbits exhibit a retrograde rotating motion, orbiting in the opposite direction to the Moon's trajectory. Such unique geometry, combined with their relative position within the Earth-Moon gravitational field, contributes to a high level of stability, leading DROs to be classified in the Hènon family f.

Unlike orbits near L1 and L2, which are unstable to small perturbations and require constant corrections to remain stable, DROs pass above these points at a greater distance, avoiding stability issues and maintaining their trajectory over time. These properties make DROs perfect solutions for long-term space missions, such as Earth or Moon observation missions, where frequent orbital corrections are typically required.

However, DROs are stable when only planar motion is considered; a change in stability can signal various bifurcations with other families of POs, even three-dimensional ones. Although studying such variants plays an important role in characterizing the dynamics of DROs, this thesis focuses solely on analyzing the relationship between DROs and LOs for the purpose of constructing these orbits. Since they are both planar orbits, the targeting scheme for DROs involves exactly the same design and constraint vectors seen in Section 3.3.2. The planar bifurcation from LOs, indeed, occurs when the tangential velocity $\dot{\eta}$ increases to such an extent as to produce orbits with greater amplitudes and lower $\mathscr{J}_C$, capable of exceeding even L1.

As per 3.39, the design vector is:

$$\tilde{\boldsymbol{X}}_0 = \begin{Bmatrix} \xi \\ \dot{\eta} \\ \tau \end{Bmatrix}. \tag{3.42}$$

Again, it is required that the orbit crosses the $\hat{\boldsymbol{\xi}}_S - \hat{\boldsymbol{\zeta}}_S$ plane with no velocity component along the $\hat{\boldsymbol{\xi}}_S$ direction, so:

$$\boldsymbol{\chi}\left(\tilde{\boldsymbol{X}}_0^*\right) = \begin{Bmatrix} \eta_f \\ \dot{\xi}_f \end{Bmatrix} = \mathbf{0}. \tag{3.43}$$

The reduced Jacobian matrix is the same of equation (3.41):

$$\tilde{\boldsymbol{J}} = \begin{bmatrix} \varphi_{21} & \varphi_{25} & \dot{\eta}_f \\ \varphi_{41} & \varphi_{45} & \ddot{\xi}_f \end{bmatrix}. \tag{3.44}$$

As for the Lyapunov case, the DC procedure allows only the initial velocity $\dot{\eta}_0$ and the integration time τ to vary at fixed initial position ξ_0. Here, the guess velocity

$\dot{\eta}_0$, again negative due to retrograde motion, is increased manually until an extended quasi-elliptical orbit -i.e. a DRO one- is obtained. In particular, by vaguely taking the Artemis I mission orbit as reference [24], a LO with $\xi_0 \approx 70,000$ km (kept fixed) is chosen as guess and only the $\dot{\eta}_0$ variable is modified.

Therefore, the targeted DRO is computed from the initial state:

$$\tilde{\boldsymbol{X}}_0 = \{1.180000, 0.000000, 0.000000, 0.000000, -0.498237, 0.000000\}^T,$$
$$\tau = 3.224769, \quad \mathscr{J}_C = 2.927885,$$

where $\dot{\eta}_0$ is the specific value of initial velocity that can be perturbed to retrieved the DRO family (Figure 3.4). Finally, such orbit is verified by comparing the solution with existing orbits in the NASA's database [55].

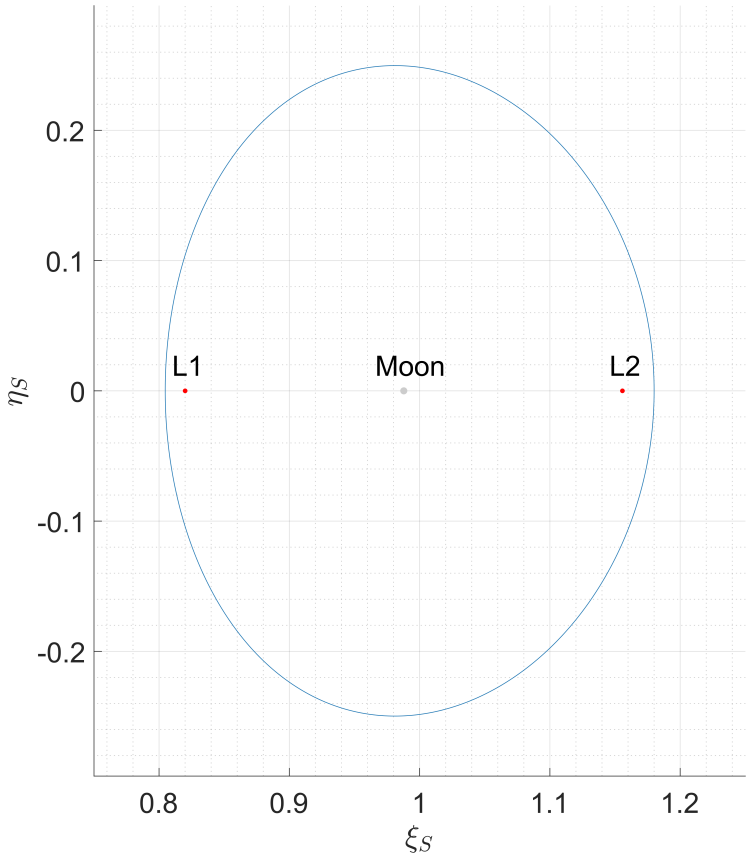

Fig. 3.3 Targeted Distant Retrograde Orbit.

The main characteristics of the implemented DRO are provided in Table 3.1 below.

Table 3.1 DRO characteristic properties.

Property	Value	Unit
Perilune	70392.55	km
Apolune	96058.13	km
Period	14.00	days

It is worth noting that such periodic orbits are only meaningful within the context of the CR3BP. When a generic trajectory is integrated in a higher-fidelity model, additional perturbations and influences from multi-body gravitation inevitably cause a nonlinear behavior, highly divergent from the expected one. Indeed, the concept of *periodicity* itself ceases to exist in the NBP. Therefore, specific strategies to tackle nonlinearities and aid convergence during the DC process are required.

To perform a transition from the POs just computed in the CR3BP to QPOs in the NBP, the ephemerides data must be taken into account. If implemented, this procedure would gradually replace the analytical solution with its medium-fidelity counterpart PO, then transitioned in the NBP via a time-dependent coordinate transformation. By defining a first guess integration time, corresponding to the guess period of QPO, a FTDC strategy should be employed.

After incorporating all the gravitational perturbations and achieving QPO final conditions relatively close to the initial ones within an acceptable error, it would be necessary to implement a subsequent VTDC to actually target and "close" the trajectory. Please remember that, while the generation of POs in the CR3BP provides only a valuable starting point for the optimization of the analyzed DRI scenario, such a complex transition to the NBP is beyond the scope of this thesis.

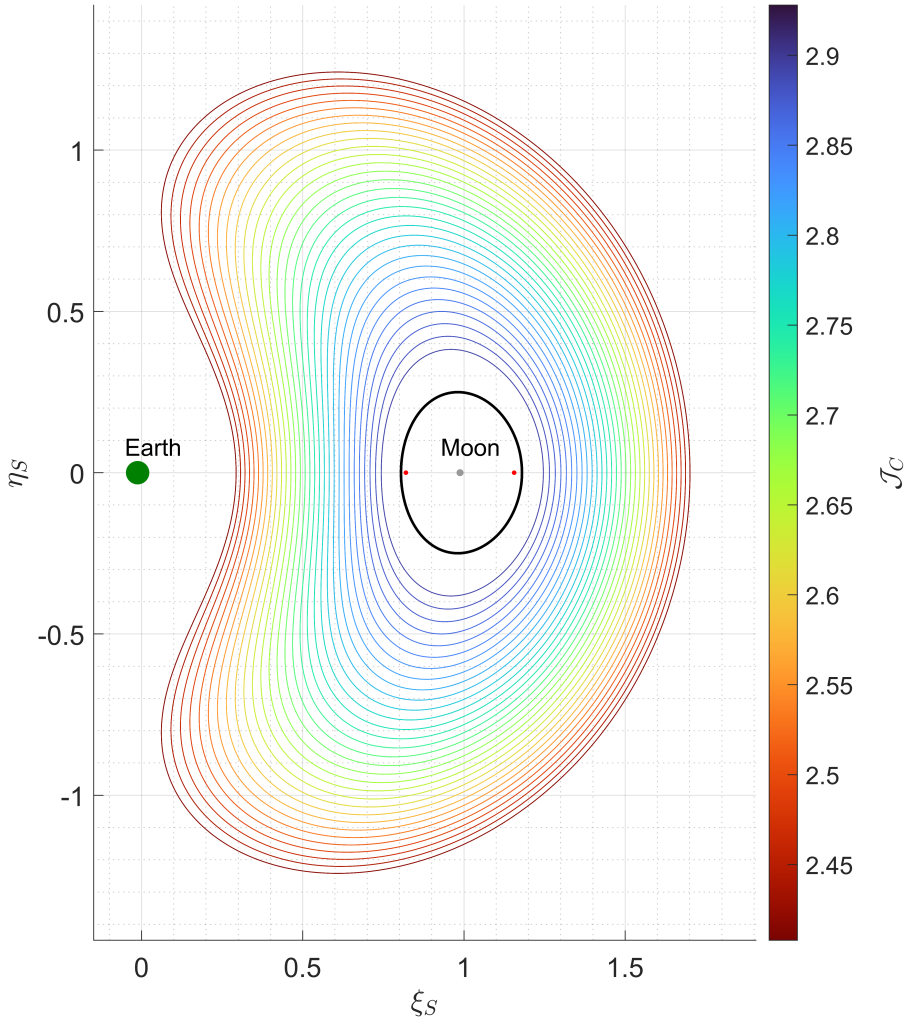

Fig. 3.4 DRO family in the EM binary system.

Chapter 4

Optimal Control Theory

Optimal Control Problems (OCPs) are a specific class of mathematical problems concerning the search for control actions able to optimize a certain performance index in a constrained dynamic system. The optimization can result in either a maximization or a minimization of the objective function, representative of the system behavior. Basically, this involves the identification of the most effective control law -one among the admissible strategies- which guides the system over time from an initial state to a desired final state, while considering system dynamics and constraints. Hereafter, necessary conditions that ensure an optimal solution will be outlined on the basis of Optimal Control Theory (OCT).

In space trajectories optimization, regardless of the specificities strictly related to the examined problem, it is possible to generalize the OCP in a time-continuous mathematical formulation, commonly adopted for finite-thrust mission scenarios. The problem conventionally revolves around maximizing the final mass of the spacecraft, which is equivalent to minimize the fuel consumption, or minimizing the time of flight. The selection of the proper merit index is essential to define the optimization problem in compliance with mission objectives and requirements. In this thesis the maximization of m_f is indeed proposed: the primary objective is to identify the lunar transfer requiring the lowest orbit insertion costs, thereby increasing the storable payload.

Due to the presence of nonlinearities in the objective function and/or constraints, no analytical solution is available, so OCPs are treated as Non Linear Programming Problems (NLPs), making them suitable to a wider range of numerical approaches.

Therefore, each complex OCP is decomposed into smaller and more manageable subproblems through a *transcription* process, aimed at finding an approximate discrete-time solution almost close to the continuous original one. The resulting discretized OCP can now be solved using numerical optimization methods, based on various iteration and approximation techniques. However, a comprehensive dissertation about nonlinear programming and transcription is provided in [56, 57], but such detailed analysis exceeds the bounds of this thesis. Betts also delved into NLPs numerical resolution, outlining all the mathematical aspects of different approaches [43, 58].

The structure of Chapter 4 is depicted below. The first section explores the numerical features of direct and indirect optimization, comparing them and offering an overview that corroborates the choice of an indirect procedure in the thesis. The presented approach broadly follows that provided by Mascolo [44], with additional references in [59, 60]. Section 4.2, indeed, offers a complete formulation of a generic OCP, delineated as a Two-Point Boundary Value Problem (TPBV), where constraints are imposed only at the extremal points of domain.

In the following sections, the numerical procedure implemented to solve this BVP is thoroughly detailed. The transition to a Multi-Point Boundary Value Problem (MPBVP), achieved by adding further conditions to intermediate nodes of trajectory, is also analyzed in a brief *excursus*. In the end, Section 4.5 delves into the application of OCT to space trajectory optimization, providing the basis for the examined case study.

4.1 Direct versus Indirect optimization methods

Numerical methods are essential to deal with the transcribed OCP, since they convert the initial infinite-dimensional problem into a new one with a finite dimension. As mentioned above, these optimization methods are broadly divided into two main classes: direct and indirect. Although Direct Methods (DMs) have historically been preferred due to their simpler implementation, since Lawden's studies in the 1950s [61–64], Indirect Methods (IMs) have been reevaluated in space trajectory optimization, making a comparison between these two approaches extremely interesting.

DMs offer a versatile strategy for treating complex problems in optimal control, given their high robustness and flexibility in handling dynamics and diverse constraints. As the name suggests, they tackle the OCP directly, performing a time-discretization of both state and controls, and solving differential equations via numerical integration; this implies that a large number of unknown variables arises, significantly increasing computational costs. The procedure consists in starting from a tentative solution, then evaluating the evolution of the performance index and constraints over time, and based on this, iteratively refining the initial guess again with the aim of optimize the cost function [65]. This parametric representation of the OCP, obtained bypassing the underlying dynamics of the system, may suffer from approximation errors and scarce accuracy, so that solution refinement techniques should be implemented. Unfortunately, the existence of such a strong correlation between the guesses and the final values can lead to a solution that is suboptimal, but not necessarily the optimal one. Moreover, the lack of theoretical insights into the nature of the problem completes the picture, making it difficult to understand whether such a solution is truly optimal.

Within this framework, IMs represent a viable alternative. Originated with the CoV (Bernoulli's brachistochronous curve problem, 1696 [1]), this approach provides a faster and more accurate solution at minimal computational costs [66]. Differently from DMs, the indirect optimization aims to maximize (or minimize) a functional, by first deriving the first-order necessary conditions for optimality, thus defining a Boundary Value Problem (BVP). Starting from initial guesses, the formulation involves evaluating the errors on Boundary Conditions (BCs) and then modifying the tentative solution to reduce such errors until convergence is achieved [67]. IMs have proven effective in solving sophisticated problems, from TPBVP to more articulate MPBVP, where the domain is partitioned into discrete subintervals and the internal nodes between them are conveniently constrained. The search for suitable adjoint variables, or costates, introduced to initialize the indirect optimization problem, poses a more significant challenge compared to DMs, inherently demanding considerable time and efforts from the user. Although, even in this case, the solution strictly depends on initial conditions, IMs delve deeper into the problem offering valuable theoretical insights about how to adjust the guesses and guide the solution towards optimality. As a result of such a complex implementation, in the last decades, IMs

[1] The brachistochronous is the curve that allows a massive particle to go from one point to another in the shortest possible time. This problem inspired Lagrange's work on CoV.

has often been relegated to the background in favor to direct ones. However, the use of appropriate techniques to improve their robustness has allowed IMs to be rediscovered and extended to a wide range of space trajectory applications. Further details on numerical methods comparison and state-of-art are explored in [68–72].

For all these reasons, the use of an IM in the present thesis is well-motivated. An iterative shooting procedure is proposed, demonstrating the effectiveness of such a IM in different mission scenarios, from impulsive orbital transfer to low-thrust manoeuvres. Moreover, among the best known methods, the Pontryagin's Maximum Principle (PMP) is employed, which provides necessary optimality conditions of controls and state variables through the introduction of the so-called Hamiltonian function [2].

4.2 General statement for Optimal Control Theory

The primary objective in OCT is to define the optimal control law that either maximizes or minimize a cost function, while satisfying all the system constraints. The control strategy must consider system evolution over time, leading it towards a desired final state and optimizing the functional along the way. As anticipated, the proposed formulation is specifically referred to space trajectory optimization problems. For the sake of brevity, the discussion will focus solely on maximization, omitting dual aspects related to minimization.

Formally, the trajectory evolution over time is governed by a set of first-order ODEs $\dot{\boldsymbol{x}}(t)$, which are derived from the fundamental principles of mechanics applied to the examined SC system. Given n state variables and m control variables, these equations, depending on both the state vector $\boldsymbol{x}(t) \in \mathbb{R}^n$ and the control vector $\boldsymbol{u}(t) \in \mathbb{R}^n$, can be written as:

$$\dot{\boldsymbol{x}}(t) = \boldsymbol{f}\left(\boldsymbol{x}(t), \boldsymbol{u}(t), t\right) \tag{4.1}$$

where the time t is an independent variable. Therefore, the OCP aims at identifying the optimal trajectory $\boldsymbol{x}^*(t)$, guided by optimal controls $\boldsymbol{u}^*(t)$, that maximizes the objective function $\mathcal{J}$. Such a merit index quantifies the system "performance", namely

[2] One valuable alternative to PMP is represented by the Hamilton-Jacobi-Bellman equations, which directly derive the optimal control policy through dynamic programming [73].

the effectiveness of control actions with respect to system dynamics and constraints, and takes the form:

$$\mathcal{J} = \varphi(\boldsymbol{x}_0, \boldsymbol{x}_f, t_0, t_f) + \int_{t_0}^{t_f} \Phi(\boldsymbol{x}(t), \boldsymbol{u}(t), t)\, dt \tag{4.2}$$

This functional is composed by two main scalar terms:

- The first one φ depends on the values that state variables and time have at the external boundaries (i.e. the extremal ones), giving particular weight to the desired final state.
- The second one Φ, integrated from the initial to the final time, reflects the trend of state quantities, controls, and time itself along the trajectory. It is a measure of *how* the solution evolves to reach the final condition.

This expression can be opportunely rearranged either in the Lagrange's formulation, with $\varphi = 0$, or in the Mayer's formulation, with $\Phi = 0$. As will be discussed further, the Mayer's formulation is adopted in this thesis. In the optimal condition, the merit index must be maximized, while satisfying any type of constraint that may be imposed on the state variables and time at the extremes of domain, so that a TPBVP arises. Such BCs are grouped in the constraint vector:

$$\boldsymbol{\chi}(\boldsymbol{x}_0, \boldsymbol{x}_f, t_0, t_f) = \mathbf{0}. \tag{4.3}$$

The control vector $\boldsymbol{u}$ may also be bounded to respect admissibility criteria, which are detailed later on. A simpler notation is proposed for clarity:

$$\varphi \triangleq \varphi(\boldsymbol{x}_0, \boldsymbol{x}_f, t_0, t_f), \tag{4.4a}$$

$$\boldsymbol{\chi} \triangleq \boldsymbol{\chi}(\boldsymbol{x}_0, \boldsymbol{x}_f, t_0, t_f). \tag{4.4b}$$

A *Bolza's problem* is thus defined; indeed, the equations (4.1) to (4.3) lay the foundation for such a classical TPBVP, aimed to optimize a system under specific BCs, by solving a set of time-continuous ODEs between two extremal states.

The implementation of IM can be now introduced, with its mathematical principles to be explored henceforth. This approach assumes the optimization of a new

merit index $\mathcal{J}^*$, obtained by inserting opportune auxiliary variables, that can be expressed as follows:

$$\mathcal{J}^* = \varphi + \boldsymbol{\mu}^T \boldsymbol{\chi} + \int_{t_0}^{t_f} \left[\Phi + \boldsymbol{\lambda}^T (\boldsymbol{f} - \dot{\boldsymbol{x}}) \right] dt. \tag{4.5}$$

Therefore, such augmented functional includes the adjoint variables, or costates, contained in the adjoint vector $\boldsymbol{\lambda}(t) \in \mathbb{R}^n$ and bijectively related to the state quantities, and the Lagrange multipliers $\boldsymbol{\mu} \in \mathbb{R}^m$, referred to BCs. The performed augmentation is tailored for OCPs, where the optimization is also subject to constraints. Indeed, for a generic non-converged solution (i.e. when $\boldsymbol{\chi} \neq \mathbf{0}$) state equations are not respected and $\dot{\boldsymbol{x}} \neq \boldsymbol{f}$, while for an optimal one both BCs and dynamics are satisfied, thus $\boldsymbol{\chi} = \mathbf{0}$ and $\dot{\boldsymbol{x}} = \boldsymbol{f}$ and, therefore, $\mathcal{J} = \mathcal{J}^*$. As a result, solving the problem in equation (4.5) then coincides with optimizing the original one in equation (4.2), one provided that all conditions are met.

In theory, since time derivatives $\dot{\boldsymbol{x}}(t)$ are unknown variables and must be integrated during the optimization, the process could be simplified by integrating the $-\boldsymbol{\lambda}^T \dot{\boldsymbol{x}}$ term in equation (4.5) by part:

$$\int_{t_0}^{t_f} (-\boldsymbol{\lambda}^T \dot{\boldsymbol{x}}) dt = -(\boldsymbol{\lambda}^T \boldsymbol{x}) \Big|_{t_0}^{t_f} + \int_{t_0}^{t_f} (\dot{\boldsymbol{\lambda}}^T \boldsymbol{x}) dt. \tag{4.6}$$

Thus, by substituting into the equation (4.6), one retrieves:

$$\mathcal{J}^* = \varphi + \boldsymbol{\mu}^T \boldsymbol{\chi} + (\boldsymbol{\lambda}_0^T \boldsymbol{x}_0 - \boldsymbol{\lambda}_f^T \boldsymbol{x}_f) + \int_{t_0}^{t_f} (\Phi + \boldsymbol{\lambda}^T \boldsymbol{f} + \dot{\boldsymbol{\lambda}}^T \boldsymbol{x}) dt. \tag{4.7}$$

All the indirect optimization process revolves around the system Hamiltonian $\mathcal{H}$, which appears in equation (4.7):

$$\mathcal{H} \triangleq \Phi + \boldsymbol{\lambda}^T \boldsymbol{f}. \tag{4.8}$$

Indeed, the Hamiltonian is an indispensable quantity to formulate the equations that describe the problem, namely the optimality, transversality, and the control equations. In IMs, maximizing the merit index $\mathcal{J}^*$ means respecting the first-order necessary conditions for optimality, therefore, the $\mathcal{J}^*$ has to be stationary at the optimal point, i.e. $\delta \mathcal{J}^* = 0$. With some mathematical manipulations, the first-order

differential $\delta\mathcal{J}^*$ attains the following form:

$$\delta\mathcal{J}^* = \left(\frac{\partial\varphi}{\partial t_0} + \boldsymbol{\mu}^T\frac{\partial\boldsymbol{\chi}}{\partial t_0} - \mathcal{H}_0\right)\delta t_0 + \tag{4.9a}$$

$$+\left(\frac{\partial\varphi}{\partial t_f} + \boldsymbol{\mu}^T\frac{\partial\boldsymbol{\chi}}{\partial t_f} + \mathcal{H}_f\right)\delta t_f + \tag{4.9b}$$

$$+\left(\frac{\partial\varphi}{\partial \boldsymbol{x}_0} + \boldsymbol{\mu}^T\frac{\partial\boldsymbol{\chi}}{\partial \boldsymbol{x}_0} + \boldsymbol{\lambda}_0^T\right)\delta\boldsymbol{x}_0 + \tag{4.9c}$$

$$+\left(\frac{\partial\varphi}{\partial \boldsymbol{x}_f} + \boldsymbol{\mu}^T\frac{\partial\boldsymbol{\chi}}{\partial \boldsymbol{x}_f} - \boldsymbol{\lambda}_f^T\right)\delta\boldsymbol{x}_f + \tag{4.9d}$$

$$+\int_{t_0}^{t_f}\left[\left(\frac{\partial\mathcal{H}}{\partial\boldsymbol{x}} + \dot{\boldsymbol{\lambda}}^T\right)\delta\boldsymbol{x} + \frac{\partial\mathcal{H}}{\partial\boldsymbol{u}}\delta\boldsymbol{u}\right]dt. \tag{4.9e}$$

Since $\delta\mathcal{J}^*$ must be null, a targeted choice of both costates $\boldsymbol{\lambda}$ and Lagrange multipliers $\boldsymbol{\mu}$ allows to nullify, for any variation in times, states, and controls, all their respective multiplying coefficients. Depending on which term is imposed equal to zero, a different condition arises, thus composing the entire set of the BVP boundary conditions. So, by nullifying the coefficients in lines (4.9a) and (4.9b), two algebraic equations at the initial and final times are defined, known as *transversality conditions*; lines (4.9c) and (4.9d) yield *optimality conditions*, namely $2n$ algebraic equations, each referred to a state quantity at both the external boundaries; finally, when the latter coefficients are null, line (4.9e) provides *n Euler-Lagrange equations* for the adjoint variables and *m* algebraic *control equations*. Hence, under the imposed BCs, the BVP is totally delineated by a total of $2 + 2n + m$ equations, which respectively determine 2 times (t_0 and t_f), n initial variables for both state ($\boldsymbol{x}$) and costate ($\boldsymbol{\lambda}$), and m multiplying coefficients ($\boldsymbol{\mu}$). All of these conditions will be examined below.

4.2.1 Boundary conditions for optimality

The transversality and optimality conditions dictate the behavior of trajectory at both times and states at the extremes of domain. These BCs, obtained by nullifying the coefficients of δt_0, δt_f, $\delta\boldsymbol{x}_0$, and $\delta\boldsymbol{x}_f$ in equations (4.9), compose the following set of ODEs:

$$\frac{\partial \varphi}{\partial t_0} + \boldsymbol{\mu}^T \frac{\partial \boldsymbol{\chi}}{\partial t_0} - \mathcal{H}_0 = 0 \tag{4.10a}$$

$$\frac{\partial \varphi}{\partial t_f} + \boldsymbol{\mu}^T \frac{\partial \boldsymbol{\chi}}{\partial t_f} + \mathcal{H}_f = 0 \tag{4.10b}$$

$$\frac{\partial \varphi}{\partial \boldsymbol{x}_0} + \boldsymbol{\mu}^T \frac{\partial \boldsymbol{\chi}}{\partial \boldsymbol{x}_0} + \boldsymbol{\lambda}_0^T = \mathbf{0} \tag{4.10c}$$

$$\frac{\partial \varphi}{\partial \boldsymbol{x}_f} + \boldsymbol{\mu}^T \frac{\partial \boldsymbol{\chi}}{\partial \boldsymbol{x}_f} - \boldsymbol{\lambda}_f^T = \mathbf{0}. \tag{4.10d}$$

Now, the role of Hamiltonian function $\mathcal{H}$ in the indirect optimization can be clarified. Indeed, from the two transversality equations (4.10a) and (4.10b), if the time appears neither in the function φ nor in the vector $\boldsymbol{\chi}$, the extremal values of Hamiltonian $\mathcal{H}_0$ and $\mathcal{H}_f$ are both null, and the values for time are dependent on the optimization. Conversely, if time is contained in $\boldsymbol{\chi}$, namely the initial and final times are fixed, then the respective Hamiltonian values are free and dependent on the process. Moreover, if the time variable is unconstrained but subject to optimization (i.e. generally minimization), the related Hamiltonian $\mathcal{H}_f$ is equal to 1.

The optimality equations (4.10c) and (4.10d) follow a similar reasoning. If a specific i-th state variable x_i does not feature nor in φ nor in $\boldsymbol{\chi}$, the associated costate λ_{x_i} is equal to zero. On the other hand, if such x_i is constrained, its adjoint variable results free at the same point. For a free state variable, for example the SC final mass, that has to be optimized (i.e. maximized), the corresponding costate is of unity.

To summarize the foregoing discussion, one has:

- if $\begin{Bmatrix} t_0 \\ t_f \end{Bmatrix} \notin \begin{Bmatrix} \varphi \\ \boldsymbol{\chi} \end{Bmatrix} \Rightarrow \begin{cases} \mathcal{H}_0 = 0 \\ \mathcal{H}_f = 0 \end{cases}$
- else if $\begin{Bmatrix} t_0 \\ t_f \end{Bmatrix} \in \begin{Bmatrix} \varphi \\ \boldsymbol{\chi} \end{Bmatrix} \Rightarrow \begin{cases} \mathcal{H}_0 \neq 0 \\ \mathcal{H}_f \neq 0 \end{cases}$
- if $\begin{Bmatrix} x_{i_0} \\ x_{i_f} \end{Bmatrix} \notin \begin{Bmatrix} \varphi \\ \boldsymbol{\chi} \end{Bmatrix} \Rightarrow \begin{cases} \lambda_{x_{i_0}} = 0 \\ \lambda_{x_{i_f}} = 0 \end{cases}$
- else if $\begin{Bmatrix} x_{i_0} \\ x_{i_f} \end{Bmatrix} \in \begin{Bmatrix} \varphi \\ \boldsymbol{\chi} \end{Bmatrix} \Rightarrow \begin{cases} \lambda_{x_{i_0}} \neq 0 \\ \lambda_{x_{i_f}} \neq 0 \end{cases}$

4.2.2 Equations for adjoint variables and controls

From the last line (4.9e) of equation (4.9) one can retrieve the set of ODEs that delineates the evolution of adjoint variables $\boldsymbol{\lambda}$ and controls $\boldsymbol{u}$ over time. By imposing the coefficients of $\delta\boldsymbol{x}$ equal to zero, the first set of n Euler-Lagrange equations for costates arises:

$$\frac{d\boldsymbol{\lambda}}{dt} = -\left(\frac{\partial \mathcal{H}}{\partial \boldsymbol{x}}\right)^T, \tag{4.11}$$

given that $\boldsymbol{\lambda}(t) \in \mathbb{R}^n$, and so its first-order derivatives $\dot{\boldsymbol{\lambda}}$. On the other hand, by imposing the coefficients of $\delta\boldsymbol{u}$ equal to zero, the set of m algebraic equations for controls is obtained:

$$\left(\frac{\partial \mathcal{H}}{\partial \boldsymbol{u}}\right)^T = 0. \tag{4.12}$$

As previously mentioned, the control vector $\boldsymbol{u}$ may be partially or totally constrained within certain limits of admissibility, such that $\boldsymbol{u}(\boldsymbol{x}(t), t) \in \boldsymbol{\mathcal{U}}$, where these control actions might depend on both state variables and time itself. Therefore, it suggests that a specific control variable u should be properly kept within the explicit range $\mathcal{U}_{min} < u < \mathcal{U}_{max}$.

This is where the Pontryagin's Maximum Principle (PMP) (or Pontryagin's minimum Principle, PmP, for minimization problems) is invoked; the optimal control $\boldsymbol{u}^* \in \boldsymbol{\mathcal{U}}$ is the one that, per each point in the desired trajectory, maximizes the Hamiltonian at that precise point. Such optimal law establishes the necessary conditions under which the control policy, resulting from the implemented method, is indisputably deemed optimal rather than suboptimal.

Furthermore, equation (4.12) implies that the i-th control u_i is not necessarily constrained to the admissible boundaries; according to the PMP, if $\mathcal{U}_{i,min} < u_i < \mathcal{U}_{i,max}$, such control is unbounded, otherwise it is assigned to the extremes of $\boldsymbol{\mathcal{U}}$.

However, depending on the derivation of Hamiltonian in equation (4.12), two cases arise:

$$\frac{\partial \mathcal{H}}{\partial u_i} = \begin{cases} f(u_i) & \text{if } \mathcal{H} \text{ nonlinear wrt } u_i, \\ k_{u_i} & \text{else if } \mathcal{H} \text{ affine}, \end{cases} \tag{4.13}$$

where k_{u_i} is constant. In the first case, the derivation yields a function of the bounded control u_i, setting the conditions that guide the control strategy. On the other hand, if the Hamiltonian $\mathcal{H}$ is linear, or *affine*, with respect to the control (except for $k_{u_i} = 0$), no information about the strategy to be adopted is provided, and a specific approach has to be sought. Specifically, a *bang-bang* control strategy is employed, influenced by the coefficient k_{u_i} resulting from derivation (4.13). For $k_{u_i} \neq 0$, the Hamiltonian is maximized by switching the control between its extremal allowable values, without assuming intermediate values. Therefore:

- the control is set to its maximum admissible value, $u_i = \mathcal{U}_{i,max}$, when $k_{u_i} > 0$,
- otherwise it is set to its minimum, $u_i = \mathcal{U}_{i,min}$, when $k_{u_i} < 0$.

Moreover, if $k_{u_i} = 0$, then bang-bang controls are not applicable, thus necessitating the introduction of singular arcs. As described in [74], this strategy occurs when the solution cannot be directly determined by applying PMP, but requires the evaluation of high-order conditions involving derivatives of the Hamiltonian function[3]. Fortunately, such complex scenario never arises in this thesis, since the Hamiltonian under investigation is affine to the control. Therefore, the selected control variable -the thrust T- is handled through a simpler bang-bang strategy, and commuted between its maximum T_{max} and its minimum value T_{min} (i.e., 0). Further details on the proposed model will be explored in Section 4.5.

Summarizing for a generic control u_i, from results of the Hamiltonian derivation in (4.12), the following applies:

- if $f(u_i) \quad \Rightarrow \quad \mathcal{U}_{i,min} < u_i < \mathcal{U}_{i,max}$,
- else if k_{u_i} $\begin{cases} > 0 & \Rightarrow \quad u_i = \mathcal{U}_{i,max}, \\ < 0 & \Rightarrow \quad u_i = \mathcal{U}_{i,min}, \\ = 0 & \Rightarrow \quad \text{singular arcs strategy.} \end{cases}$

[3]Differently from bang-bang controls (or nonsingular arcs), singular arcs involve additional conditions to identify the optimal control policy, such as the generalized Legendre-Clebsch condition.

4.3 Multi-Point Optimal Control Problem

Converting a TPBVP into a MPBVP could facilitate the intricacies of computational modeling, enhancing the numerical convergence of the solution algorithms and improving code robustness. Such a flexible approach breaks down complex dynamics into a number of n_p manageable subintervals, called indistinctly phases or arcs, while constraints are imposed in both external and internal points along the trajectory. Within each arc, variables are presumed to be continuous, at least up to the junction points, where discontinuities may arise as different arcs meet.

A schematic representation of the domain partition for a MPBVP is depicted in Figure 4.1.

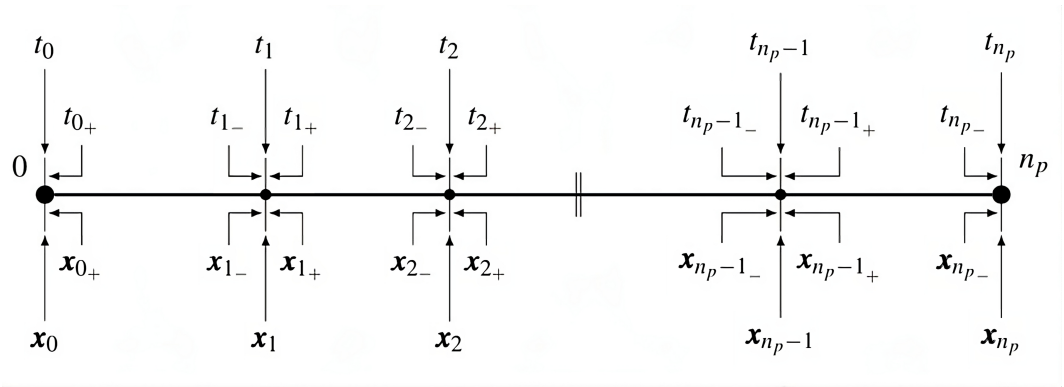

Fig. 4.1 Schematic representation of domain partition into multiple arcs [44].

The notation previously introduced in (4.1) to (4.3) for the TPBVP, is reformulated henceforth to accommodate the MPBVP. Thus, the subscript for each quantity denotes, from 0 to n_p, the considered node of the trajectory, with the addition of a plus or a minus sign, respectively referred to the values immediately before and after the boundary in the neighborhood of that point.

Therefore, the MPBVP merit index is defined as:

$$\mathcal{J} = \boldsymbol{\varphi}(\boldsymbol{x}_{(j-1)_+}, \boldsymbol{x}_{j-}, t_{(j-1)_+}, t_{j-}) + \sum_{j=1}^{n_p} \int_{t_{(j-1)_+}}^{t_{j-}} [\Phi(\boldsymbol{x}(t), \boldsymbol{u}(t), t)]\, dt, \tag{4.14}$$

where $\mathcal{J}$ is not only influenced by the values of both state and time variables for each node, but takes also into account *how* the solution evolves arc by arc.

In this case too, the BCs are generally Non Linear (NL) and again may depend on the state vector and time. So, one has:

$$\boldsymbol{\chi}(\boldsymbol{x}_{(j-1)_+}, \boldsymbol{x}_{j-}, t_{(j-1)_+}, t_{j-}) = \mathbf{0}, \quad j = 1, \ldots, n_p. \tag{4.15}$$

The augmented functional $\mathcal{J}^*$ incorporates the mentioned constraints, facilitating the search for the optimal point, while ensuring the solution compliance with the underlying conditions. It takes the form:

$$\mathcal{J}^* = \varphi + \boldsymbol{\mu}^T \boldsymbol{\chi} + \sum_{j=1}^{n_p} \int_{t_{(j-1)_+}}^{t_{j-}} \left[\Phi + \boldsymbol{\lambda}^T (\boldsymbol{f} - \dot{\boldsymbol{x}}) \right] dt. \tag{4.16}$$

and, after integrating by part:

$$\mathcal{J}^* = \varphi + \boldsymbol{\mu}^T \boldsymbol{\chi} + \sum_{j=1}^{n_p} \left[\boldsymbol{\lambda}_{(j-1)_+}^T \boldsymbol{x}_{(j-1)_+} - \boldsymbol{\lambda}_{j-}^T \boldsymbol{x}_{j-} \right] + \sum_{j=1}^{n_p} \int_{t_{(j-1)_+}}^{t_{j-}} \left[\Phi + \boldsymbol{\lambda}^T \boldsymbol{f} - \dot{\boldsymbol{\lambda}}^T \boldsymbol{x} \right] dt. \tag{4.17}$$

The first order differentiation $\delta\mathcal{J}^*$, expressed per each arc, is:

$$\delta\mathcal{J}^* = \left(\frac{\partial \varphi}{\partial t_{(j-1)_+}} + \boldsymbol{\mu}^T \frac{\partial \boldsymbol{\chi}}{\partial t_{(j-1)_+}} - \mathcal{H}_{(j-1)_+} \right) \delta t_{(j-1)_+} + \tag{4.18a}$$

$$+ \left(\frac{\partial \varphi}{\partial t_{j-}} + \boldsymbol{\mu}^T \frac{\partial \boldsymbol{\chi}}{\partial t_{j-}} + \mathcal{H}_{j-} \right) \delta t_{j-} + \tag{4.18b}$$

$$+ \left(\frac{\partial \varphi}{\partial \boldsymbol{x}_{(j-1)_+}} + \boldsymbol{\mu}^T \frac{\partial \boldsymbol{\chi}}{\partial \boldsymbol{x}_{(j-1)_+}} - \boldsymbol{\lambda}_{(j-1)_+}^T \right) \delta \boldsymbol{x}_{(j-1)_+} + \tag{4.18c}$$

$$+ \left(\frac{\partial \varphi}{\partial \boldsymbol{x}_{j-}} + \boldsymbol{\mu}^T \frac{\partial \boldsymbol{\chi}}{\partial \boldsymbol{x}_{j-}} - \boldsymbol{\lambda}_{j-}^T \right) \delta \boldsymbol{x}_{j-} + \tag{4.18d}$$

$$+ \sum_{j=1}^{n_p} \int_{t_{(j-1)_+}}^{t_{j-}} \left[\left(\frac{\partial \mathcal{H}}{\partial \boldsymbol{x}} + \dot{\boldsymbol{\lambda}}^T \right) \delta \boldsymbol{x} + \frac{\partial \mathcal{H}}{\partial \boldsymbol{u}} \delta \boldsymbol{u} \right] dt, \quad j = 1, \ldots, n_p. \tag{4.18e}$$

Instead of considering the transition of a single j-th arc from $t_{(j-1)_+}$ to t_{j-}, it is more efficient to focus on the boundary points themselves, which transversality and optimality conditions are explicitly formulated as:

$$\frac{\partial \varphi}{\partial t_{j_+}} + \boldsymbol{\mu}^T \frac{\partial \boldsymbol{\chi}}{\partial t_{j_+}} - \mathcal{H}_{j_+} = 0, \qquad j = 0, \ldots, n_p - 1 \tag{4.19a}$$

$$\frac{\partial \varphi}{\partial t_{j_-}} + \boldsymbol{\mu}^T \frac{\partial \boldsymbol{\chi}}{\partial t_{j_-}} + \mathcal{H}_{j_-} = 0, \qquad j = 1, \ldots, n_p \tag{4.19b}$$

$$\frac{\partial \varphi}{\partial \boldsymbol{x}_{j_+}} + \boldsymbol{\mu}^T \frac{\partial \boldsymbol{\chi}}{\partial \boldsymbol{x}_{j_+}} + \boldsymbol{\lambda}_{j_+}^T = \mathbf{0}, \qquad j = 0, \ldots, n_p - 1 \tag{4.19c}$$

$$\frac{\partial \varphi}{\partial \boldsymbol{x}_{j_-}} + \boldsymbol{\mu}^T \frac{\partial \boldsymbol{\chi}}{\partial \boldsymbol{x}_{j_-}} - \boldsymbol{\lambda}_{j_-}^T = \mathbf{0}, \qquad j = 1, \ldots, n_p. \tag{4.19d}$$

All the considerations on Euler-Lagrange and control equations, previously made for the TPBVP, remain essentially unchanged in the MPBVP domain.

4.4 Implementation of Boundary Value Problems

The main purpose of this thesis is to optimize transfer trajectories to lunar DROs within a medium-fidelity model that accurately reflects the CR3BP dynamics. This BVP implementation requires to address the numerical issues that arise as the IM is developed, along with managing the nonlinearities inherent in such a complex scenario. Consequently, it is essential to enhance code robustness and mitigate the solution high sensitivity with respect to variations in initial conditions.

To tackle these challenges, an augmented TPBVP has been formulated, as detailed in previous sections. Therefore, the initial state vector is now composed of the previous one extended with the adjoint vector:

$$\boldsymbol{y}_0 = \left\{ (\boldsymbol{x}_0)^T, (\boldsymbol{\lambda}_0)^T \right\}^T. \tag{4.20}$$

The objective is to identify the optimal initial state $\boldsymbol{y}_0^*$ that allows reaching the desired final state $\boldsymbol{y}_f^*$, while satisfying all BCs. The indirect optimization is performed through the single-shooting method earlier described in Section 3.3, selected for its straightforward implementation and low computational demands. This approach aligns with the aim of developing a practical and replicable solution methodology based on the IMs formulation, capable of handling the complex dynamics of the CR3BP. The entire procedure is explored in the following Section.

The set of governing equations to be integrated is generally reformulated as:

$$\dot{\boldsymbol{y}} = \boldsymbol{f}(\boldsymbol{y}(t), t), \tag{4.21}$$

Given that the OCP may involve also some constant variables, a new vector $\boldsymbol{z}$ can be employed:

$$\boldsymbol{z} = \left\{\boldsymbol{y}^T, \boldsymbol{c}^T\right\}^T, \tag{4.22}$$

obtained by coupling $\boldsymbol{y}$ with the constant vector $\boldsymbol{c}$. So, the system set of ODEs becomes:

$$\dot{\boldsymbol{z}} = \frac{d\boldsymbol{z}}{dt} = \boldsymbol{f}(\boldsymbol{z}(t), t), \tag{4.23}$$

where:

$$\dot{\boldsymbol{c}} = \frac{d\boldsymbol{c}}{dt} = \boldsymbol{0}. \tag{4.24}$$

All the constraints are satisfied if:

$$\boldsymbol{\chi}(\boldsymbol{z}) = \boldsymbol{0}. \tag{4.25}$$

As seen in Section 3.3, the implemented shooting procedure aims at finding the optimal initial state $\boldsymbol{q}_0^*$ which fulfills BCs $\boldsymbol{\chi}(\boldsymbol{q}^*) = \boldsymbol{0}$. The process starts by defining an initial guess for the state vector $\boldsymbol{q}_r = \boldsymbol{z}_0$, then proceeding iteratively. The error in BCs is computed between the values at the r-th iteration and the successive ones through a first-order Taylor expansion:

$$\boldsymbol{\chi}(\boldsymbol{q}_{r+1}) = \boldsymbol{\chi}(\boldsymbol{q}_r) + \frac{\partial \boldsymbol{\chi}(\boldsymbol{q}_r)}{\partial \boldsymbol{q}_{r+1}}(\boldsymbol{q}_{r+1} - \boldsymbol{q}_r). \tag{4.26}$$

In this approximation, the partial derivatives of the constraint vector $\boldsymbol{\chi}$ with respect to the state vector compose the Jacobian matrix $\boldsymbol{J}(\boldsymbol{\chi})$, which is crucial in understanding *how* small changes in $\boldsymbol{q}$ affect the problem, and thereby *how* to correct the guess after each iteration.

The following notation is introduced for brevity:

$$\boldsymbol{\chi}_r \triangleq \boldsymbol{\chi}(\boldsymbol{q}_r), \tag{4.27a}$$

$$\boldsymbol{J}(\boldsymbol{\chi}_r) \triangleq \boldsymbol{J}(\boldsymbol{\chi}(\boldsymbol{q}_r), \boldsymbol{q}_{r+1}). \tag{4.27b}$$

If the solution exists, then $\boldsymbol{\chi}_{r+1} = \mathbf{0}$ and therefore:

$$\boldsymbol{\chi}_r + [\boldsymbol{J}(\boldsymbol{\chi}_r)](\boldsymbol{q}_{r+1} - \boldsymbol{q}_r) = \mathbf{0}. \tag{4.28}$$

From this, it is possible to retrieve the state of the design vector $\boldsymbol{q}$ at each iteration:

$$\boldsymbol{q}_{r+1} = \boldsymbol{q}_r - [\boldsymbol{J}(\boldsymbol{\chi}_r)]^{-1}\boldsymbol{\chi}_r. \tag{4.29}$$

Rigorously, the Jacobian matrix should be exactly computed with respect to the examined homogeneous problem, introducing a new STM matrix for linear mapping. As per equation (3.18), the evolution of such matrix over time is described by its own set of ODEs, which would then need to be added to the system governing equations.

In this case, the Jacobian matrix $\boldsymbol{J}(\boldsymbol{\chi})$ is simply approximated via the forward finite-difference methods as:

$$\boldsymbol{J}(\boldsymbol{\chi}_r) = \frac{\boldsymbol{\chi}_r^p - \boldsymbol{\chi}_r}{\Delta}, \tag{4.30}$$

where each free-variable element of vector $\boldsymbol{q}^p$ is perturbed with a $\Delta = 1 \times 10^{-7}$:

$$\chi_{i_r}^p \triangleq \chi(q_{i_r}^p), \tag{4.31a}$$

$$q_{i_r}^p \triangleq q_{i_r} + \Delta. \tag{4.31b}$$

This approximation makes the problem adaptable to any variation in constraints, initial conditions, or even time schemes, allowing for more flexible analyses.

In conclusion, the presented TPBVP is governed by the system:

$$\dot{\boldsymbol{z}} = \boldsymbol{f}(\dot{\boldsymbol{z}}(t), t), \tag{4.32}$$

formed by the sole set of system principal ODEs. By integrating simultaneously them, it is possible to determine the optimal initial state $\boldsymbol{z}_0$ which allows to reach the desired

final state $\boldsymbol{z}_f(\boldsymbol{z}_0(t), t_0)$ while respecting the imposed constraints $\boldsymbol{\chi}$. Such integration relies on the Adams-Moulton numerical approach, an implicit and linear multistep method with variable step size and order [75, 76]. Specifically, the algorithm implements the LSODA Python integrator, known for its stability and robustness, making it well-suited to handle stiff differential equations [77]. In addition, the code is precompiled in C++ language, significantly enhancing computational capabilities. This hybrid approach leverages the speed and efficiency of C++ while maintaining the flexibility and ease of use of Python. On a standard 2.80 GHz CPU laptop with an i7 Intel Core processor, LSODA proves particularly effective, achieving convergence with computation times of 1 hundredth of second per iteration and an error tolerance of 1e-7. This precision, combined with the inherent speed of the indirect method, allows for the calculation of multiple solutions in a very short time frame.

In order to improve the iterative procedure, two numerical techniques are also implemented:

- A relaxation parameter κ_1 is introduced during the correction per each iteration:

$$\boldsymbol{z}_{r+1} = \boldsymbol{z}_r - \kappa_1 \cdot [\boldsymbol{J}(\boldsymbol{\chi}_r)]^{-1} \boldsymbol{\chi}_r, \tag{4.33}$$

  where $\kappa_1 = 1 \times 10^{-3} \div 1 \times 10^{-5}$. Usually, lower values are suitable during the initial assumptions for unknown variables, whereas higher values can be chosen only when the solution is reasonably close to the optimal one.

- Let be $E_{max} = \max(\chi_i)$ the code required precision. At the end, a control on boundary conditions is imposed between the error at each iteration and the subsequent one:

$$E_{max,r+1} < \kappa_2 \cdot E_{max,r}, \tag{4.34}$$

  where $\kappa_2 = 2 \div 3$. The latter parameter is effective in facilitating the convergence of first step, even tough the first couple of steps increase the maximum error while establishing the proper optimality direction in the search space. If the error becomes significantly large, then the equation (4.34) does not hold and a bisection method is applied on the correction up to five times. After that, the process is automatically stopped since it is unable to converge from the selected attempt solution.

4.5 OCT for space trajectory applications

The spacecraft CR3BP dynamical system subject to optimization is [78]:

$$\frac{d\xi}{dt} = \dot{\xi} \tag{4.35a}$$
$$\frac{d\eta}{dt} = \dot{\eta} \tag{4.35b}$$
$$\frac{d\zeta}{dt} = \dot{\zeta} \tag{4.35c}$$
$$\frac{d\dot{\xi}}{dt} = 2\dot{\eta} + \xi - \frac{1-\mu}{\rho_{13}^3}(\xi+\mu) - \frac{\mu}{\rho_{23}^3}[\xi-(1-\mu)] + \frac{T_\xi}{m} \tag{4.35d}$$
$$\frac{d\dot{\eta}}{dt} = -2\dot{\xi} + \eta - \frac{1-\mu}{\rho_{13}^3}\eta - \frac{\mu}{\rho_{23}^3}\eta + \frac{T_\eta}{m} \tag{4.35e}$$
$$\frac{d\dot{\zeta}}{dt} = -\frac{1-\mu}{\rho_{13}^3}\zeta - \frac{\mu}{\rho_{23}^3}\zeta + \frac{T_\zeta}{m} \tag{4.35f}$$
$$\frac{dm}{dt} = -\frac{T}{c} \tag{4.35g}$$

or, in compact form:

$$\frac{d\boldsymbol{\rho}}{dt} = \boldsymbol{\mathcal{V}} \tag{4.36a}$$
$$\frac{d\boldsymbol{\mathcal{V}}}{dt} = \boldsymbol{g}(\boldsymbol{\rho}) + \boldsymbol{\hbar}(\boldsymbol{\mathcal{V}}) + \frac{\boldsymbol{T}}{m} \tag{4.36b}$$
$$\frac{dm}{dt} = -\frac{T}{c}, \tag{4.36c}$$

where $\boldsymbol{\rho} = \{\xi, \eta, \zeta\}^T$ and $\boldsymbol{\mathcal{V}} = \left\{\dot{\xi}, \dot{\eta}, \dot{\zeta}\right\}^T$ are the nondimensional position and velocity vectors. The functions $\boldsymbol{g}(\boldsymbol{\rho})$ and $\boldsymbol{\hbar}(\boldsymbol{\mathcal{V}})$, introduced to compact the equations, are respectively:

$$\boldsymbol{g}(\boldsymbol{\rho}) = \left\{ \begin{array}{c} \xi - \frac{1-\mu}{\rho_{13}^3}(\xi+\mu) - \frac{\mu}{\rho_{23}^3}[\xi-(1-\mu)] \\ \eta - \frac{1-\mu}{\rho_{13}^3}\eta - \frac{\mu}{\rho_{23}^3}\eta \\ -\frac{1-\mu}{\rho_{13}^3}\zeta - \frac{\mu}{\rho_{23}^3}\zeta \end{array} \right\} \tag{4.37a}$$

$$\boldsymbol{\hbar}(\boldsymbol{\mathcal{V}}) = \left\{ \begin{array}{c} 2\dot{\eta} \\ -2\dot{\xi} \\ 0 \end{array} \right\} \tag{4.38b}$$

The first two lines, (4.36a) and (4.36b), are obtained from equations (2.30) by adding the thrust term $\boldsymbol{T}$, while the last equation (4.36c) represents the mass consumption due to the propulsion, strictly depending on the effective exhaust velocity $c = I_{sp} g_0$. The spacecraft mass m and the thrust magnitude T are non-dimensionalized by using the initial spacecraft mass m_0.

Such system of ODEs characterizes an OCP aimed at finding the optimal control law $\boldsymbol{u}^*(t)$ that maximizes the merit index, generally equivalent to the final mass of the spacecraft.

The Mayer formulation is preferred here, so one has:

$$\mathcal{J} = \varphi = m_f. \tag{4.39}$$

The state vector $\boldsymbol{x}(t) \in \mathbb{R}^n$ is:

$$\boldsymbol{x} = \left\{ \xi, \quad \eta, \quad \zeta, \quad \dot{\xi}, \quad \dot{\eta}, \quad \dot{\zeta}, \quad m \right\}^T, \tag{4.40}$$

the variables of which are associated to their corresponding adjoint variables, thus composing the augmented state vector $\boldsymbol{y}(t) \in \mathbb{R}^{2n}$:

$$\boldsymbol{y} = \left\{ \begin{array}{cccccccccccccc} \xi, & \eta, & \zeta, & \dot{\xi}, & \dot{\eta}, & \dot{\zeta}, & \lambda_\xi, & \lambda_\eta, & \lambda_\zeta, & \lambda_{\dot{\xi}}, & \lambda_{\dot{\eta}}, & \lambda_{\dot{\zeta}}, & m, & \lambda_m \end{array} \right\}^T. \tag{4.41}$$

Please note that the vector $\boldsymbol{y}$ has no superscript here, but already contains the nondimensional quantities according to the CR3BP formulation. Moreover, $\boldsymbol{y}$ coincides with the vector $\boldsymbol{z}$ seen previously, since there are no additional constants in this case ($\boldsymbol{c} = \boldsymbol{0}$).

By expressing the EoMs, as discussed in (4.35), the Hamiltonian is specifically defined for space trajectory OCPs:

$$\begin{aligned}\mathcal{H} = \boldsymbol{\lambda}^T \boldsymbol{f} = \sum_{i=1}^{2n} \lambda_i f_i = \lambda_\xi \dot{\xi} + \lambda_\eta \dot{\eta} + \lambda_\zeta \dot{\zeta} + \\ + \lambda_{\dot{\xi}} \left[2\dot{\eta} + \xi - \frac{1-\mu}{\rho_{13}^3}(\xi+\mu) - \frac{\mu}{\rho_{23}^3}(\xi - 1 + \mu) + \frac{T_\xi}{m} \right] + \\ + \lambda_{\dot{\eta}} \left[-2\dot{\xi} + \eta - \frac{1-\mu}{\rho_{13}^3}\eta - \frac{\mu}{\rho_{23}^3}\eta + \frac{T_\eta}{m} \right] + \\ + \lambda_{\dot{\zeta}} \left[-\frac{1-\mu}{\rho_{13}^3}\zeta - \frac{\mu}{\rho_{23}^3}\zeta + \frac{T_\zeta}{m} \right] + \\ - \lambda_m \frac{T}{c},\end{aligned} \tag{4.42}$$

or, in compact form:

$$\mathcal{H} = \boldsymbol{\lambda}_\rho^T \boldsymbol{\mathcal{V}} + \boldsymbol{\lambda}_\mathcal{V}^T \left[\boldsymbol{g}(\boldsymbol{\rho}) + \boldsymbol{h}(\boldsymbol{\mathcal{V}}) + \frac{\boldsymbol{T}}{m} \right] - \lambda_m \frac{T}{c}, \tag{4.43}$$

where $\boldsymbol{\lambda}_\rho$ and $\boldsymbol{\lambda}_\mathcal{V}$ are respectively the adjoint vectors for position and velocity.

By grouping all terms multiplying the thrust-to-mass ratio, one obtains:

$$\mathcal{H} = \boldsymbol{\lambda}_\rho^T \boldsymbol{\mathcal{V}} + \boldsymbol{\lambda}_\mathcal{V}^T [\boldsymbol{g}(\boldsymbol{\rho}) + \boldsymbol{h}(\boldsymbol{\mathcal{V}})] + T \left(\frac{\boldsymbol{\lambda}_\mathcal{V}^T}{m} \frac{\boldsymbol{T}}{T} - \frac{\lambda_m}{c} \right), \tag{4.44}$$

thus finding that the Hamiltonian is linear with respect to the control $\boldsymbol{u}(t)$, namely the thrust vector $\boldsymbol{T}$ in its magnitude and direction. For this reason, as seen in Section 4.2.2, a bang-bang control must be implemented. Such operation is performed by means of the *Switching Function* (SF) parameter, obtained in equation (4.44) as:

$$\mathcal{S}_\mathcal{F} = \frac{\boldsymbol{\lambda}_\mathcal{V}^T}{m} \frac{\boldsymbol{T}}{T} - \frac{\lambda_m}{c}. \tag{4.45}$$

Therefore, in accordance with the PMP, the optimal control which maximizes the merit index (i.e. m_f) is the thrust that maximizes the Hamiltonian:

$$\mathcal{H} = \boldsymbol{\lambda}_\rho^T \boldsymbol{\mathcal{V}} + \boldsymbol{\lambda}_\mathcal{V}^T [\boldsymbol{g}(\boldsymbol{\rho}) + \boldsymbol{h}(\boldsymbol{\mathcal{V}})] + T \mathcal{S}_\mathcal{F}. \tag{4.46}$$

The bang-bang technique implies a control to be modulated along the trajectory as follows; the thrust is maximized, $T = T_{max}$, when $\mathcal{S}_{\mathcal{F}} > 0$, while it is imposed null, $T = 0$, when $\mathcal{S}_{\mathcal{F}} < 0$, thus defining the entire control strategy. For a MPBVP, unfortunately not employed here, such technique would be implemented arc by arc, strictly guiding the trajectory during the mission. The singular arcs scenario, instead, which requires the computation of SF time derivatives, is definetively excluded from the discussion.

As regards the thrust direction, Lawden provides an important insight [61]: the optimal thrust direction that maximizes the switching function, and consequently the Hamiltonian in (4.44), is parallel to the adjoint velocity vector $\boldsymbol{\lambda}_{\mathcal{V}}$, named *Primer vector*:

$$\boldsymbol{\lambda}_{\mathcal{V}} = \begin{Bmatrix} \lambda_{\dot{\xi}} \\ \lambda_{\dot{\eta}} \\ \lambda_{\dot{\zeta}} \end{Bmatrix}, \quad \lambda_{\mathcal{V}} = \|\boldsymbol{\lambda}_{\mathcal{V}}\|. \tag{4.47}$$

As a result, the switching function $\mathcal{S}_{\mathcal{F}}$ in equation (4.45) can be rewritten in its scalar form as:

$$\mathcal{S}_{\mathcal{F}} = \frac{\lambda_{\mathcal{V}}}{m} - \frac{\lambda_m}{c}. \tag{4.48}$$

The thrust $\boldsymbol{T}$ vector can be decomposed via its two characteristic angles, the in-plane angle α_T and the out-of-plane angle β_T, as shown in Figure 4.2:

$$\boldsymbol{T} = \begin{Bmatrix} T_\xi \\ T_\eta \\ T_\zeta \end{Bmatrix} = T \begin{Bmatrix} \cos\alpha_T \cos\beta_T \\ \sin\alpha_T \cos\beta_T \\ \sin\beta_T \end{Bmatrix}, \quad T = \|\boldsymbol{T}\|. \tag{4.49}$$

The optimal values for these angles are retrieved by deriving the Hamiltonian in equation (4.42) with respect to the thrust angles themselves:

$$\frac{\partial \mathcal{H}}{\partial \alpha_T} = -\lambda_{\dot{\xi}} \sin\alpha_T + \lambda_{\dot{\eta}} \cos\alpha_T = 0 \tag{4.50a}$$

$$\frac{\partial \mathcal{H}}{\partial \beta_T} = \lambda_{\dot{\zeta}} \cos\beta_T - \left(\lambda_{\dot{\xi}} \cos\alpha_T + \lambda_{\dot{\eta}} \sin\alpha_T\right) \sin\beta_T = 0. \tag{4.50b}$$

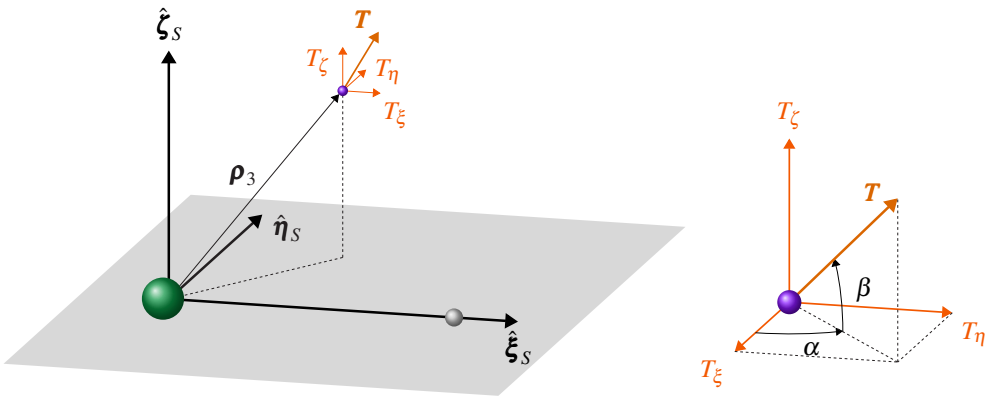

Fig. 4.2 Thrust angles in the synodic EM RF.

Then, the following optimal directions are obtained:

$$\cos\alpha_T \cos\beta_T = \frac{\lambda_{\dot{\xi}}}{\lambda_{\mathcal{V}}} \tag{4.51a}$$

$$\sin\alpha_T \cos\beta_T = \frac{\lambda_{\dot{\eta}}}{\lambda_{\mathcal{V}}} \tag{4.51b}$$

$$\sin\beta_T = \frac{\lambda_{\dot{\zeta}}}{\lambda_{\mathcal{V}}} \tag{4.51c}$$

which coincide with the cosine directors of the thrust vector $\boldsymbol{T}$. Therefore, the optimal thrust angles are easily computed from equations (4.51a) to (4.51c) via primer vector $\boldsymbol{\lambda}_{\mathcal{V}}$. The augmented BVP is finally completed by finding the adjoint variables via integration from equation (4.11). Their problem-specific form is presented in Appendix B.

During an indirect optimization process in highly nonlinear dynamical systems, the evaluation of error gradients demands great computational efforts and time. For such a complex CR3BP model, the implemented gravitational interactions may affect the procedure, giving rise to numerical issues in handling thrust discontinuities. Indeed, when the switching function oscillates around zero changing its sign multiple times during the integration, the automatic sequence of thrust-coast phases may be compromised, leading to the elimination of a desired thrust phase ($\mathcal{S}_\mathcal{F} > 0$) or to the introduction of an unwanted coast phase ($\mathcal{S}_\mathcal{F} < 0$). Moreover, if a solution is on the border between two different switching families, for example a two-burn (T-C-T) and a three-burn (T-C-T-C-T) structure, the switching function may oscillate indefinetively without converging.

Over the years, several numerical techniques have been implemented to address these critical issues, from smoothing techniques [79] to the most recent integrated control regularization method [80], but their investigation is beyond the scope of this research. A different approach implies that the problem's switching structure is specified *a priori*, thus defining a tailored series of thrust-coast phases along the entire trajectory. Such an arc sequence is modified only if the PMP is violated, following the strategic corrections suggested by the examined switching function. An additional boundary condition is imposed, fixing the switching function to zero when the thruster is turned on or off (i.e. at switching points). In this way, the procedure robustness is significantly enhanced, accelerating convergence and increasing numerical precision.

However, it is important to highlight that while this approach is well-suited for the analysis, it was not implemented due to time constraints and the inherent complexity of the method.

Chapter 5

Lunar transfer trajectories to Distant Retrograde Orbits in the CR3BP

Chapter 5 describes the actual scenario of this thesis, aimed at finding optimal Earth-Moon direct transfers that ensure a final DRO insertion (DRI) with minimum propellant usage. All the examined trajectories result from the implemented TPBVP, grounded on the optimal control IM formulation and the use of a bang-bang thrust control law. The dynamical model considers a three-body gravitation under the assumptions of the CR3BP, whose EoMs have been presented in Chapter 2.

As anticipated, the core of the analysis involves searching for the optimal costates that allow the spacecraft to thrust in preferential directions and correct the trajectory while satisfying all imposed constraints. The complexity of the CR3BP model makes this research more challenging, as the solution may exhibit unexpected behaviors due to the combined gravitational effects.

The case study is perfectly framed by introducing all the boundary conditions characterizing the lunar transfers. This includes reporting the features of the spacecraft and the selected engine, as well as the initial conditions for departure from Earth and the terminal conditions to insert into DRO. The target orbit is computed via a single-shooting procedure and STM, as seen in Chapter 2, employing a fixed-time correction scheme.

There are multiple potential applications for these results. Optimizing such EM transfers can significantly enhance mission efficiency, reducing costs for lunar exploration and establishing a reliable supply chain for lunar bases [32]. Additionally,

the stable nature of the DRO makes it an ideal location not only for approaching the Moon but also for long-term scientific missions, space telescopes, and as a staging point for deeper space exploration [33–35].

5.1 Boundary conditions

5.1.1 Spacecraft propulsion system

This section introduces the specific properties of the spacecraft, which is assumed to be punctiform, and describes the thruster it is equipped with for the examined scenario.

To overcome the physical limitations of traditional chemical propulsors, which have low specific impulses (at best, $I_{sp} = 350 \div 450$ s), Electrical Propulsion (EP) is preferred here. EP thrusters are characterized by very high I_{sp}, on the order of thousands of seconds, depending on the engine's operating principle, whether electrothermal, electrostatic, or electromagnetic. On the other hand, these devices produce lower accelerations over time, necessitating an effective ΔV greater than the ideal one and thus extending thrust phases for hours, days, or even weeks. Since the goal of this analysis is solely to preserve propellant, irrespective of mission duration, engine efficiency is crucial. Other considerations regarding eclipse periods, during which solar power supply ceases, are beyond the scope of this thesis.

Several EP thrusters have been developed and tested over the past decades; however, none of these have been used as a reference since their applications are usually limited to small correction maneuvers. For a complete Earth-Moon transfer, an ideal electrostatic thruster with rather optimistic specifications has been selected. These characteristics, including thrust, specific impulse, and the total mass of the satellite, are provided in Table 5.1 below.

Table 5.1 SC characteristic properties.

Quantity	Value	Unit
m_0	1000	kg
I_{sp}	3000	s
T	1.0	N

Thrust and specific impulse are considered constant, resulting in the bang-bang control discussed in Section 4.5.

Although the ultimate goal is to identify cost-effective trajectories by minimizing propellant requirements, the implemented problem actually optimizes the SC final mass. The relationship between mass consumption and velocity change, namely the cost of maneuvering, is expressed by the Tsiolkovsky equation:

$$\Delta V = -I_{sp} g_0 \ln\left(\frac{m_f}{m_0}\right), \tag{5.1}$$

where:

$$m_p = m_0 - m_f. \tag{5.2}$$

Please note that the propellant mass m_p generally constitutes around $10 \div 15\%$ of the initial mass m_0.

5.1.2 Initial conditions

To accurately define an EM transfer, a proper selection of the initial and final conditions is essential. While the final points on the orbit are well-known, the challenge arises with the initial point, the state of which, especially the velocities, is unknown regardless of the selected location.

Leveraging the lack of a preferential direction of integration over time, as discussed in Section 3.4, the trajectory is integrated backward in time, starting from the DRO and arriving near Earth. Therefore, by reversing the integration time, the initial point of this integration will coincide with the target of the transfer, while the final point will provide the departure point of the transfer itself.

In particular, the trajectory is computed by integrating equations (2.30), without considering any thrust; the aim of this strategy is only to obtain a reference trajectory, so no correction is needed. The point at $\eta = 0$ on DRO, used as the starting point for the orbit computation in Section 3.5, is selected as the initial condition for the integration:

$$\{1.180000, 0.000000, 0.000000, 0.000000, -0.498237, 0.000000\}^T,$$

A grid-search method is employed to identify the final (nondimensional) $\Delta\mathcal{V}_f$ components along the $\hat{\boldsymbol{\xi}}_S$ and the $\hat{\boldsymbol{\eta}}_S$ directions, which, combined, allow the DRI maneuver. As a result, the final velocities $\dot{\xi}$ and $\dot{\eta}$ have to be increased by:

$$\Delta\mathcal{V}_f = \left\{ \begin{array}{c} 0.1000 \\ -0.5000 \end{array} \right\}. \tag{5.3}$$

The integration time, which is negative, is gradually increased until the final point of the trajectory is within a certain distance from Earth, here set to 20000 km. So, by integrating backward for 5.6954 days, the following point is retrieved:

$$\{-0.008135,\ -0.051873,\ 0.000000,\ 5.979900,\ -0.240686,\ 0.000000\}^T,$$

which can be considered as a generic point on a circular parking MEO with a radius of 20000 km, used to leave the planet. The whole integrated trajectory is represented in Figure 5.1, where the radii of Earth and Moon are multiplied by a scale factor of 1000 for representation purposes.

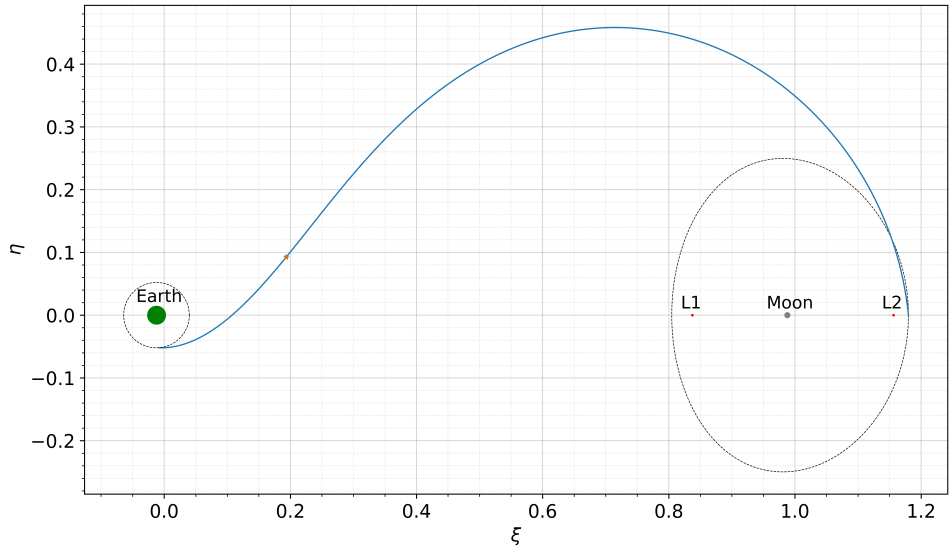

Fig. 5.1 EM transfer integrated backward over time.

However, since the code shows high sensitivity even to very small variations in velocity near Earth, it is preferred to break the trajectory to concentrate corrections only in the second part during the optimization. In other words, this strategy exploits

manually the same principle behind the MPBVP already seen in Section 4.3, where the trajectory is automatically divided into multiple arcs. This breakpoint, marked with a yellow star on the plot, is obtained by cutting off the integration time to 5.40 days:

$$\{0.193506, 0.092323, 0.000000, 1.634975, 2.003608, 0.000000, \}^T .$$

Consequently, the initial mass m_0 has to change, taking into account the fuel burned during the first half. Again, from the Tsiolkovsky equation, one has:

$$m_0^b = m_0 e^{-\frac{\Delta V_0}{c}} = 944.65\,\text{kg}, \tag{5.4}$$

where the superscript b indicates the residual mass at breakpoint after the first segment and will be omitted henceforth for clarity. The ΔV_0 coincides with the difference between the starting velocity on the trajectory and the circular velocity on MEO:

$$\Delta V_0 = \|V_0\| - V_{MEO} = \|V_0\| - \sqrt{\frac{\mu_E}{r_{MEO}}} = 1.6737\,\text{km/s}. \tag{5.5}$$

This new initial mass and the state of breakpoint now represent the real initial conditions $\boldsymbol{x}_0$ for the optimization problem:

$$\boldsymbol{x}_0 = \{0.193506, 0.092323, 0.000000, 1.634975, 2.003608, 0.000000, 1.000000\}^T ,$$

where the last unit value is exactly the mass, which is nondimensionalized by the SC mass itself.

To ensure the process converges, these quantities must be accompanied by seven reasonable adjoint variables, associated to initial mass, position and velocities, which are unknown. While some demonstrate a perceivable progression over time, others exhibit a less predictable behavior. The magnitude of a specific costate indicates the relevance of the corresponding state variable at the same moment in time. In particular, adjoint velocities play a key role, as they emphasize the importance of each thrust direction with respect to the others; the sign of each adjoint indicates whether its thrust component aligns (if positive) or opposes (if negative) the direction of that velocity.

Given the form assumed by the switching function in this analysis (see Section 4.5), the velocities and the position costates impact directly the correction procedure by influencing the slope and the level of the SF itself, respectively. Specific guesses must be selected based on the expected behavior of the SF, and then the optimal constants can be identified iteratively. In this case, the adjoint variables λ_ξ and λ_η are both set to 1×10^{-1}, while $\lambda_{\dot{\xi}}$ and $\lambda_{\dot{\eta}}$ can be imposed in the range $1 \times 10^{-2} \div 1 \times 10^{-3}$. The λ_ζ and $\lambda_{\dot{\zeta}}$ guesses are less relevant since the scenario is entirely planar. However, the high delicacy of the code prevents using null values, so small non-zero initial values are fixed equal to 1×10^{-7}. Finally, λ_m, indicator of the SC mass, is set around 1.

5.1.3 Terminal conditions

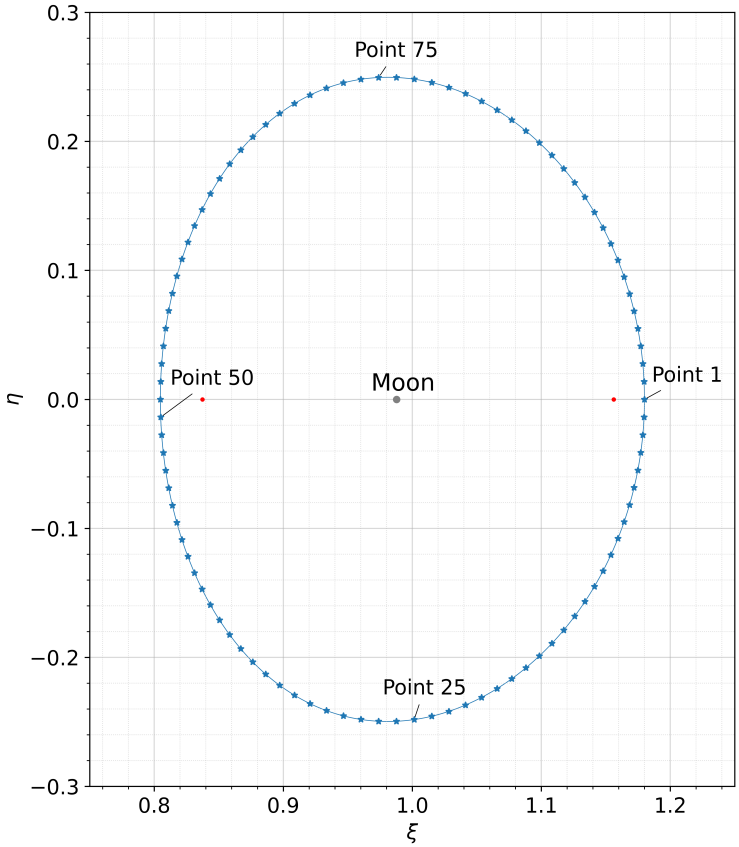

Fig. 5.2 Selected final points on DRO.

For fixed initial conditions, each transfer trajectory is uniquely distinguished by its final conditions. In this regard, the DRO is discretized into 100 different points, for which positions and velocities are known. Once the convergence for a specific final point is achieved, one can proceed to others using a continuation strategy to identify the optimal trajectory. Specifically, given the dynamics of the problem, the range of interest is from *point 97* to *point 24*.

Since the code proves to be extremely sensitive to changes in the Hamiltonian, the Fixed-Time Differential Correction (FTDC) procedure is employed. Starting from the period of the integrated trajectory, the integration time is manually increased to allow corrections until convergence. As a consequence, the application of the PMP ensures the solution optimality only for that specific time. Such limitation is mitigated as much as possible by exploring different times for each solution in hundredths of a day to avoid falling into a suboptimal solution.

The reduced set of terminal boundary conditions has the form:

$$\boldsymbol{\chi}_f = \left\{ \xi_f,\ \eta_f,\ \zeta_f,\ \dot{\xi}_f,\ \dot{\eta}_f,\ \dot{\zeta}_f,\ \lambda_{m_f},\ \Delta\tau_f \right\}^T, \tag{5.6}$$

where the notation $\Delta\tau$ is employed to distinguish the nondimensional integration time for transfer optimization (Δt for the dimensional one) from the integration time τ used during the orbits construction process. Please note that the time of flight will now be measured starting from the breakpoint. Therefore, 0.2954 days must be added to retrieve the effective total transfer time.

5.2 Fixed-time transfer trajectories

First off, a fixed-time sensitivity analysis is conducted for the first obtained convergence. In this case, convergence is reached with a transfer time of $\Delta t_f = 7.1$ days, targeting the same final point of the integrated trajectory (i.e. the point at $\eta = 0$), referred to here as *point 1*. Different values of Δt_f are investigated in the neighborhood of these 7.1 days to evaluate the impact of assigned time on the solution.

Figure 5.3 clearly shows how the structure of switching function and the fuel consumption change at varying of time of flight.

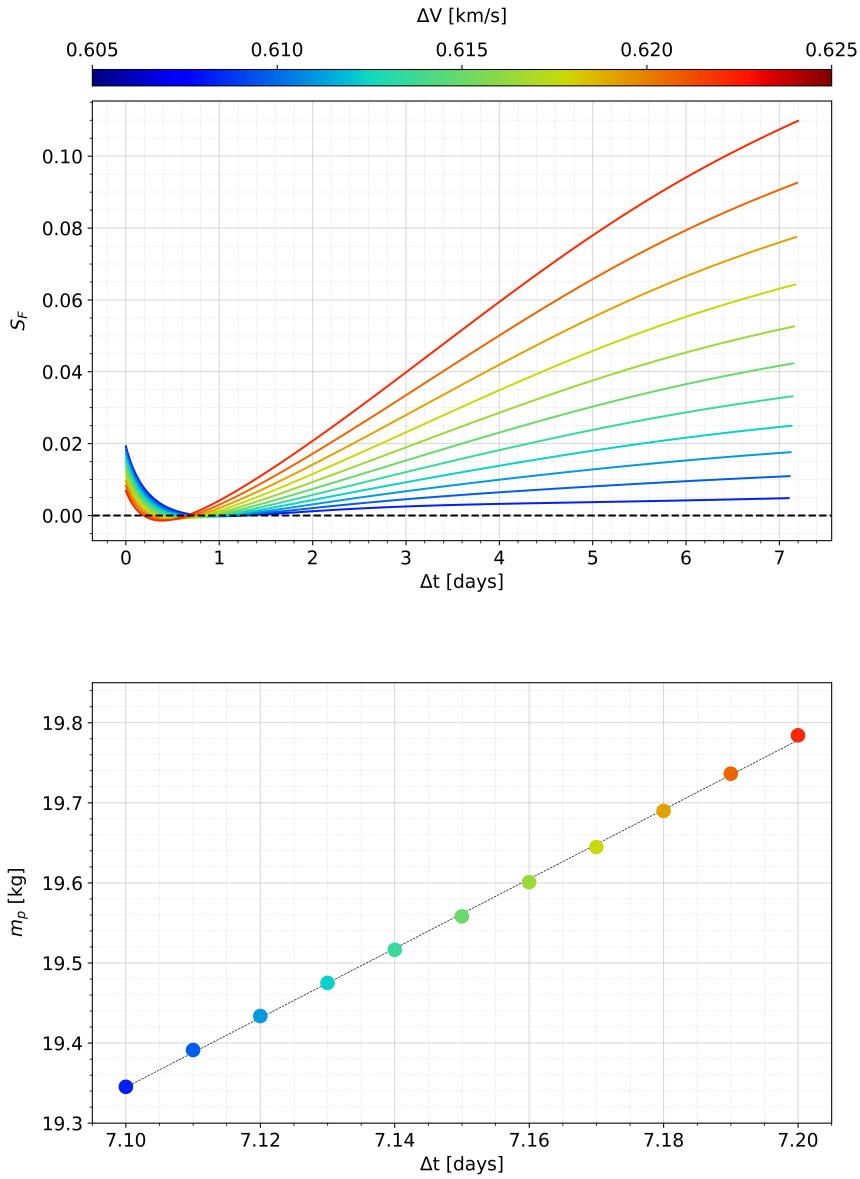

Fig. 5.3 SF structure and burned propellant mass for different Δt_f at *point 1*.

Under the same conditions, no convergence is achieved for lower times than 7.1 days, as the spacecraft has too little time and thrust to appropriately correct the trajectory and complete the transfer. All the SFs belong to the same family; they exhibit a two-burn structure, consisting of an initial thrust phase to orient the trajectory, a coasting phase, and a final thrust phase to achieve the orbit insertion (T-C-T scheme). Steeper slopes of SF involve longer coasting phases, which may

lead the satellite in a free-dynamic condition. To take back the trajectory on a controlled track, stronger corrections are required in the residual time, resulting in a more significant fuel consumption, with an almost linear trend.

For this reason, the evolution of in-plane angles α for these initial trajectories is reported in Figure 5.4. All the coasting phases occurs between 0.2 and 1.3 days.

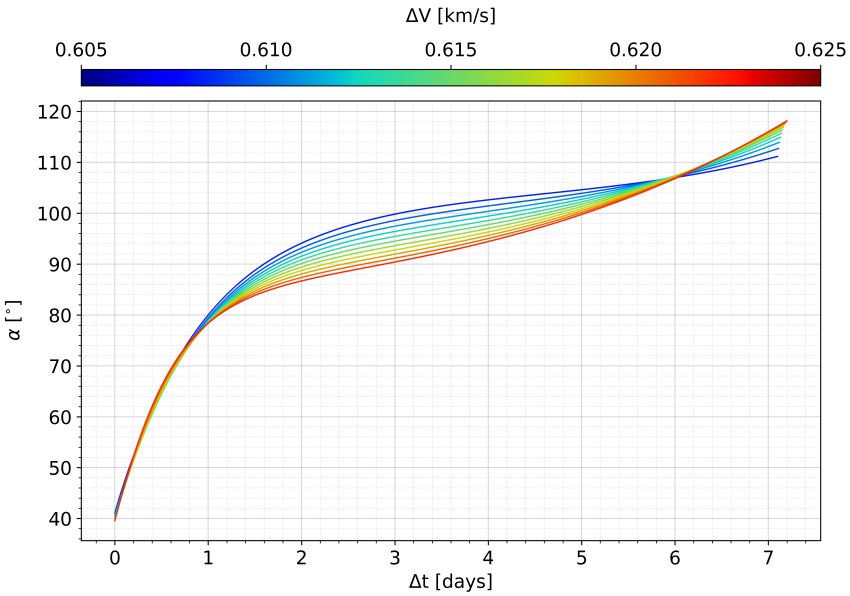

Fig. 5.4 Evolution of in-plane angles α over time for different Δt_f at *point 1*.

The solution at minimum propellant requests ends up coinciding with the one at minimum time, exactly at 7.1 days. For longer durations, the insertion trajectory slightly deviates from the optimal condition, causing the code to thrust in different directions, even if unnecessarily. After the coasting phase, the trajectory tends to open less outward and increase the satellite tangential velocity, before recovering in the final part. During this segment, indeed, the thrust opposes the SC's forward motion almost parallelly, slowing it down just enough for the DRI maneuver.

Moreover, it is worth remembering that in the CR3BP, due to existing perturbations, there are predefined paths for a given energy value, namely the Hill surfaces (see Section 2.2.5). Deviating from these trajectories may also require additional propellant.

The continuation strategy starts from here; similar reasonings are applied to the other points as well, searching for the solution at minimum time and consumption per each targeted point.

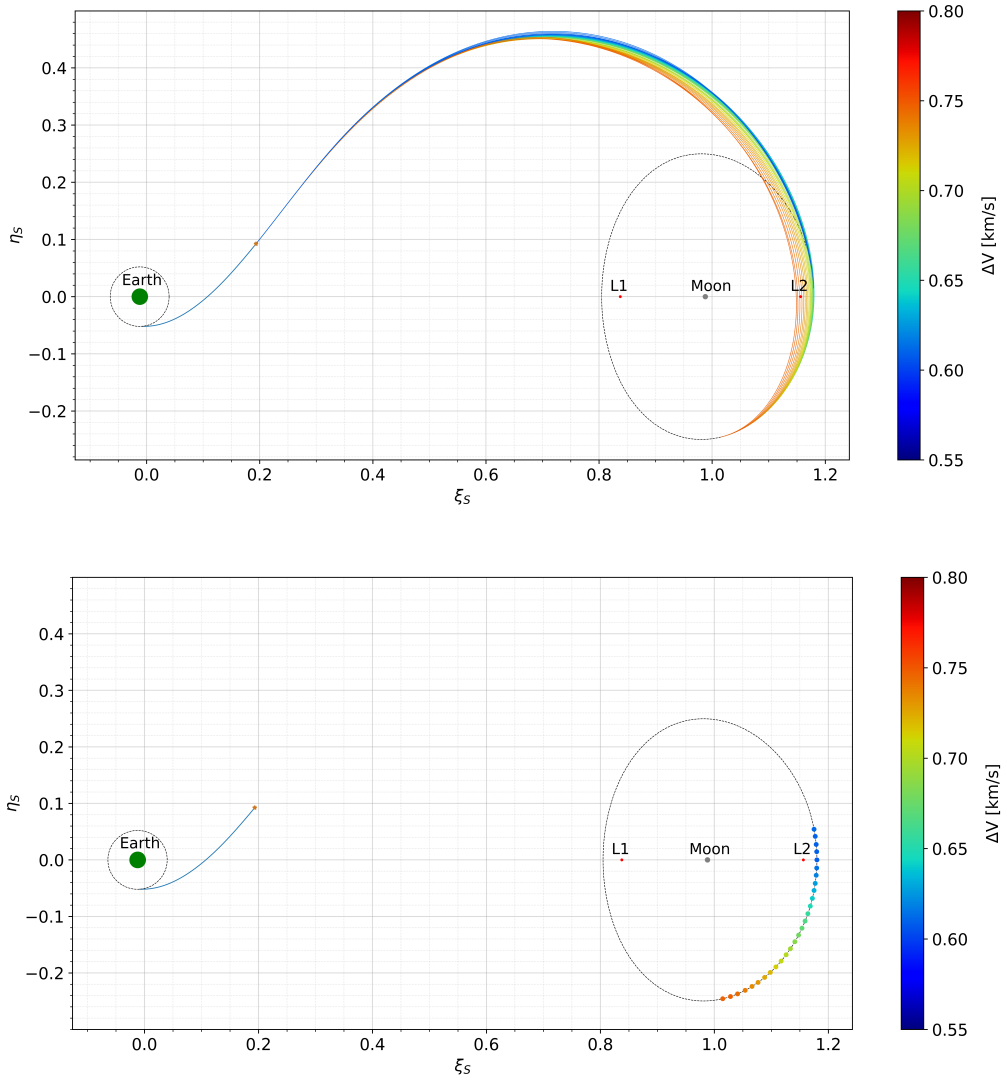

Fig. 5.5 Transfer trajectories for all targeted points on DRO in the $\hat{\boldsymbol{\xi}}_S - \hat{\boldsymbol{\eta}}_S$ plane.

By varying the final point on DRO and the relative fixed time, the entire family of solutions emerges. In Figure 5.5, all the resulting transfer trajectories are plotted in the $\hat{\boldsymbol{\xi}}_S - \hat{\boldsymbol{\eta}}_S$ plane as a function of the total ΔV utilized. A particular focus on the targeted points on orbit is also provided.

As previously mentioned, the concentration is on a limited area of interest on the final DRO. Concerning points at negative η, it is not practical to proceed beyond *point 24*, as the required ΔV only increases. The trends of $\mathcal{S}_{\mathcal{F}}$, besides, are increasingly flattening, indicating a gradual transition to another family, specifically to a five-phase structure (T-C-T-C-T). On the other side, solutions beyond *point 97* show a considerable increase in the slope of SF, while still maintaining a two-burn structure. Targeting these points implies transfers at the lowest times, increasing the difficulties in achieving convergence with the provided thrust values.

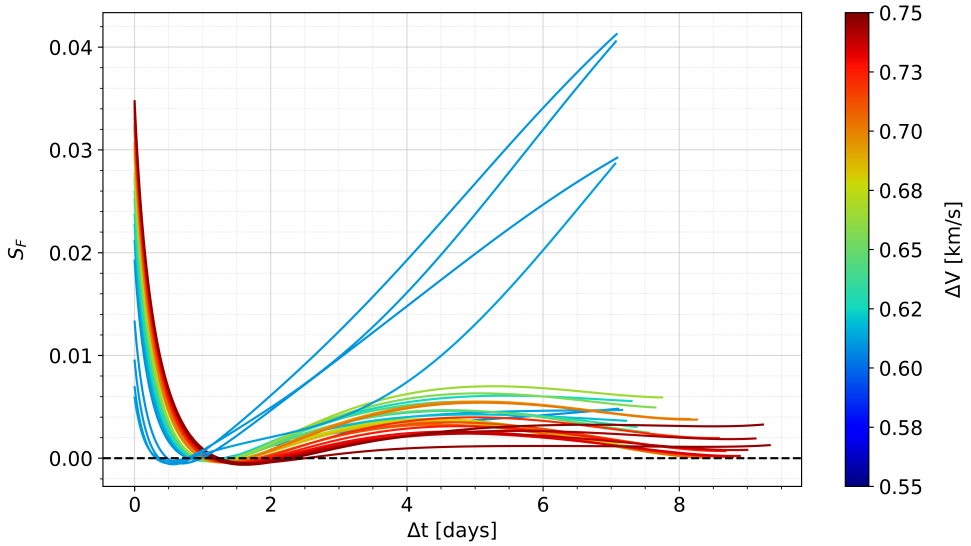

Fig. 5.6 SF structures for all trajectories. Lowest-time solutions stand out for their slopes.

The diverse behavior of $\eta > 0$ solutions is also reflected in the evolution of guesses over time (Figure 5.7). Particularly, while for λ_ξ, λ_η, and $\lambda_{\dot{\xi}}$ such curves follow the longer-time solutions, for $\lambda_{\dot{\eta}}$ they rise sharply, similar to what is observed for the SFs. This is because the guess $\lambda_{\dot{\eta}}$ is associated with the most significant variable of the problem -i.e. the $\dot{\eta}$ velocity-, which directly influences the primer vector in $\mathcal{S}_{\mathcal{F}}$. The trends of λ_ζ and $\lambda_{\dot{\zeta}}$, instead, stabilize at zero throughout the entire integration time. In order to respect the optimality conditions, $\lambda_{\dot{\zeta}}$ values gradually increase to 1.

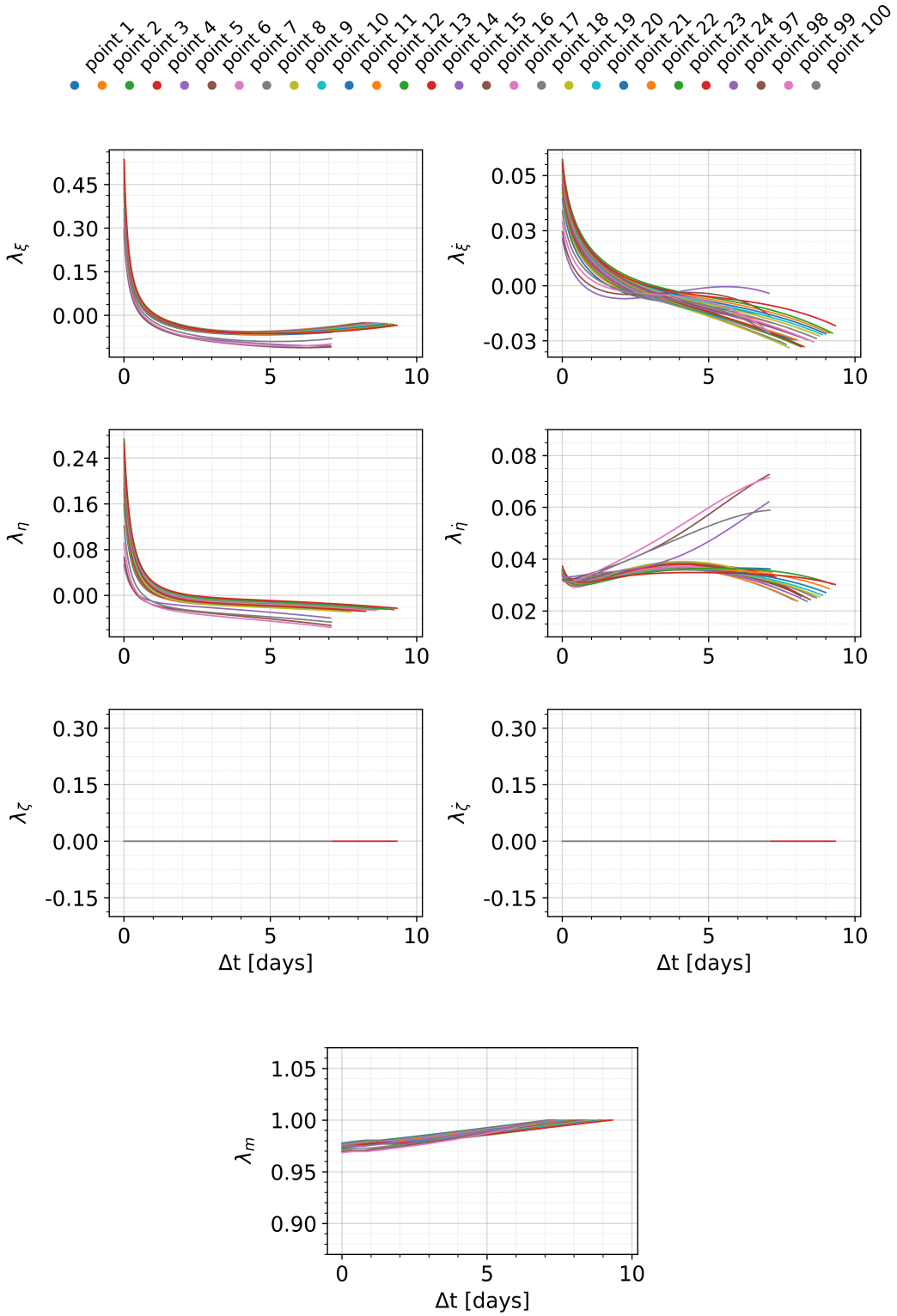

Fig. 5.7 Evolution of guesses $\{\lambda_{x_i}, \lambda_\eta, \lambda_\zeta, \lambda_{\dot{\xi}}, , \lambda_{\dot{\eta}}, \lambda_{\dot{\zeta}}, \lambda_m\}$ over time for all solutions.

The variation in the assigned time of flight is depicted in Figure 5.8 below. Each final point is expressed in percentage of position along the orbit, where *point 1* corresponds to 0%. The graph also reports the percentage of coasting time with respect to the relative transfer time (from breakpoint) for some solutions.

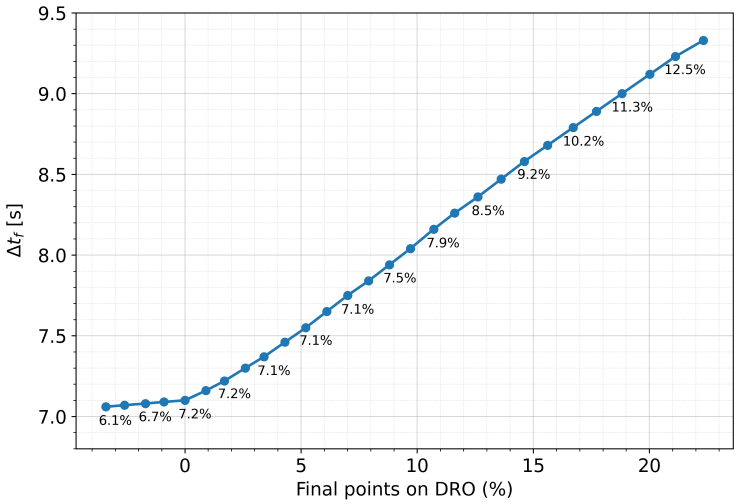

Fig. 5.8 Fixed time of flight Δt_f for each solution. The percentages of coasting time with respect to the transfer time are also reported.

It is easy to observe that, following the irregular shape of the DRO and targeting progressively more distant points, the assigned Δt values exhibits a perfectly linear trend, as one might expect. Once again, the resistance encountered in converging the solutions for $\eta > 0$ leads to a more cautious and gradual allocation of times, which explains the slightly lower slope of the initial segment.

Proceeding to $\eta < 0$ results in longer coasting time, but also the thrusting phases extend. Indeed, the propellant mass requests increases progressively (Figure 5.9), where, as usual, the relationship between m_p and ΔV is described by the Tsiolkovsky equation. Counterintuitively, a shorter transfer does not necessarily mean a lower consumption. For positive η values, while the transfer time decreases, the fuel consumption begins to increase again since the thrust phases must be sufficient to reach the orbit within the limited time available.

This increase is slightly mitigated by the easier achievement of the tangency condition between the trajectory and the orbit. Indeed, the optimal trajectory better suits the quasi-elliptical shape of the DRO by inserting the spacecraft with a velocity

that is as aligned as possible with the orbit velocities. Higher thrust values would be necessary to explore other solutions, both in terms of arc structure and insertion point on the DRO.

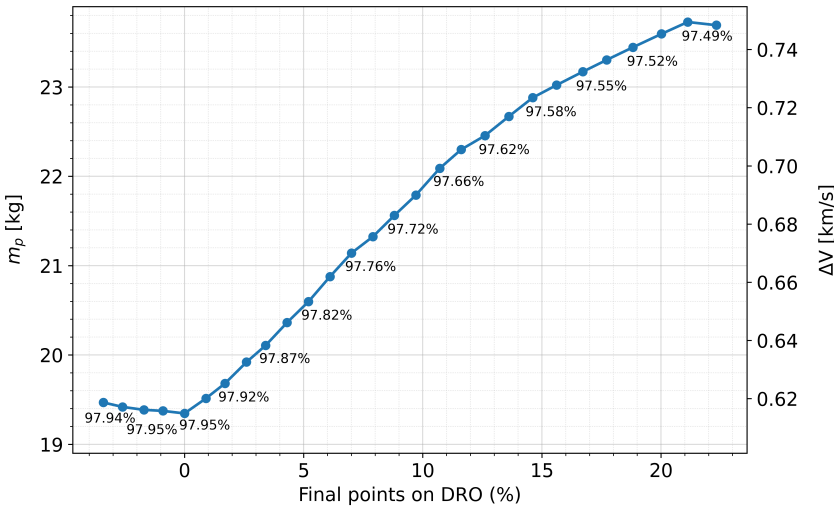

Fig. 5.9 Burned propellant mass (and total cost ΔV) for each solution. The percentages of SC final mass with respect to the initial mass are also reported.

As expected, the optimal trajectory proves to be the one at minimum time that least deviates from the integrated trajectory, specifically the one that targets *point 1*. This point ensures a perfectly tangential insertion at $\dot{\xi} = 0$, with a consumption of "only" 19.35 kg, equal to :

$$\boldsymbol{x}_f^* = \{1.180000, 0.000000, 0.000000, 0.000000, -0.498237, 0.000000, 925.3047\}^T,$$

where $m_f^* = 925.31$ kg is the optimal value of the SC final mass. The complete results are provided in Table 5.2.

The optimal transfer trajectory can be retrieved from the specific optimal guesses, $\boldsymbol{\lambda}_0^* = \{\lambda_\xi, \lambda_\eta, \lambda_\zeta, \lambda_{\dot{\xi}}, \lambda_{\dot{\eta}}, \lambda_{\dot{\zeta}}, \lambda_m\}^T$, reported here:

$$\boldsymbol{\lambda}_0^* = \{0.431809, 0.162831, 0.000000, 0.040203, 0.035012, 0.000000, 0.977617\}^T.$$

Table 5.2 Optimal final results

Δt^* [days]	m_f^* [kg]	m_p^* [kg]	ΔV^* [km/s]
7.10	925.31	19.35	0.6082

The plot in Figure 5.10 highlights the diverse phases along the trajectory, distinguished by color depending on whether the engine is turned on (in red) or off (in green). This low-thrust engine requires the satellite to thrust for the majority of the trajectory, except during the phase from $\xi \approx 0.40$ to 0.51, where it coasts.

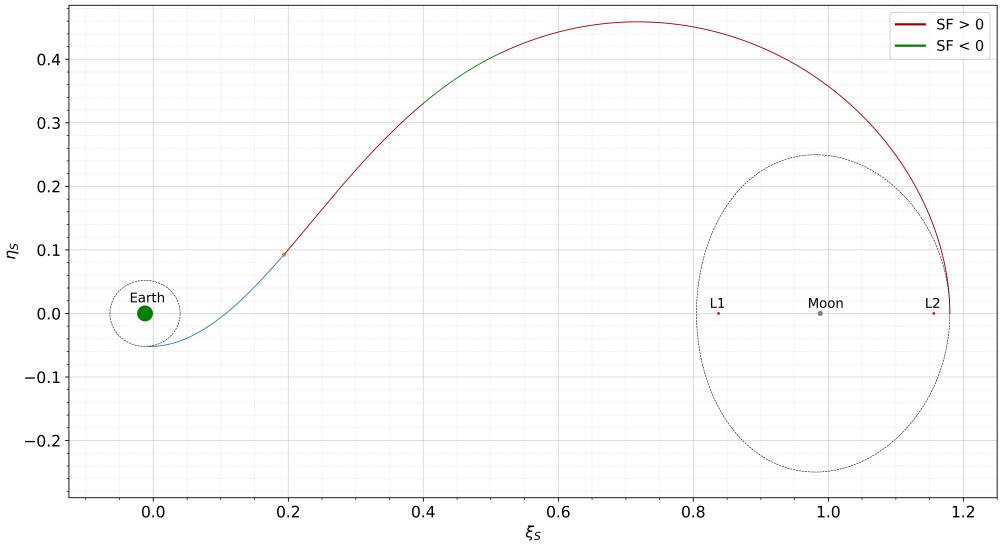

Fig. 5.10 Optimal transfer trajectory to *point 1*, divided into thrust phases ($\mathcal{S}_\mathcal{F} > 0$, in red) and coast phases ($\mathcal{S}_\mathcal{F} < 0$, in green).

As anticipated, the SF follows the T-C-T family scheme. Such structure, coupled with the final mass evolution over time, is displayed in Figure 5.11. The portion of the SF curve at negative values, corresponding to the coasting phase, results in a plateau at 942.32 kg in the total mass trend. It is precisely the duration of such coasting phase (equal to 7.2% of the assigned transfer time), that makes this solution stand out from the others, ensuring the best compromise between saving propellant and maintaining a controlled trajectory.

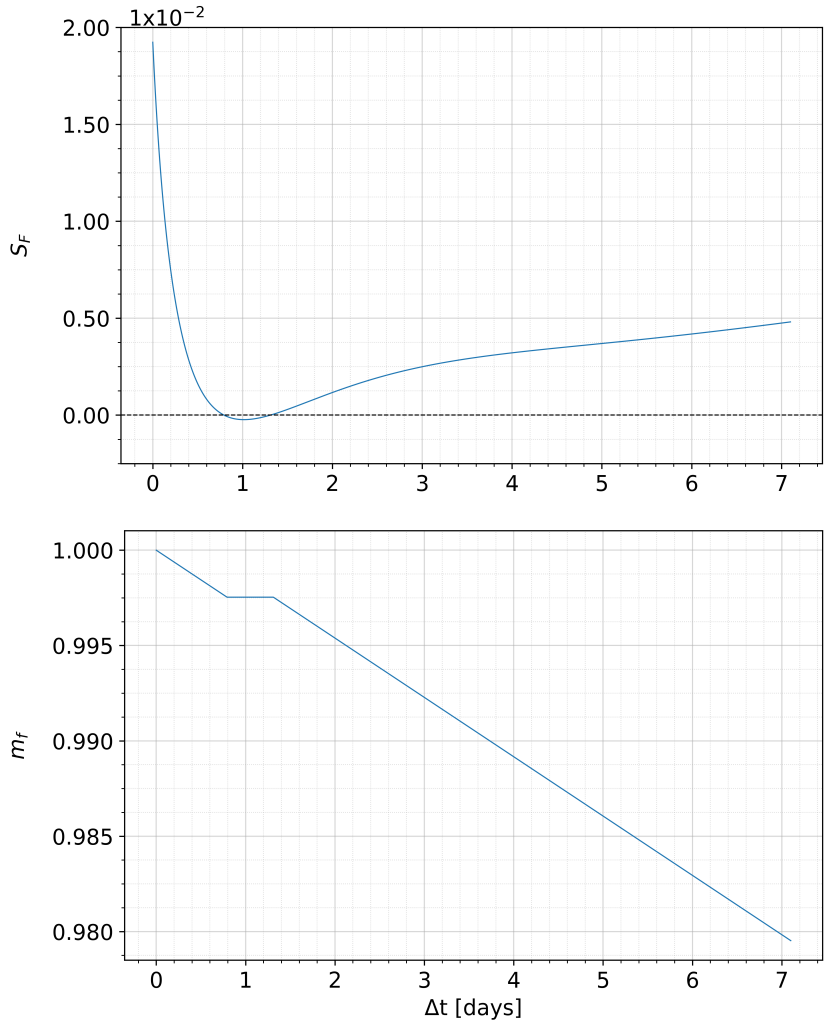

Fig. 5.11 Evolution of switching function and SC total mass fraction over time.

The direction of the thrust vector is not immediately apparent. For this reason, it is necessary to carefully analyze the evolution of the in-plane and out-of-plane thrust angles over time (Figure 5.12).

The α angle exhibits an always increasing trend. The initial values around $40 \div 50^\circ$ determine an acceleration in the forward direction. The satellite tends to open the trajectory upwards, arching it just enough to allow for DRO insertion. During the second thrust phase, the angle assumes values well beyond 90°, as the SC thrusts radially outwards and slows down.

The continuous deceleration peaks towards the end, when α reaches values around 111°, resulting in a thrust nearly opposite to the trajectory. This braking completely nullifies the velocity component along the $\hat{\boldsymbol{\xi}}_S$ axis, leading the spacecraft to the desired insertion velocities. The β angle, on the other hand, is always null, as the examined scenario is entirely planar.

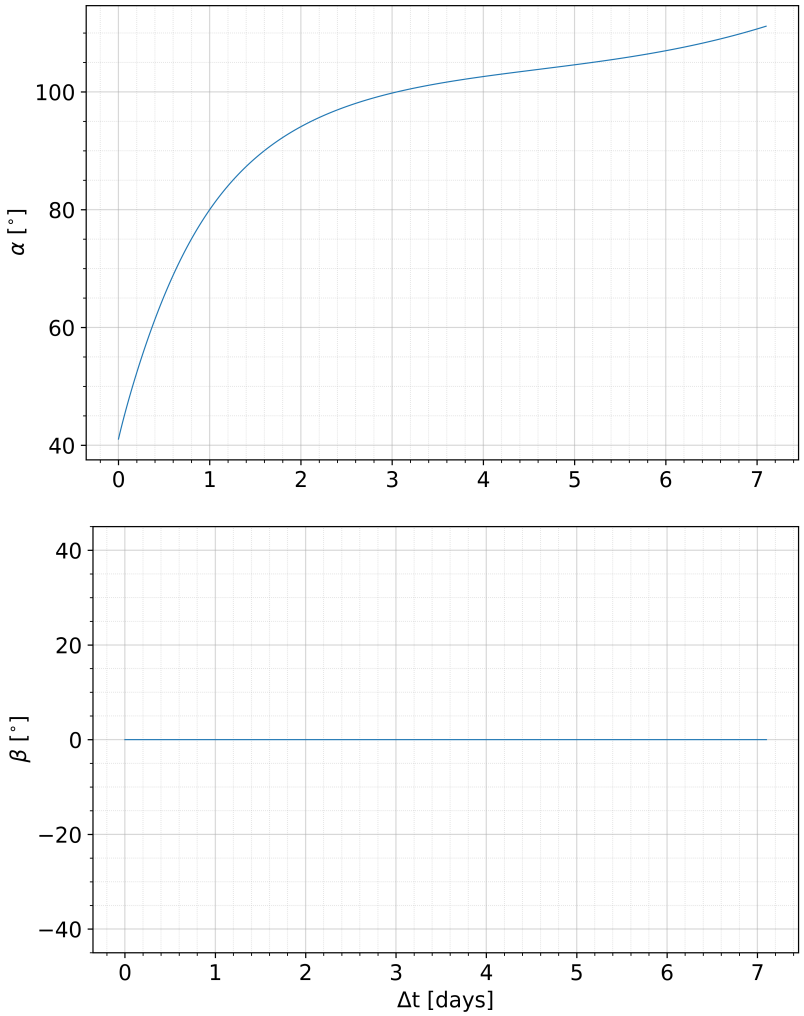

Fig. 5.12 Evolution of the in-plane α and out-of-plane β thrust angles over time.

For completeness, the time evolution of positions and velocities is also reported.

The trends of ξ and η perfectly reflect the arching of trajectory, while the velocities $\dot{\xi}$ and $\dot{\eta}$ decrease until they match those of *point 1*. Once again, the planar dynamics of the problem impose that ζ and $\dot{\zeta}$ are null.

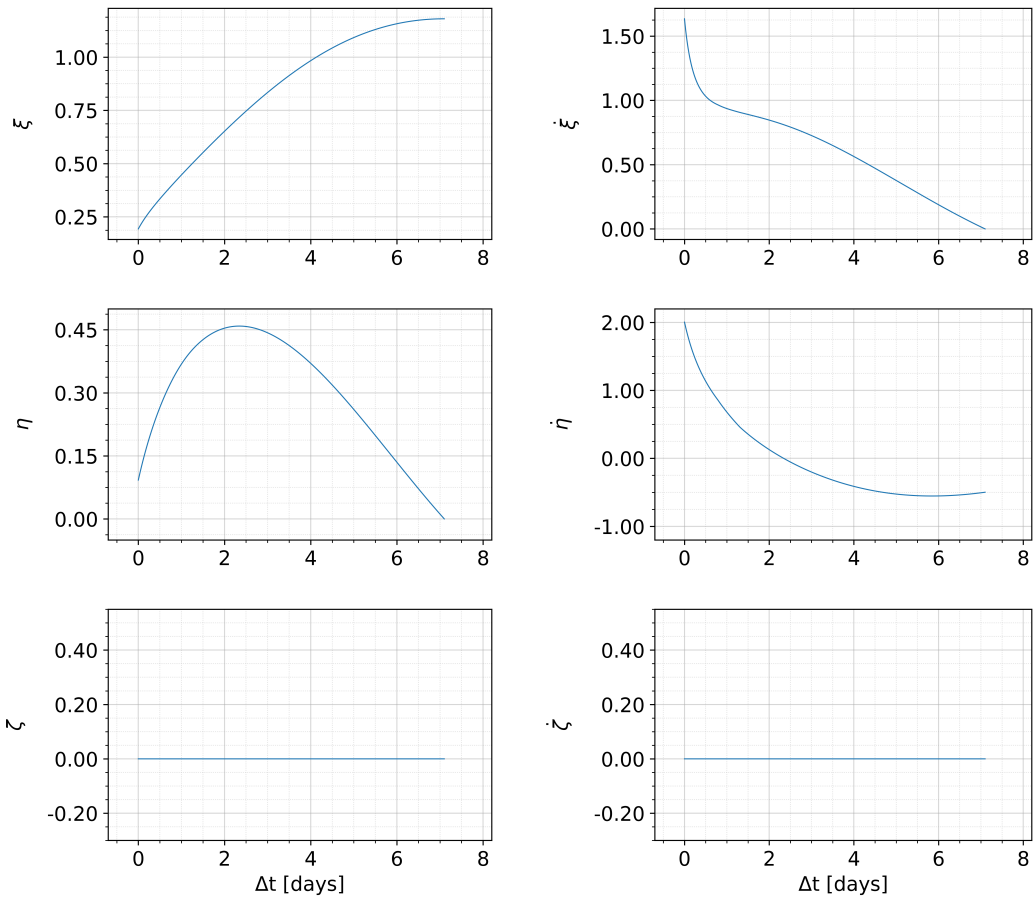

Fig. 5.13 Evolution of positions $\{\xi, \eta, \zeta\}$ and velocities $\{\dot{\xi}, \dot{\eta}, \dot{\zeta}\}$ over time.

Chapter 6

Conclusions

This thesis focuses on optimizing low-thrust lunar transfer trajectories within a medium-fidelity model, reflecting the current interest in establishing a scientific presence in cislunar space. Specifically, the scenario involves direct insertion trajectories into a selenocentric Distant Retrograde Orbit (DRO) within the planar Circular Restricted Three-Body Problem (CR3BP). Due to their high level of stability, these orbits are ideal solutions for long-term space missions, limiting the orbital maintenance corrections that are typically required.

In this context, space trajectory optimization represents the core of this work. Chapter 4 provides an extensive investigation of Optimal Control Theory (OCT), enabling a comparison between direct and indirect numerical methods. Although more challenging to implement, the indirect formulation has been identified as the most suitable for space application problems, ensuring more robust solutions and higher computational speed. The existance of transversality and optimality conditions at the extremal points of the domain leads to the formation of a classical Two-Point Boundary Value Problem (TPBVP).

For solving the case study BVP, all these principles have been applied to implement an iterative single-shooting algorithm with a fixed-time differential correction scheme. The objective was to maximize the final mass of the spacecraft, thus reducing propellant requirements and allowing for heavier mission payloads. However, the selection of a specific transfer time may result in a suboptimal solution. To address this issue, a time sensitivity analysis was conducted for each solution, inferring that the best trajectories were those with not only minimal fuel consumption but also

minimum time. The Pontryagin's Maximum Principle (PMP) allowed the validation of an optimal solution for that assigned time.

By leveraging the theoretical insights offered by the examined problem, a *bang-bang* control law was implemented, switching discontinuously between thrust and coast phases along the trajectory. Additionally, other tailored strategies have been employed to tackle the numerical intricacies of indirect method and facilitate the search for optimal guesses. Among these strategies, the trajectory was divided into two parts, with only the second one being subject to optimization, thereby redefining initial boundary conditions and simplifying the problem dynamics. The terminal conditions for the insertion, instead, were determined by positions and velocities on the DRO. Such a periodic orbit was initially computed within the CR3BP model, again using an iterative shooting method, then, it was discretized into several points, which served as targeted points for the optimization process.

To conclude, the dual purpose of this research has thus been achieved. The implemented code has proved to be flexible and efficient, establishing a valuable baseline for identifying cost-effective trajectories in the most diverse applications. Moreover, direct solutions to reach cislunar space, by exploiting the presence of stable, periodic DROs have been explored. Results suggest that two-burn trajectories provide the most effective approach for the orbit insertion. The optimal trajectory is the one at minimum fuel consumption, which best fits the quasi-elliptical shape of DRO in the shortest time.

6.1 Future research

Various possibilities for future developments would have been investigated in more detail with more available time. First, the limitations related to a fixed-time analysis need to be addressed. One promising direction is to effectively convert the TPBVP into a Multi-Point Boundary Value Problem (MPBVP), dividing the trajectory into multiple arcs and imposing additional boundary conditions at intermediate nodes. This strategy would perfectly fit the complex dynamics of the case study, allowing for effective handling of the code high sensitivity to variable-time corrections. At that point, the application of the PMP would ensure the incontrovertible optimality of the solution. Additionally, the challenges of the indirect method could be tackled

by defining *a priori* the succession of thrust and coast phases for the entire trajectory, thus stabilizing the switching structure and guiding the solution towards optimality.

Further improvements could focus on refining numerical techniques to enhance the algorithm efficiency and robustness. An automatic tool for generating guesses could also be implemented to reduce computational times, allowing for a rapid evaluation of different solutions. The high adaptability of the code leaves the door open for additional customizations.

The fundamentals of OCT can be extended to more complex space mission applications. For example, it may prove interesting to explore alternative solutions to DRO direct insertions, such as multi-revolution trajectories or transfers that exploit the contact points between DROs and tangential Lyapunov orbits [31]. Then, these maneuvers could be coupled with various scenarios of imminent interest, from rendezvous with asteroids to lunar landing operations [32–35].

For better adherence to reality, the model could be transitioned from the adopted CR3BP to a higher-fidelity n-Body Problem (NBP). Starting with a 4-body gravitational model (including the Sun, Earth, Moon, and spacecraft), ephemerides data and planetary perturbations must be taken into account. As mentioned in Chapter 3, the examined periodic orbits would be converted into Quasi-Periodic Orbits (QPOs) in the NBP, losing any stability or periodicity properties. Due to perturbing accelerations, such orbits diverge from their regular, closed CR3BP counterparts, generally exhibiting an unpredictable behavior. Future research may be directed towards investigating how perturbing effects impact on trajectory evolution. Moreover, variations in departure dates may significantly affect optimized trajectories, revealing diverse behaviors based on the relative positions of celestial bodies.

References

[1] NASA. The Artemis Plan, NASA's Lunar Exploration Program Overview. URL https://www.nasa.gov/wp-content/uploads/2020/12/artemis_plan-20200921.pdf?emrc=f43185. Technical Report NP-2020-05-2853-HQ. (Retrieved: 2023-11-20).

[2] ESA Earth Observation Portal (eoPortal). Lunar gateway of nasa's artemis program. URL https://www.eoportal.org/other-space-activities/lunar-gateway. (Retrieved: 2023-11-20).

[3] NASA. Gateway. URL https://www.nasa.gov/mission/gateway/. (Retrieved: 2023-11-20).

[4] Robert W. Farquhar and Ahmed A. Kamel. Quasi-periodic orbits about the translunar libration point. *Celestial mechanics*, 7(4):458–473, 1973.

[5] David L. Richardson. Analytic construction of periodic orbits about the collinear points. *Celestial mechanics*, 22(3):241–253, 1980.

[6] Ryan Whitley and Roland Martinez. Options for staging orbits in cislunar space. In *2016 IEEE Aerospace Conference*, pages 1–9. IEEE, 2016.

[7] Jeffrey S Parker and Rodney L Anderson. *Low-energy lunar trajectory design*, volume 12. John Wiley & Sons, 2014.

[8] Giorgio Mingotti, Francesco Topputo, and Franco Bernelli-Zazzera. Efficient invariant-manifold, low-thrust planar trajectories to the Moon. *Communications in Nonlinear Science and Numerical Simulation*, 17(2):817–831, 2012.

[9] Elisa Maria Alessi, Gerard Gomez, and Josep J. Masdemont. Two-manoeuvres transfers between LEOs and Lissajous orbits in the Earth-Moon system. *Advances in Space Research*, 45(10):1276–1291, 2010.

[10] Edward Belbruno and John Carrico. Calculation of weak stability boundary ballistic lunar transfer trajectories. In *Astrodynamics Specialist Conference*, page 4142, 2000.

[11] Edward Belbruno. Analytic estimation of weak stability boundaries and low energy transfers. *Celestial Mechanics, Dedicated to Donald Saari for his 60th Birthday*, 292:17, 2002.

[12] Li Mingtao and Zheng Jianhua. Impulsive lunar halo transfers using the stable manifolds and lunar flybys. *Acta Astronautica*, 66(9-10):1481–1492, 2010.

[13] Roger A Broucke. Periodic orbits in the restricted three body problem with earth-moon masses. Technical report, 1968.

[14] Michel Hénon. *Generating families in the restricted three-body problem*, volume 52. Springer Science & Business Media, 1997.

[15] Michel Hénon. Numerical exploration of the restricted problem, v. *Astronomy and Astrophysics, vol. 1, p. 223-238 (1969).*, 1:223–238, 1969.

[16] Michel Hénon. Numerical exploration of the restricted problem. VI. Hill's case: Non-periodic orbits. *Astronomy and Astrophysics, Vol. 9, p. 24-36*, 9:24–36, 1970.

[17] Michel Hénon. Vertical stability of periodic orbits in the restricted problem. I. Equal masses. *Astronomy and Astrophysics*, 28:415, 1973.

[18] Michel Hénon. Vertical Stability of Periodic Orbits in the Restricted Problem. II. Hill's Case. *Astronomy and Astrophysics*, 30:317–321, 1974.

[19] Collin J. Bezrouk and Jeffery Parker. Long duration stability of Distant Retrograde Orbits. In *AIAA/AAS astrodynamics specialist conference*, page 4424, 2014.

[20] Collin Bezrouk and Jeffrey S. Parker. Long-term evolution of Distant Retrograde Orbits in the Earth-Moon system. *Astrophysics and Space Science*, 362:1–11, 2017.

[21] M. Gates and D. Mazanek. Asteroid Redirect Mission (ARM), 2016.

[22] NASA. Orion Will Go the Distance in Retrograde Orbit During Artemis I. URL https://www.nasa.gov/missions/orion-will-go-the-distance-in-retrograde-orbit-during-artemis-i/. (Retrieved: 2023-11-20).

[23] Jeff Foust. Orion enters lunar Distant Retrograde Orbit. URL https://spacenews.com/orion-enters-lunar-distant-retrograde-orbit/. (Retrieved: 2023-11-20).

[24] Timothy F. Dawn, Jeffrey Gutkowski, Amelia Batcha, Jacob Williams, and Samuel Pedrotty. Trajectory design considerations for exploration mission 1. In *2018 Space Flight Mechanics Meeting*, page 0968, 2018.

[25] Amelia L. Batcha, Jacob Williams, Timothy F. Dawn, Jeffrey P. Gutkowski, Maxon V. Widner, Sarah L. Smallwood, Brian J. Killeen, Elizabeth C. Williams, and Robert E. Harpold. Artemis I trajectory design and optimization. In *2020 AAS/AIAA Astrodynamics Specialist Conference*, number AAS 20-649, 2020.

[26] Xu Ming and Xu Shijie. Exploration of distant retrograde orbits around Moon. *Acta Astronautica*, 65(5-6):853–860, 2009.

[27] Chelsea M. Welch, Jeffrey S. Parker, and Caley Buxton. Mission considerations for transfers to a distant retrograde orbit. *The Journal of the Astronautical Sciences*, 62:101–124, 2015.

[28] Cesar A. Ocampo and George W. Rosborough. Transfer trajectories for distant retrograde orbiters of the earth. *NASA STI/Recon Technical Report A*, 95:1323–1337, 1993.

[29] Jacob Demeyer and Pini Gurfil. Transfer to distant retrograde orbits using manifold theory. *Journal of Guidance, Control, and Dynamics*, 30(5):1261–1267, 2007.

[30] Giorgio Mingotti, Francesco Topputo, and Franco Bernelli-Zazzera. Transfers to distant periodic orbits around the Moon via their invariant manifolds. *Acta Astronautica*, 79:20–32, 2012.

[31] Lucia Capdevila, Davide Guzzetti, and Kathleen Howell. Various transfer options from Earth into distant retrograde orbits in the vicinity of the Moon. In *AAS/AIAA Space Flight Mechanics Meeting*, volume 118, 2014.

[32] Ruikang Zhang, Yue Wang, Hao Zhang, and Chen Zhang. Transfers from distant retrograde orbits to low lunar orbits. *Celestial Mechanics and Dynamical Astronomy*, 132:1–30, 2020.

[33] Naomi Murakami and Koji Yamanaka. Trajectory design for rendezvous in lunar Distant Retrograde Orbit. In *2015 IEEE Aerospace Conference*, pages 1–13. IEEE, 2015.

[34] Davide Conte, Marilena Di Carlo, Koki Ho, David B. Spencer, and Massimiliano Vasile. Earth-Mars transfers through Moon distant retrograde orbits. *Acta Astronautica*, 143:372–379, 2018.

[35] Davide Conte and David B. Spencer. Mission analysis for Earth to Mars-Phobos distant retrograde orbits. *Acta Astronautica*, 151:761–771, 2018.

[36] Leonhard Euler. *Elementa calculi variationum*. Euler Archive, 1770. URL https://scholarlycommons.pacific.edu/euler-works/385.Retrieved(2024-05-22).

[37] Leonhard Euler. Elementa calculi variationum. *Novi commentarii academiae scientiarum Petropolitanae*, pages 51–93, 1766.

[38] Joseph Louis Lagrange. *Mécanique analytique*, volume 1. Mallet-Bachelier, 1853.

[39] Arthur Earl Bryson and Yu-Chi Ho. *Applied optimal control: optimization, estimation, and control*. Blaisdell publishing company, 1969.

[40] David N. Burghes and Alexander Graham. *Control and optimal control theories with applications*. Horwood Publishing, 2004.

[41] Donald E. Kirk. *Optimal control theory: an introduction*. Courier Corporation, 2004.

[42] Emmanuel Trélat. Optimal control and applications to aerospace: some results and challenges. *Journal of Optimization Theory and Applications*, 154:713–758, 2012.

[43] John T. Betts. *Practical methods for optimal control and estimation using nonlinear programming*. SIAM, 2010.

[44] Luigi Mascolo. *Low-Thrust Optimal Escape Trajectories from Lagrangian Points and Quasi-Periodic Orbits in a High-Fidelity Model*. PhD thesis, Politecnico di Torino, Turin, 2023.

[45] David A. Vallado. *Fundamentals of astrodynamics and applications*, volume 12. Springer Science & Business Media, 2001.

[46] John E. Prussing and Bruce A. Conway. Orbital mechanics. *(No Title)*.

[47] Howard D. Curtis. *Orbital mechanics for engineering students: Revised Reprint*. Butterworth-Heinemann, 2020.

[48] Roger R. Bate, Donald D. Mueller, Jerry E. White, and William W. Saylor. *Fundamentals of astrodynamics*. Courier Dover Publications, 2020.

[49] Victor Szebehely. Theory of Orbits-The Restricted Problem of Three Bodies. *Academic Press Inc.*, 1967. ISBN 978-0-12412-431-8.

[50] Joseph-Louis Lagrange. Essai sur le probleme des trois corps. *Prix de l'académie royale des Sciences de paris*, 9:292, 1772.

[51] Dennis B. Westra. Lagrangian Points. URL https://www.mat.univie.ac.at/~westra, 2017.

[52] George William Hill. *The collected mathematical works of George William Hill*, volume 9. Carnegie institution of Washington, 1909.

[53] David L. Richardson. Periodic and Quasi Periodic Halo Orbits in the Earth-Sun/Earth-Moon Systems. Technical report, Technical report., 2010.

[54] Archie E. Roy. *Orbital motion*. CRC Press, 2020.

[55] NASA. Three-Body Periodic Orbits. URL https://ssd.jpl.nasa.gov/tools/periodic_orbits.html#/periodic. (Retrieved: 2024-05-16).

[56] David G. Luenberger, Yinyu Ye, et al. *Linear and nonlinear programming*, volume 2. Springer, 1984.

[57] Katta G. Murty and Feng-Tien Yu. *Linear complementarity, linear and nonlinear programming*, volume 3. Citeseer, 1988.

[58] John T. Betts. Survey of numerical methods for trajectory optimization. *Journal of guidance, control, and dynamics*, 21(2):193–207, 1998.

[59] Alessandro Zavoli. *Indirect Optimization of Bang-Bang Control Problems and Applications to Formation Flying Missions*. PhD thesis, Università La Sapienza di Roma, Rome, 2013.

[60] Robert E. Pritchett. *Numerical Methods for Low-Thrust Trajectory Optimization*. PhD thesis, Purdue University, West Lafayette, Indiana, 2016.

[61] Derek F. Lawden. Optimal trajectories for space navigation. *(No Title)*, 1963.

[62] Derek F. Lawden. Minimal rocket trajectories. *Journal of the American Rocket Society*, 23(6):360–367, 1953.

[63] Derek F. Lawden. Fundamentals of space navigation. *Journal of the British Interplanetary Society*, 13(2):87–101, 1954.

[64] Derek F. Lawden. Optimal Powered Arc in an Inverse Square Law Field, 1961.

[65] Francesco Topputo, Chen Zhang, et al. Survey of direct transcription for low-thrust space trajectory optimization with applications. In *Abstract and Applied Analysis*, volume 2014. Hindawi, 2014.

[66] Daniel Liberzon. *Calculus of variations and optimal control theory: a concise introduction*. Princeton university press, 2011.

[67] Guido Colasurdo and Lorenzo Casalino. Indirect methods for the optimization of spacecraft trajectories. *Modeling and Optimization in Space Engineering*, pages 141–158, 2013.

[68] Anil V. Rao. A survey of numerical methods for optimal control. *Advances in the astronautical Sciences*, 135(1):497–528, 2009.

[69] Bruce A. Conway. A survey of methods available for the numerical optimization of continuous dynamic systems. *Journal of Optimization Theory and Applications*, 152:271–306, 2012.

[70] Oskar Von Stryk and Roland Bulirsch. Direct and indirect methods for trajectory optimization. *Annals of operations research*, 37:357–373, 1992.

[71] David Morante, Manuel Sanjurjo Rivo, and Manuel Soler. A survey on low-thrust trajectory optimization approaches. *Aerospace*, 8(3):88, 2021.

[72] Abolfazl Shirazi, Josu Ceberio, and Jose A. Lozano. Spacecraft trajectory optimization: A review of models, objectives, approaches and solutions. *Progress in Aerospace Sciences*, 102:76–98, 2018.

[73] Pierre-Louis Lions. On the Hamilton-Jacobi-Bellman equations. *Acta Applicandae Mathematica*, 1:17–41, 1983.

[74] James Phillip McDanell and William Francis Powers. Necessary conditions joining optimal singular and nonsingular subarcs. *SIAM Journal on Control*, 9(2):161–173, 1971.

[75] L.F. Shampine and M.K. Gordon. Computer solution of ordinary differential equations: the initial value problem, 1975.

[76] Forest Ray Moulton. *New methods in exterior ballistics*. University of Chicago Press, 1926.

[77] SciPy Community. scipy.integrate.LSODA. URL https://docs.scipy.org/doc/scipy/reference/generated/scipy.integrate.LSODA.html, 2024. (Retrieved: 2023-11-20).

[78] Chen Zhang, Francesco Topputo, Franco Bernelli-Zazzera, and Yu-Shan Zhao. Low-thrust minimum-fuel optimization in the circular restricted three-body problem. *Journal of Guidance, Control, and Dynamics*, 38(8):1501–1510, 2015.

[79] Cristiana Silva and Emmanuel Trélat. Smooth regularization of bang-bang optimal control problems. *IEEE Transactions on Automatic Control*, 55(11):2488–2499, 2010.

[80] Thomas Antony and Michael J. Grant. Path constraint regularization in optimal control problems using saturation functions. In *2018 AIAA Atmospheric Flight Mechanics Conference*, page 18, 2018.

Appendix A

CR3BP Partial pseudopotential $\mathscr{U}$ derivatives

First derivatives

$$\begin{aligned}\frac{\partial \mathscr{U}}{\partial \xi} &= \frac{\partial}{\partial \xi}\left\{\frac{1}{2}(\xi^2+\eta^2)+\frac{1-\mu}{\left[(\xi+\mu)^2+\eta^2+\zeta^2\right]^{\frac{1}{2}}}+\frac{\mu}{\left[(\xi-1+\mu)^2+\eta^2+\zeta^2\right]^{\frac{1}{2}}}\right\}\\ &= \xi-\frac{(1-\mu)(\xi+\mu)}{\left[(\xi+\mu)^2+\eta^2+\zeta^2\right]^{\frac{3}{2}}}-\frac{\mu(\xi-1+\mu)}{\left[(\xi-1+\mu)^2+\eta^2+\zeta^2\right]^{\frac{3}{2}}}\\ &= \xi-(1-\mu)\frac{(\xi+\mu)}{\rho_{13}^3}-\mu\frac{(\xi-1+\mu)}{\rho_{23}^3}\end{aligned} \tag{A.1a}$$

$$\frac{\partial \mathscr{U}}{\partial \eta} = \eta-(1-\mu)\frac{\eta}{\rho_{13}^3}-\mu\frac{\eta}{\rho_{23}^3} \tag{A.1b}$$

$$\frac{\partial \mathscr{U}}{\partial \zeta} = -(1-\mu)\frac{\zeta}{\rho_{13}^3}-\mu\frac{\zeta}{\rho_{23}^3} \tag{A.1c}$$

Second derivatives

$$\mathscr{U}_{\xi\xi} = 1 - \frac{(1-\mu)}{\rho_{13}^5}\left[\rho_{13}^2 - 3(\xi+\mu)^2\right] - \frac{\mu}{\rho_{23}^5}\left[\rho_{23}^2 - 3(\xi-1+\mu)^2\right] \tag{A.2a}$$

$$\mathscr{U}_{\xi\eta} = 3\eta\left[\frac{(1-\mu)}{\rho_{13}^5}(\xi+\mu) + \frac{\mu}{\rho_{23}^5}(\xi-1+\mu)\right] \tag{A.2b}$$

$$\mathscr{U}_{\xi\zeta} = 3\zeta\left[\frac{(1-\mu)}{\rho_{13}^5}(\xi+\mu) + \frac{\mu}{\rho_{23}^5}(\xi-1+\mu)\right] \tag{A.2c}$$

$$\mathscr{U}_{\eta\xi} = \mathscr{U}_{\xi\eta} \tag{A.2d}$$

$$\mathscr{U}_{\eta\eta} = 1 - \frac{(1-\mu)}{\rho_{13}^5}\left(\rho_{13}^2 - 3\eta^2\right) - \frac{\mu}{\rho_{23}^5}\left(\rho_{23}^2 - 3\eta^2\right) \tag{A.2e}$$

$$\mathscr{U}_{\eta\zeta} = 3\eta\zeta\left[\frac{(1-\mu)}{\rho_{13}^5} + \frac{\mu}{\rho_{23}^5}\right] \tag{A.2f}$$

$$\mathscr{U}_{\zeta\xi} = \mathscr{U}_{\xi\zeta} \tag{A.2g}$$

$$\mathscr{U}_{\zeta\eta} = \mathscr{U}_{\eta\zeta} \tag{A.2h}$$

$$\mathscr{U}_{\zeta\zeta} = -\frac{(1-\mu)}{\rho_{13}^5}\left(\rho_{13}^2 - 3\zeta^2\right) - \frac{\mu}{\rho_{23}^5}\left(\rho_{23}^2 - 3\zeta^2\right) \tag{A.2i}$$

Appendix B

Euler-Lagrange equations for the adjoint variables

$$\dot{\boldsymbol{\lambda}} = -\frac{\partial \mathcal{H}}{\partial \boldsymbol{x}} \tag{B.1}$$

$$\begin{aligned}
\dot{\lambda}_\xi = &-\lambda_{\dot{\xi}} \left[1 - \frac{1-\mu}{\rho_{13}^3} + \frac{3(1-\mu)(\xi+\mu)^2}{\rho_{13}^5} - \frac{\mu}{\rho_{23}^3} + \frac{3\mu(\xi-(1-\mu))^2}{\rho_{23}^5} \right] + \\
&- \lambda_{\dot{\eta}} \left[\frac{3(1-\mu)(\xi+\mu)\eta}{\rho_{13}^5} + \frac{3\mu(\xi-(1-\mu))\eta}{\rho_{23}^5} \right] + \\
&- \lambda_{\dot{\zeta}} \left[\frac{3(1-\mu)(\xi+\mu)\zeta}{\rho_{13}^5} + \frac{3\mu(\xi-(1-\mu))\zeta}{\rho_{23}^5} \right]
\end{aligned} \tag{B.2a}$$

$$\begin{aligned}
\dot{\lambda}_\eta = &-\lambda_{\dot{\xi}} \left[\frac{3(1-\mu)(\xi+\mu)\eta}{\rho_{13}^5} + \frac{3\mu(\xi-(1-\mu))\eta}{\rho_{23}^5} \right] + \\
&- \lambda_{\dot{\eta}} \left[1 - \frac{1-\mu}{\rho_{13}^3} + \frac{3(1-\mu)\eta^2}{\rho_{13}^5} - \frac{\mu}{\rho_{23}^3} + \frac{3\mu\eta^2}{\rho_{23}^5} \right] + \\
&- \lambda_{\dot{\zeta}} \left[\frac{3(1-\mu)\eta\zeta}{\rho_{13}^5} + \frac{3\mu\eta\zeta}{\rho_{23}^5} \right]
\end{aligned} \tag{B.2b}$$

$$\begin{aligned}\dot{\lambda}_\zeta = &-\lambda_{\dot{\xi}}\left[\frac{3(1-\mu)(\xi+\mu)\zeta}{\rho_{13}^5}+\frac{3\mu(\xi-(1-\mu))\zeta}{\rho_{23}^5}\right]+\\ &-\lambda_{\dot{\eta}}\left[\frac{3(1-\mu)\eta\zeta}{\rho_{13}^5}+\frac{3\mu\eta\zeta}{\rho_{23}^5}\right]+\\ &-\lambda_{\dot{\zeta}}\left[-\frac{1-\mu}{\rho_{13}^3}+\frac{3(1-\mu)\zeta^2}{\rho_{13}^5}-\frac{\mu}{\rho_{23}^3}+\frac{3\mu\zeta^2}{\rho_{23}^5}\right]\end{aligned} \tag{B.2c}$$

$$\dot{\lambda}_{\dot{\xi}} = -\lambda_\xi - 2\lambda_{\dot{\eta}} \tag{B.2d}$$

$$\dot{\lambda}_{\dot{\eta}} = -\lambda_\eta + 2\lambda_{\dot{\xi}} \tag{B.2e}$$

$$\dot{\lambda}_{\dot{\zeta}} = -\lambda_\zeta \tag{B.2f}$$

$$\dot{\lambda}_m = \frac{T}{m^2}\lambda_\mathcal{V} \tag{B.2g}$$